MODEL-BASED ENHANCEMENT OF MAMMOGRAPHIC IMAGES

by

R. P. Highnam

Technical Monograph PRG-105
ISBN 0-902928-82-1

Trinity 1992

Oxford University Computing Laboratory
Programming Research Group
11 Keble Road
Oxford OX1 3QD
England

Oxford University Computing Laboratory
Programming Research Group
11 Keble Road
Oxford OX1 3QD
England

Model-Based Enhancement of Mammographic Images

by

Ralph Philip Highnam

Thesis submitted for the degree of
Doctor of Philosophy
at the
University of Oxford

Programming Research Group
Oxford University Computing Laboratory

Lady Margaret Hall
Trinity Term 1992

Model-Based Enhancement of Mammographic Images

by

Ralph Philip Highnam

Thesis submitted for the Degree of Doctor of Philosophy

at the University of Oxford

Programming Research Group
Oxford University Computing Laboratory

Lady Margaret Hall
Trinity Term 1992

Abstract

We investigate model-based image enhancement of mammographic images and demonstrate the dangers of ad-hoc image enhancement and analysis. A model of the mammographic process, including degrading factors and the breast is developed. The breast is considered to consist mainly of "interesting tissue" (glandular/fibrous/cancerous) and fat. Knowledge of both the compressed breast thickness and exposure are necessary for the mammography-specific algorithms developed. It is the degrading factors which are the basis for model-based image enhancement. We study four degrading factors: scattered radiation, beam hardening, the spatially varying incident radiation intensity, and poor positioning of the automatic exposure control. The spatially varying incident radiation intensity can be measured and the mammographic images compensated by performing an x-ray exposure with no object present, this also provides some of the calibration data. Poor positioning of the automatic exposure control can be overcome by modeling the action of the control unit; this proves to be useful in amplifying scatter-removed signals to create decent images. Scatter is the key degrading factor since removing it allows simulation of a monoenergetic x-ray beam, and thus removal of the effects of beam hardening. We model scatter with a conjectured relationship between energy imparted due to scatter at a central pixel with energy imparted in a surrounding neighbourhood. Simulating a monoenergetic x-ray beam requires a choice of a photon energy, and this choice can be made with consideration only of image quality, since radiation dose to the breast is irrelevant in a theoretical situation. Scatter removal is local high-pass filtering, and the monoenergetic simulation introduces contrast according to the chosen photon energy. Both algorithms greatly enhance mammographic images, including microcalcifications. The overall model can be verified quantitatively by inspection of the thicknesses of interesting tissue which must have been present to give the measured attenuation. The results of these tests were exceptionally good.

Also considered in this thesis are the effects of breast compression on the mammogram. A new technique is proposed ("differential compression mammography") which aims to aid diagnosis by using the changes that are observed between two mammograms performed at different compressions. The initial results of a clinical trial are presented, and these are encouraging.

We show that if image analysis algorithms are to work robustly, account of the imaging parameters and degree of breast compression must be taken.

Acknowledgements

Without doubt, the most enjoyable part of this thesis was the interaction with many different people from many different backgrounds. Starting at the Churchill Hospital, which is where the breast screening unit is based, the breast care team have been overwhelmingly helpful, especially Yvonne, Wendy and Chris (the radiographers): our work on mammograms performed at different breast compressions could not have taken place without their skill and tact. Dr. Basil Shepstone, the radiologist with whom we have collaborated, has shown enormous patience in revealing some of the secrets of his trade, and in answering my weekly series of questions at often busy assessment clinics.

At the John Radcliffe Hospital, Donald Peach, teacher of radiography, has spent many hours discussing with me the physics and techniques of radiography, and has at all times been enthusiastic and encouraging. Also at the John Radcliffe, I would like to thank the pathologists and surgeons who have allowed me to be with them whilst they worked. This gave me a much better understanding of the breast, breast cancer, and breast compression. Discussions with Dr. George Cherry and Dr. Terrance Ryan in the Dermatology Department at the Slade Hospital, also helped in my understanding of breast compression.

Although officially within the Computing Laboratory, most of this work has been carried out in the Robotics Group. Of the numerous people in these two groups who have saved me from the computer, Phil Winder stands out. Alternating the mammograms performed at different compressions to see the motion was suggested by Guy Scott. Much of the early parts of this thesis were discussed with Christopher Longuet-Higgins, and by these discussions many of the ideas became ordered and formed a solid base upon which to build. Rachel Harris helped greatly with the English.

I would like to express my gratitude to David Dance and Huw Davies at the Royal Marsden Hospital. Not only did they allow me to use their Joyce-Loeble scanning microdensitometer, but David Dance also provided some of the data necessary to complete my work and spent time discussing it with me.

Finally, many thanks to Mike Brady for keeping me on the right tracks with his adept supervision, and phenomenal vision and instinct.

I acknowledge the financial support of the Science and Engineering Research Council.

Contents

List of Figures

List of Tables

1

Introduction

1.1 Detection of breast cancer

About 1 in 12 women develop breast cancer during the course of their lives. There are accepted risk factors for development of breast cancer, such as family history of the disease and early menarche, but prevention is impossible at present. In such circumstances, detection becomes the primary means of reducing mortality, and it is acknowledged that the earlier that breast cancer is diagnosed, the better the prognosis.

There are several techniques available to the radiologist to aid the detection and diagnosis of breast cancer: mammography, ultrasound, palpation, magnification mammography, fine needle aspiration biopsy, and open surgical biopsy. Of the non-invasive techniques, only mammography has been proven to detect the earliest signs of cancer. Consequently, mammography is the technique used in breast cancer screening programmes [31].

The screening programme in Britain involves examining an estimated one and a half million women each year. One mammogram of each breast is performed at screening, and so highly trained radiologists have to examine some three million mammograms a year. This is immensely time consuming and expensive in both man-power and equipment.

Diagnosis of breast cancer from a mammogram is difficult for several reasons: many signs are ambiguous; subtle differences in x-ray attenuation can be crucial; composites occur; important signs are hidden by the projected nature of the image and dense tissue;

the images can sometimes be of a poor quality. Appendix C contains a description of the radiologist's task.

10% of all the women who attend for screening have to endure the psychological trauma of being recalled to an assessment clinic due to abnormalities in their initial mammograms. Many of these abnormalities are resolved by performing further mammograms at different viewing angles. Ultrasound, palpation and fine needle aspiration biopsy are used if the radiologist is still suspicious. Despite all of these tests, some 8% of cancers are missed [67] and 70-80% of open surgical biopsies are benign [91].

The type of signs commonly looked for in mammography, the importance of detection of these signs, and the sheer cost involved in screening suggest that image processing and image analysis could contribute to more effective screening.

1.2 Role of computer

The computer might play a number of different roles which complement the radiologist:

- Image archiving: the screening programme produces huge numbers of mammographic films that degrade over time and require storage space.
- Image enhancement: mammographic images are substantially degraded, and contain information not immediately visible on a light box. Digital enhancement of an image is important practically because the image is improved with no further radiation dose to the breast.
- Objective measures: radiologists are subjective observers of mammographic signs, and they often try to correlate these signs with malignancy. Objective measures calculated by a computer should remove intra-observer and inter-observer differences and provide more consistent results.
- Sorting easy/difficult: the computer could sort the mammographic images into easy-to-diagnose and difficult-to-diagnose so that a more experienced radiologist gets the difficult images, whilst a less experienced radiologist (or computer maybe) gets the easy images.

Furthermore, the computer might play a role which emulates a radiologist:

- Prompting: the radiologist is prompted to look at certain sections of the mammographic image which have been deemed suspicious by a computer program.
- Second opinion: every mammogram should be viewed by two radiologists; the computer might take the place of one of them.

- Fully automated diagnosis: the ultimate goal, which has been aimed at since the earliest days of accessible computing. In 1967, Winsberg et al. [107] wrote: "Because of the problems inherent in the routine viewing of large numbers of examinations of presumably asymptomatic patients we have proposed the automation of reading of the radiographs...".

These roles are more important in a screening programme than in the context of a clinic for symptomatic women, since it is well known that humans performing routine inspections of mostly normal images perform poorly after a short period of time.

The roles in the list which seek to complement a radiologist will be possible for the computer to perform within the forseeable future. The roles which seek to emulate a radiologist will not be possible for the computer to perform until there is real understanding of what the radiologist is doing.

1.3 The case for model-based image enhancement

1.3.1 The need for care

The application of computer technology to mammography is safety-critical: the computer algorithms must work perfectly; there is no room for error. This is especially true with image enhancement where the computer is deemed to be "merely" enhancing the image, and not offering an opinion; in this situation the radiologist must assume the computer is reliable.

Any diagnostic error resulting from a radiologist's use of a computer, however minor, may have serious consequences for the woman involved. This could be psychological stress from having to be recalled unnecessarily, through to physical harm from open surgical biopsy or, most seriously, missing a carcinoma. To put diagnostic error in perspective: a wrong decision in just 1 case in every 10000 affects 300 women per year in the UK. In cases where the radiologist has misdiagnosed using a computer, there will clearly be legal implications for both the radiologist and perhaps the computer programmer.

The present legal situation is one of the reasons for the high number of open surgical biopsies finding benign disease: charges are only brought against a radiologist who has been negligent through missing a cancer, and not against a radiologist who has sent a woman for a biopsy which reveals benign disease. This situation will lead to the design of computer algorithms so as to ensure no false negatives, with the possible risk of high false positives.

This thesis seeks to show that image enhancement is most reliably and robustly achieved by using a model of the imaging process and degrading factors, rather than through the use of unpredictable, ad-hoc methods.

1.3.2 Non-robustness of ad-hoc enhancement

Robustness of an enhancement algorithm describes the breadth of images to which the algorithm can usefully be applied. Even the most general enhancement algorithms have a range of images to which they can be applied usefully, and a range of images to which application of the algorithm is pointless. Enhancement algorithms need to be robust because to a radiologist the computer appears as a black box with buttons which have generic names (eg. "edge sharpen"). Consequently, the radiologist is unlikely to understand initially what the computer is doing and can only learn from lengthy experience.

Consider conventional image enhancement techniques. Some of these are clearly not applicable to mammographic images. Histogram equalisation is a particularly good example, because not only do the histograms of mammographic images peak in the pixel values which are not of interest to the radiologist, but the process takes substantial time; time which the radiologist spends waiting for the results only to be disappointed. Figure (1.1) shows an original image and figure (1.2) shows a histogram-equalized version of the original after segmentation of the breast area from the film.

Stretching the histogram of an image to fill the entire dynamic range works by finding the minimum and maximum pixel values in the image and stretching them out to the minimum and maximum displayable. This kind of routine has disadvantages in practice since mammographic images contain information reaching over the entire range, and much of this information is useless for diagnoses. Better results can be obtained if the breast area is segmented accurately from the irrelevant information, but the stretching technique is still susceptible to noise.

1.3.3 Unreliability of ad-hoc image enhancement

Reliability is crucial in the image processing of mammograms, and yet many marketed medical image processing systems use unpredictable generic functions such as "edge enhancement". Some edge enhancement is certainly reliable as there is smoothing in most imaging systems, but over-enhancement of edges in mammographic images is not:

Figure 1.1: Original mammographic image GML1

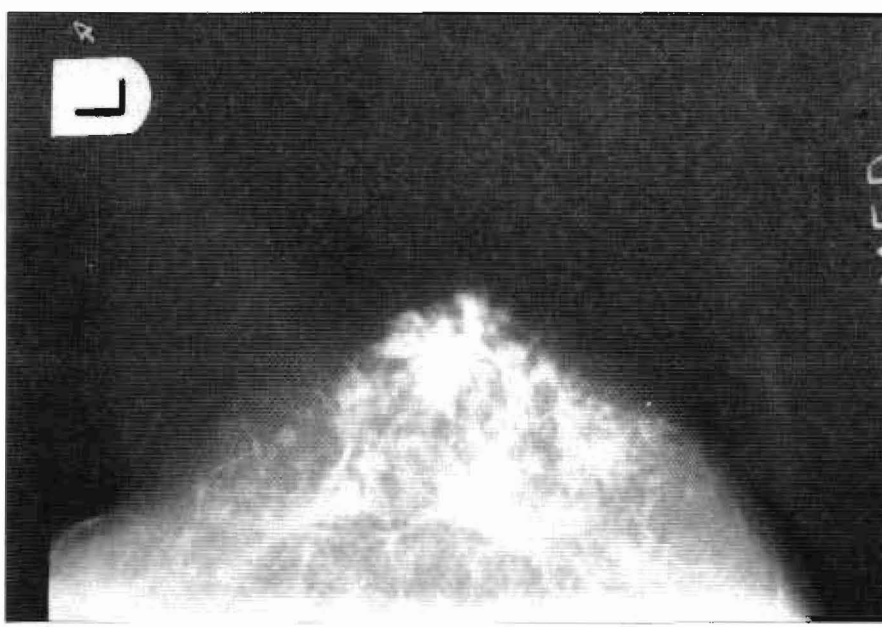

Figure 1.2: Histogram-equalized version of the original mammographic image GML1, shown in figure (1.1). The histogram was made from the pixel values within the breast area only.

- Masses with blurred edges are malignant, but edge enhancement can change these blurred edges into sharp edges indicative of benign disease.
- Calcifications are characterised by acute edges, and therefore their appearance can be created through edge enhancing.
- The shape of individual calcifications is used to differentiate benign from malignant calcification and can be distorted by inappropriate enhancement.
- Ducts and some fibrous structures appear as rough linear structures in mammographic images. Edge or contrast enhancement can cause these structures to have sharp edges, and thus the appearance of vessels.

Contrast and edge enhancement can be particularly dangerous since the image they produce is often grossly similar to the original, and the radiologist will therefore use his/her normal pattern recognition techniques to look for normal signs which might have been altered slightly. On the other hand, a radiographic technique such as xeroradiography, which is renowned for its edge enhancement, produces images which are substantially different from the original, and the radiologist is therefore alerted to use different recognition techniques.

Performing image enhancement in the frequency domain is another technique ruled out for mammographic images. Many mammographic signs are spatially localized and are not therefore localized in the frequency domain, making the application of any kind of band-pass filter unpredictable.

Of the conventional techniques, histogram-stretching would appear to be one of the most reliable, owing to its apparent simple function. However, two examples show this is not so. Stretching techniques usually assume that it is a good idea to fill the entire range of pixel values (usually 0-255). Many terminal screens do not show structures or contrast in low pixel values (typically 0-40). This means that if part of the visible original image is mapped to the low pixel values, the structures in the original disappear. Figure (1.3) shows a stretched image in which information has disappeared.

The second example of why stretching techniques are sometimes not advisable stems from the fact that the biggest danger to diagnosis comes from greatest "enhancement". Consider a flat image, with very low dynamic range. Enhancement to produce an image with wide dynamic range will necessarily amplify changes, possibly out of all proportion. Consider a breast image with an absolute range of pixel values of 50. Stretching this image to fill a range of pixel values from 0 to 250 requires stretching the pixel value range by a factor of 5. Consequently, two pixels with a difference of only 1 pixel value in the original image (quite possibly due to noise) have a difference of 5 in the stretched version, and this difference might be perceivable.

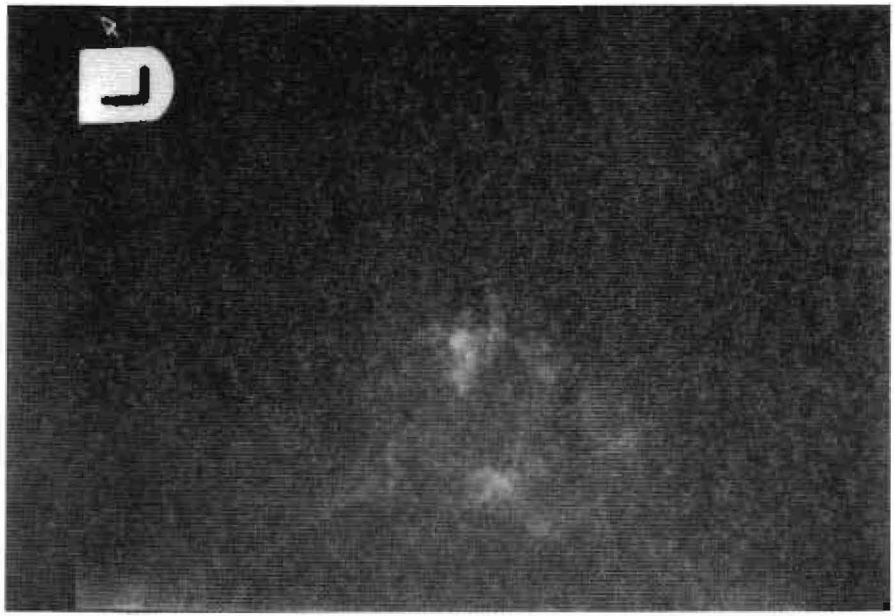

Figure 1.3: This is a linear stretched version of image GML1 in figure (1.1). The minimum and maximum pixel values in the original breast image were stretched to 0 and 255. The information in the darker pixel values has been lost, because they have been mapped to pixel values which appear black on the terminal screen.

Of course, with the use of all these techniques the radiologist still has the original image to check, but needing to do this shows a lack of trust in the enhancement. Having to consistently check the original images also reduces the radiologist's willingness to use the system, as he/she wastes time waiting for enhancement only to have to go back to the original.

Whatever technique may be used, it is important to remember that radiologists usually view mammograms in pairs: left and right mammograms are scrutinized for asymmetry; mammograms from different views are used to check signs; mammograms taken over time have signs compared. It is therefore of the greatest importance that enhancement of the images in each pair is in some way similar.

1.3.4 Analysis of enhancement

Ad-hoc enhancement techniques might be deemed reliable if it were possible to analyse exactly what they were doing in terms of the viewer's perception, but in many cases this is not possible. Common methods of analysing enhancement use Fourier analysis, entropy, histogram analysis, contrast measures, and image subtraction. Whilst useful, none of these measures can provide a full assessment.

The power spectrum might show the frequency enhancement given by an algorithm, but when the signs are spatially localized this is difficult to interpret. Histogram analysis and entropy measures both show the spread of the pixel values over the available grey scale, but as has been illustrated this is not a good measure of mammographic image enhancement. Subtracting the enhanced image from the original shows gross differences, but the resultant image has to be displayed, and often requires a transformation in order to be visible. This transformation inevitably amplifies the differences between the two images, possibly out of all proportion to the perceived differences.

Physicists often use a measure of contrast to analyse the quality of a radiographic image. However, contrast is invariably studied in terms of a small bright object upon a darker background, and in this situation accurate contrast measures are known. For images packed with information, such as mammograms, contrast measures can only be guessed at and are therefore not suitable for analysis of enhancement in a safety-critical application.

Another way of assessing image enhancement is to perform a clinical test comparing the results of diagnoses from conventional mammographic images to the results from diagnosing from enhanced mammographic images. Whilst this kind of test is necessary, it is expensive and needs careful selection of the test population.

1.4 Model-based image enhancement

1.4.1 Introduction

Reliable and robust image enhancement algorithms can be derived from a model of the imaging process and degrading factors. The robustness of such an algorithm comes from degrading effects being present in all imaging systems. The reliability of model-based algorithms comes from knowing in practice what should happen, and from choosing thresholds and variables from the physics of the system.

A model-based approach to algorithm design allows explanation to the radiologist, or radiographer, of what the computer is doing to the image in terms which they can

understand. This ability to explain is vital to building up the trust and confidence of the clinicians in the system. The potential benefits of model-based work can be judged by asking the clinician: "If this were possible to do in practice would it improve the image, and would it help diagnosis?".

The model-based approach is particularly appropriate in mammography because the imaging process is highly complex and there are many factors which degrade the image. Although the complexity of the process also necessitates that the model is only approximate.

Modeling the imaging process with a view to enhancement is only worthwhile if it is possible to obtain quantitative values from the digitized images. This requires that the digitized mammograms are of an exceptionally high quality, and that various stages of the imaging process are suitably calibrated.

This thesis develops a model of the mammographic process which is applicable to digital images. The model is different from conventional mammographic models because it has to take into account geometry and spatially varying factors, as well as use calibration to overcome film processing variations. Further to the overall model, a detailed model is proposed for the key degrading factor: scattered radiation. With the complete model, significant image enhancement is achieved in a fashion which is robust, reliable and can be explained to a radiologist. Some of the results and ideas in this thesis have previously been presented by us in [44], [45], [46], [47], [48], [49].

1.4.2 The model

Mammographic imaging process

Figure (1.4) is a schematic representation of the components of a screen-film mammographic system. When a mammogram is performed, a beam of low energy x-ray photons is directed towards a compressed breast. This beam is filtered to remove the low energy photons and collimated to the area of interest. The intensity of the beam exiting the breast is related to the thickness and type of tissue which attenuates the photons. On the basis of the x-ray attenuation coefficients we model the breast as consisting of mainly fat and "interesting" tissue (fibrous, glandular, cancerous), with calcium sometimes present. The x-ray photons leaving the breast have to pass through an anti-scatter grid before reaching a phosphorous intensifying screen. If the x-ray photon is absorbed in the screen, light photons are emitted by the phosphor and these light photons expose a film which is processed to produce a mammogram. The exposure to the breast is stopped once an automatic exposure control, positioned under a section of the breast, has received a set exposure.

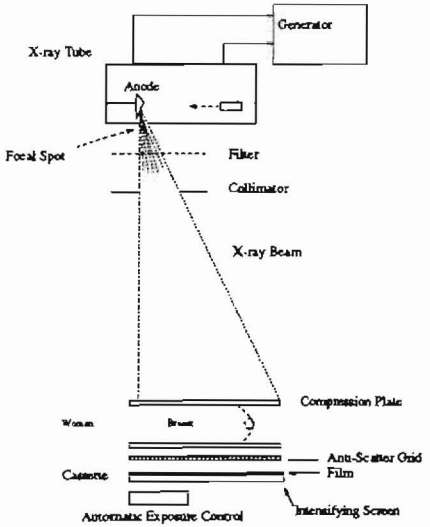

Figure 1.4: Schematic representation of mammographic system.

This description of the mammographic imaging process is highly simplified and omits mention of a number of factors which significantly degrade the mammogram. These factors include: scattered radiation, "beam hardening", and sometimes poor exposure due to the automatic exposure control being inappropriately located. A number of additional factors make it difficult to analyse mammograms quantitatively. These include varying processing results when developing films (which might also be called a degrading factor), system geometry, and the "anode heel effect".

Although mammography will become digital in the not too distant future, the model as described will still be relevant because some of the same degrading factors will be present. Furthermore, there will be a large number of old films which will require digitizing.

Varying processing results

To obtain quantitative values from the mammographic images the film processing stage must be calibrated. This we have achieved by performing an exposure of a lucite step wedge shortly before the actual mammogram is performed and processed. The original image can then be transformed to an image representing the relative energy imparted to the intensifying screen over an area corresponding to a pixel. Figure (1.5) shows the

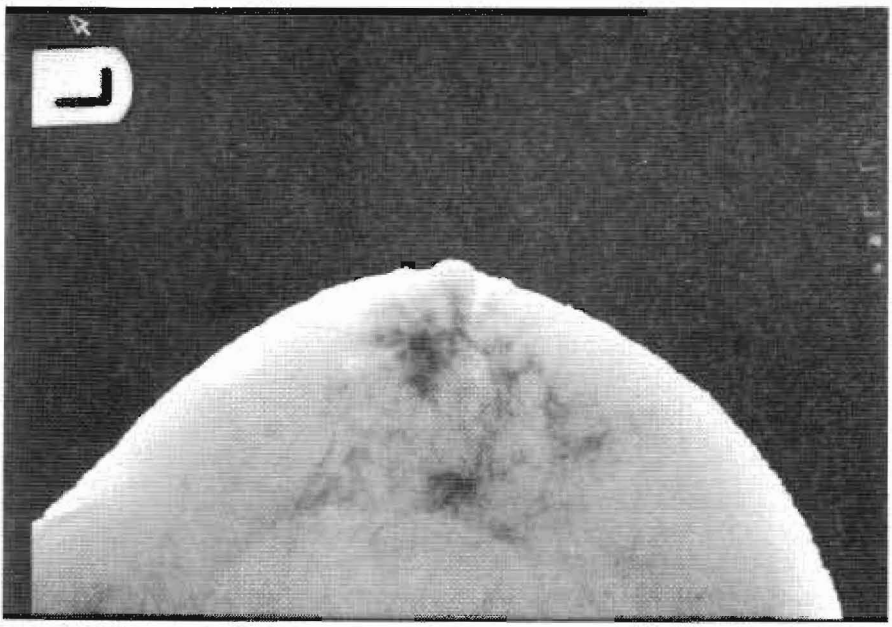

Figure 1.5: The energy imparted image of the original shown in figure (1.1). This image represents the energy which must have been imparted to the intensifying screen over each pixel to give the original image. The area outside of the breast image has been kept dark, it is in fact exposed to the full incident radiation and should therefore be bright white.

relative energy imparted image which corresponds to the original image in figure (1.1).

Anode heel effect and diverging x-ray beam

The anode heel effect and diverging x-ray beam cause the intensity of the incident radiation to vary spatially across the breast. The reduction in incident intensity can be as great as 25% from the back of the film towards the nipple. This variation is usually accepted on the assumption that the breast is less thick and less dense towards the nipple and therefore a reduction in the incident intensity gives a more even contrast in the film. The incident intensity variation can be seen, and compensated for, by performing a low exposure mammogram with no object present.

Scattered radiation

As the x-ray photons travel through the breast they can pass through the tissues freely, be absorbed, or be scattered. The x-ray photons which pass freely through the breast constitute the primary signal, and this contains specific information about the x-ray attenuating properties of the breast tissue. However, scattered photons also cause exposure to the film, and in this case the signal does not contain useful information. The effect of scattered radiation on the final image is often described as causing an overall fog. We consider scatter to be the key degrading factor in mammography, and present two models of it.

Scatter is initially modeled as being a uniform flood of radiation across the image, after the image has been compensated for the spatially varying incident radiation intensity. This assumption corresponds to the energy component imparted to the intensifying screen attributable to scatter being constant. From this the difference in the primary energy component can be calculated between any two pixels, and this difference transformed back to an image of a similar style as a mammographic image. The back transformation requires the choice of an offset value, which is set to optimize the dynamic range of the final image. Figure (1.6) shows the result of removing a constant energy component from the image in figure (1.1). This model is shown to enhance mammographic images with certain well-defined properties. However, it does not require an estimation of the scatter component and this is necessary for the model to be extended.

The second scatter model is based upon a conjectured relationship between the scatter component at the centre of a neighbourhood and the energy imparted in the neighbourhood. The percentage of the total number of scattered photons reaching the centre from each location within the neighbourhood, when an anti-scatter grid is not used, is found for a homogeneous block of tissue from empirical data. Application of grid transmission formulae provides the percentages for when a grid is used. This process provides a weighting mask where each entry represents the percentage of scattered photons coming from the volume of tissue directly above the pixel. This weighting mask is then convolved with the energy imparted image to give a value used as input to a scatter function which outputs the relative scatter component. In effect, the convolution sum is a quantitative measure of the local tissue composition and placement. The scatter function is found by using measured breast thickness, breast exposure in mAs and three calibration values. There is one further complication and this is the extra-focal radiation and breast edge effects which cause a large increase in the scatter component at the breast edge. This is modeled by selecting a value of the energy imparted for when the mask falls outside of the breast area and on the film.

Once the scatter component has been calculated it can be subtracted from the original

Figure 1.6: The result of removing a constant scatter component from the image in figure (1.1). The removal requires the use of an offset which is set to give an optimal dynamic range.

energy imparted to give the primary component. It is then necessary to display the primary component in a form suitable for a radiologist. The found primary component cannot be used to expose a film directly because it is too small to create a visible image. The approach taken in this thesis is to model the automatic exposure control. An original image is shown in figure (1.7) and the result from the weighted scatter model is shown in figure (1.8).

Beam hardening

Despite filtering, the x-ray beam is still basically polyenergetic. As the photons travel through the breast, the lower energy photons are attenuated and the average photon energy rises; this is termed "beam hardening". The consequence of this is a loss of contrast in dense areas of the breast as compared to fatty areas. To model a mammographic examination with a monoenergetic beam requires the removal of the scattered

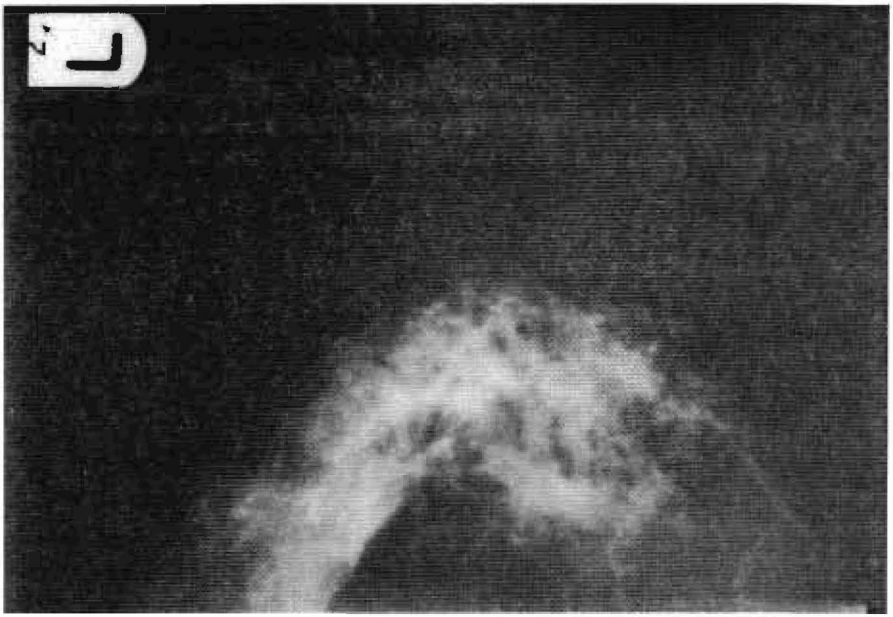

Figure 1.7: Original mammographic image MML1.

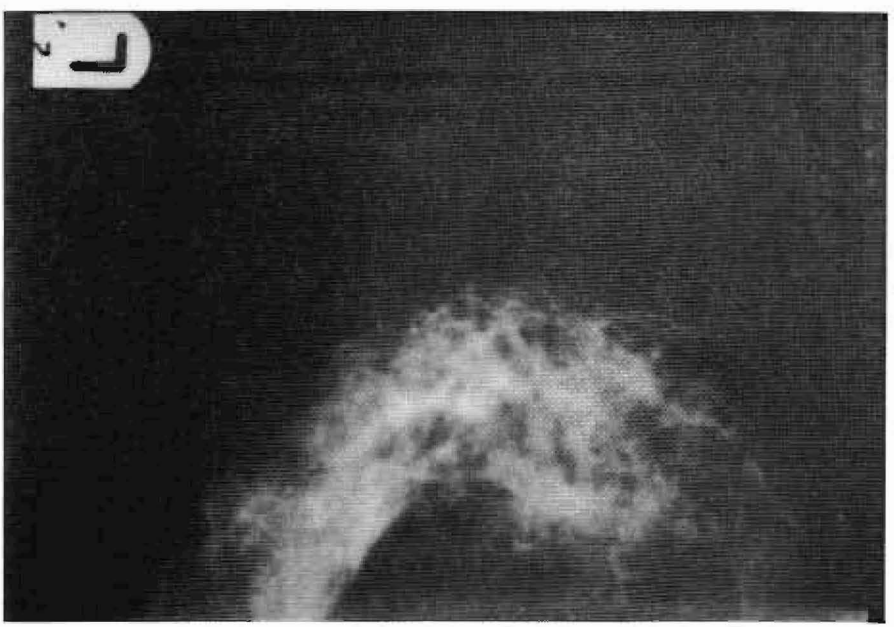

Figure 1.8: The result of removing a weighted scatter component from the image in figure (1.7). After removal, an automatic exposure control model is used to create a visible image.

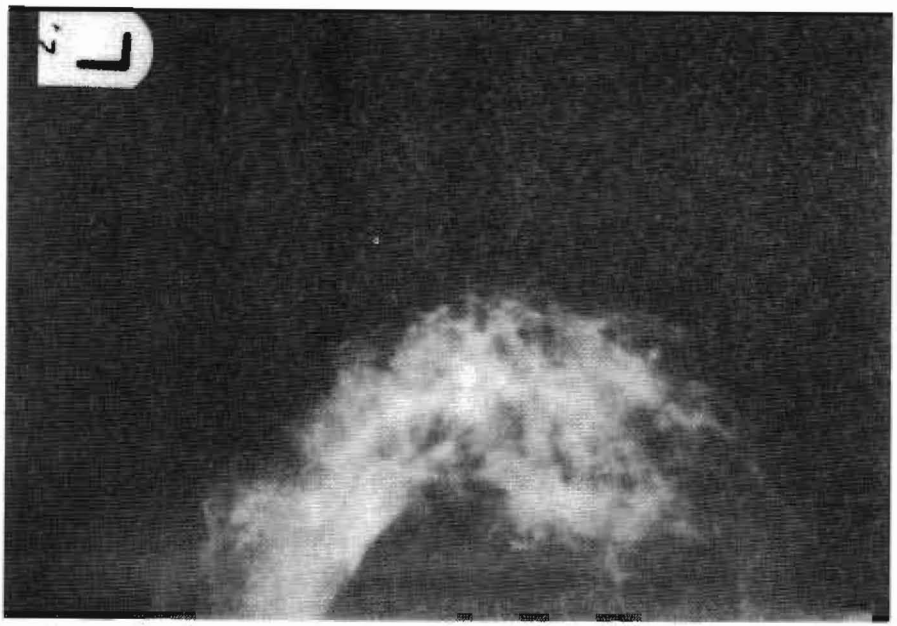

Figure 1.9: The result of performing a monoenergetic theoretical examination after scatter removal on the image in figure (1.7). The photon energy in the simulation was 19keV.

component and quantitative measures of the breast. The quantitative measure which is used is the thickness of interesting tissue which must be present to give the observed attenuation. Once this measure has been calculated, a monoenergetic examination with a theoretical automatic exposure control is used to produce a mammographic style image. The choice of photon energy for this examination is important as it determines the contrast in the final image. Figure (1.9) shows the result of performing a monoenergetic examination after weighted scatter removal. The choice of photon energy in practice is restricted by dose and noise considerations, which can be ignored in theoretical work aiming at image enhancement.

Automatic exposure control

The automatic exposure control can be modeled as a unit which terminates the exposure once a certain average film density has been reached in the area of interest on the film.

In reality the automatic exposure control is set to terminate the exposure once a certain energy has been imparted to it.

The automatic exposure control, while necessary, can give poor images because of early termination of exposure due to a number of reasons, including inappropriate positioning. Figure (1.10) shows an original image which is under-exposed due to the automatic exposure control lying under the fatty tissue near the back of the breast, rather than under the dense tissue nearer the front. Figure (1.11) shows the same image with the breast re-exposed theoretically to give a darker image.

1.4.3 Checking the model

Due to the number of approximations and assumptions that have to be made in modeling, it is important that the results are checked against experimental data. The results in this thesis are checked by comparison with published empirical data, and by studying the thicknesses of interesting tissue calculated.

1.5 Breast compression

The benefits of breast compression in mammography are well known: reduction of motion artifacts by immobilizing the breast; reduction of geometric blur; reduction of film density range through more uniform breast thickness; reduction of scattered radiation; improved separation of tissue structures through increased projected area; dose reduction. Since breast compression is an integral and varying part of the mammographic process we became concerned about the reliability of image analysis routines when faced with mammographic images taken at varying compressions. This reliability is important when the mammograms are performed by different radiographers, as the degree of compression is not standardized.

To investigate, we initially tried to predict the changes which would occur in the mammogram with different breast compressions. However, this proved to be difficult and totally dependent on the specific tissues within each breast. This led to the idea of performing mammography at different breast compressions in order to try and determine the hardness and mobility of the breast tissues from the change in mammographic appearance and position. Figure (1.12) shows a mammogram of a breast compressed to a thickness of 5.15cm, and figure (1.13) shows a mammogram of the same breast compressed to 5.8cm. These mammograms were obtained as part of a clinical trial at the Churchill Hospital in Oxford, which is trying to ascertain if diagnostic accuracy can be increased by considering the physical properties of the breast tissue attainable by

Figure 1.10: An original mammographic image. The automatic exposure control lies beneath the fatty tissue at the back of the breast and the image is therefore underexposed.

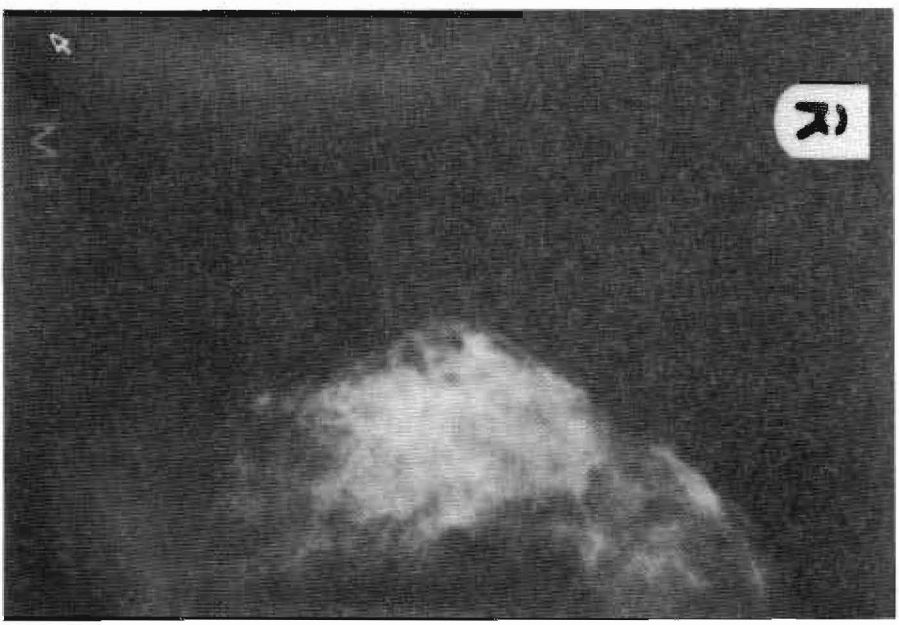

Figure 1.11: The automatic exposure control has been set to give a higher exposure in a theoretical study to the breast in figure (1.10). It could equally have been moved forward to go underneath the dense tissue.

taking mammograms at different compressions.

1.6 Overview of thesis

This introduction has explained the reasons why we believe a model-based approach is viable and vital in the enhancement of mammographic images. Chapter 2 discusses the approach in relation to the computer-aided mammography problems which have been identified and tackled by other researchers. This critical literature survey stresses the importance of considering how the images were formed, and notes the potential shortcomings of previous work.

Chapter 3 presents the model that we have developed for the analogue mammographic imaging process, and states the assumptions and approximations which inevitably have to be made. This chapter explains the degrading effects which are present in mammography. The next chapter transfers the model to the digital domain, and presents the fundamentals of applying image processing to mammography, including digitization, an automatic exposure control model and compensating the images for the spatially varying incident radiation intensity. With the overall model explained, chapter 5 proposes two models of scattered radiation, and shows the enhancement possible using them. This chapter ends with a theoretical simulation of a monoenergetic examination, and discussion of the perfect examination in terms of photon energy and information seen. Figure (1.14) shows the connections between chapters 3,4 and 5 in relation to simulating a scatter-free monoenergetic mammographic examination.

The idea of performing mammograms at different breast compressions is explored in chapter 6, and initial results of a clinical trial are presented. This chapter includes a review of published work on breast compression, and a discussion of breast anatomy. We believe such a discussion is vital because too often mammograms are considered independently of the three dimensional object they represent. Included in this chapter is discussion of the imaging effects of changing breast compression.

Chapter 7 shows in detail the enhancement achieved by the model-based algorithms developed in the thesis on several specific mammographic features, and also shows the same features with full and slightly less compression of the breast. The conclusions and possibilities for future work are found in chapter 8.

The appendices contain: (A) a glossary of medical terms; (B) details of the processes by which an x-ray photon is attenuated; (C) a review of the difficult task facing a radiologist when he/she diagnoses from mammograms; (D) a discussion about digitizing mammograms using a CCD camera; (E) details of the calibration of the x-ray system.

Figure 1.12: A photograph of a mammogram performed with breast ASR compressed to a uniform thickness of 5.15cm.

Figure 1.13: A photograph of a mammogram performed with breast ASR compressed to a uniform thickness of 5.8cm. There are obvious changes between this mammogram and the one performed with more compression (figure 1.12). In particular, the dense area in the bottom right of the photograph is seen to spread out with more compression.

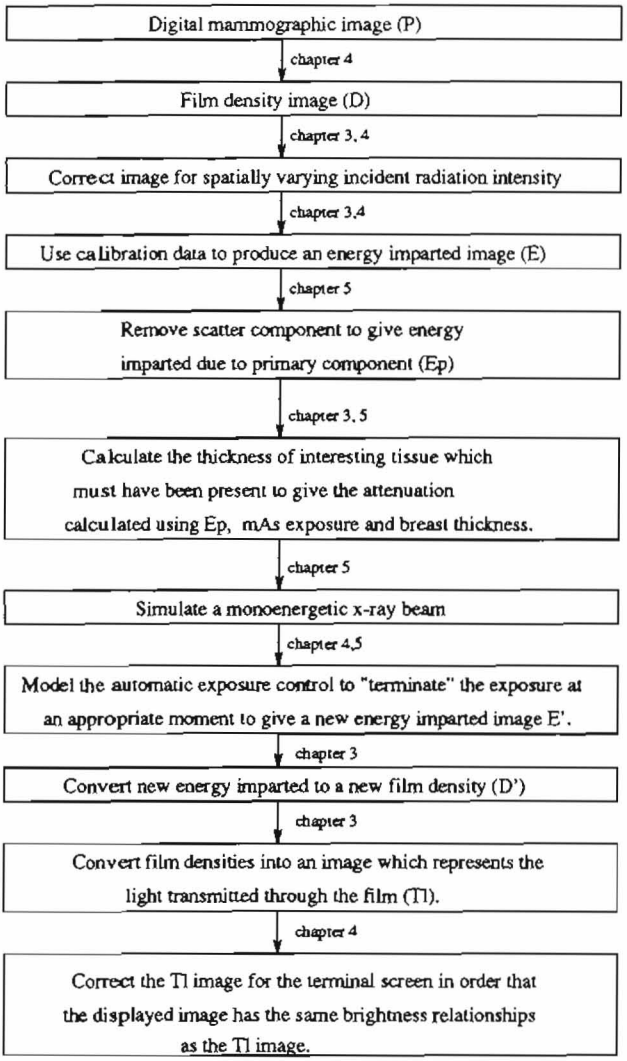

Figure 1.14: This is the process by which a mammographic image is transformed to show the image which would have appeared had a monoenergetic x-ray beam be used. The labeling between the boxes shows the chapter where the relevant ideas are developed. The simulation starts by removing the imaging parameters and scatter to give a quantitative measure of the breast tissue which is then transformed back as if a monoenergetic beam were used.

2

Computer-Aided Mammography

2.1 Introduction

Many papers have been published on the computer analysis of mammographic images, and several on their enhancement. The problems which these papers address can be categorized under the following headings:

- Noise
- Gain
- Segmentation of the breast image from pectoral muscle and background
- Registration and matching of breast images
- Detection of masses
- Classification of masses
- Detection of possible calcifications
- Classification of possible calcifications
- Evaluation of the parenchymal pattern
- Image enhancement

This chapter explains in detail each of these problems, and surveys the past attempts at solving them. It aims to show the applicability of a model-based approach, and the importance of our work to each specific problem.

Although the problems have been tackled in more than one way, comparing the results of different papers is difficult, if not impossible. This is because of differences not only in digitization but also in recording methods and the x-ray systems used. For example, the work reported in one paper might have been carried out on noiser images than in another, and thus records more false alarms when detecting calcifications; another might have images of far better resolution and thus be able to use the shape of the calcifications more reliably in the classification stage. Comparing recent results with papers written before 1980 is even more difficult, since the pre-1980 work was conducted either on xeromammograms or film-screen mammograms taken without an anti-scatter grid.

2.2 Noise

There are two types of noise in mammographic images: film noise and digitizer noise. Film noise is due mainly to the limited number of x-ray quanta, film granularity and random inhomogeneities in the intensifying screen. The number of x-ray quanta can be increased by using a greater exposure, but this increases the radiation dose to the breast. The size of radiation dose is linked to the risk of inducing cancer. In a screening programme, the risk of inducing cancer must be kept to a minimum, and therefore a compromise between film noise and radiation dose must be struck [51].

Some research has been done on noise suppression in mammographic images. Much of this work has appeared in papers dealing with the detection of calcifications; both noise and calcifications have high spatial frequency, and noise might therefore assume the same appearance as a calcification.

Conventional noise suppression techniques have been applied to mammographic images. Chan et al. [14] looked for noise as being out-of-place in a neighbourhood and used the mean and standard deviation of the neighbourhood to try and detect it. Lai et al. [62], in a paper detecting masses rather than calcifications, tried median filtering, selective averaging and selective median filtering. Most researchers have tended to avoid this kind of technique because of the smoothing with which it is associated and thus the risk of removing calcifications.

The high spatial frequency of noise argues for noise removal in the frequency domain. Chan et al. [16] claimed that noise is of a higher frequency than calcifications, and backed this up by studying the power spectrum of calcifications with the background

removed manually. On the basis of this study they applied a band-pass filter to remove the noise, and later derived a box-rim filter [15] to use in the spatial domain. Dhawan et al. [24] adopted a similar view of noise and applied a contrast enhancement function chosen to avoid high frequency noise amplification.

Since noise is typically of a high spatial frequency and randomly distributed across an image, a lower area bound on the proposed calcifications can be set [14], [15], [16], [23], [28], [106]. The digitization resolution is crucial because the lower area bound has to be small enough to pick-up the smallest calcifications, although there is a trade-off between noise and resolution.

Noise is extremely unlikely to be spatially localized, unlike most clusters of malignant calcifications, and so a lower bound on the number of calcification particles within a certain locality is a powerful noise suppression measure. The bound has to be chosen carefully and the calcification detection scheme has to be good, since noise is quite likely to produce a number of candidate particles within a certain area.

In their paper dealing with extraction and measurement of lesion edge blur, Richter and Claridge [81] [82] take the original step of converting from cartesian to polar coordinates in order to smooth the image tangentially so that the profile of the lesion in the radial direction is preserved.

Karssemeijer et al. [58] use the underlying physics of noise, both radiographic and digital, to work out a grey-level transform that makes the absolute noise level constant across their CCD images. Their transform is reported to lead to more reliable analysis when thresholds are applied to measures calculated locally.

We believe that conventional noise suppression techniques based in either the spatial or the frequency domain are doomed to failure for mammographic images due to the necessity of not smoothing the image and the localised nature of calcifications. However, the techniques specific to digital mammography provide solid ground for noise suppression, although the values for the bounds (especially the size of calcification) have to be carefully chosen in order to take account of changes in geometry, and, as we show in chapter 6, changes in the degree of breast compression.

The work of Karssemeijer et al. [58] provides a good example of a model-based approach producing a novel method. Furthermore, as the authors recognise, noise removal is not necessary for thresholding local measures if the absolute noise level can be made constant. It is interesting to note that whilst their method serves its purpose for image analysis, it does not necessarily enhance the image to the viewer.

2.3 Gain

Many different factors influence the level of the pixel values and contrast in mammographic images. These factors range from the type of film, processing and exposure to the degree of breast compression and method of digitization. These influences mean that mammographic images cannot be assumed to have any particular distribution or range of pixel values. This inevitably rules out using the given pixel values, for example as thresholds, or for direct comparison between images.

Some authors have tackled the gain problem in the conventional ways: thresholds are set from histograms [1], [14], [43], [62], [106]; ratios are used [1], [28], [94]; some form of image normalization takes place [59], [62].

A mammography-specific way of overcoming gain is to try and use the symmetry between left and right mammograms noted by radiologists [43], [59]. However, whilst possibly removing the effects of different processing conditions, the problem of gain still exists as witnessed by the differences in exposure and breast thickness between left and right breasts. In any case, symmetry is much more qualitative than can be dealt with by simple subtraction between left and right breast images.

Texture measures are particularly susceptible to gain, and texture analysis has been applied to mammographic images to try and describe the global pattern of the breast image. Miller and Astley [68] normalize their texture measures, whilst Magnin et al. [66] choose texture measures that depend less on the imaging system rather than run the risk of removing important inter-mammogram variations by normalization in an ad-hoc fashion. Caldwell et al. [8] address this issue by showing that the algorithm they propose to compute fractal dimension is robust to changes in the recording system.

The variations in system gain due to different exposures, film processing conditions, and digitization can be removed using the underlying physics; it is the variation of breast thickness which is the major problem. It might be best to transform each mammographic image to some standard breast thickness and exposure; this can be performed with the model developed in this thesis. However, any relationship between spatial dimensions and feature brightness might be lost. This is discussed further in section (8.2.11).

2.4 Segmentation of breast image from pectoral muscle and background

The breast needs to be segmented from the pectoral muscle and blank film area for several reasons: it reduces the area of the image to be examined; it facilitates registration of left and right breast images; and it allows different analysis and enhancement algorithms to be applied to the segmented areas.

The image segmentation required depends upon the mammographic view. Mammographic images taken from either the cranio-caudal, medio-lateral or medio-lateral oblique view need to have the breast image segmented from the film image, and possibly also the chest wall image. Medio-lateral oblique mammographic images also require that the breast image be segmented from the pectoral muscle image. Accurate segmentation is vital in applications which require minimum or maximum values from the breast area, or which make assumptions only valid within certain areas.

Segmenting the breast image from the film is difficult for images taken by some CCD cameras. In these images, the breast edge tends to merge smoothly into the background. Segmenting the breast image from the film becomes trivial when the mammograms are digitized with a high quality scanner, although there will be curtailing of the breast edge as most scanners cannot pick up the full dynamic range of the mammographic images.

To segment the breast from the film and chest wall on xeromammograms, Kimme et al. [59] used a ridge following algorithm. Hand et al. [43] made this process more robust by using candidate cells and choosing the best when conflicts arose, although they reported exclusion of 2 small lesions from the breast image. Semmlow et al. [87] in a follow-on from this work reverted to finding the chest wall boundary from the image placement. They used a nipple detection filter to gauge some idea of the breast/film boundary. This filter was sensitive to concave shapes characterized by large vertical gradients with rough textures on one side and smooth textures on the other.

The pectoral muscle appears in a medio-lateral mammographic image as a bright wide band slanted across one corner of the image. Detecting the slanted line between the muscle image and breast image is reported to be problematic even with high quality digital images, although Miller and Astley [68] report some success using a Hough transform.

2.5 Registration and matching of breast images

Left and right breast images need to be registered and matched to check for asymmetry, normalise the image values, and detect change over time. Registration and matching of the images are interlinked because registration might require scaling, and this cannot be done without consideration of how the matching is to be performed.

Registration of breast images is difficult because of differences in shape, size and relative position. These differences arise from the left and right breasts being physically different and the degree of compression changing. Matching of the breast images is difficult, even after registration, because it is unclear what exactly should be compared and this is compounded by the problem of gain. This suggests that qualitative matching rather than quantitative matching should take place.

Registration of fixed rigid bodies within images takes place by the selection of corresponding control points in each image, which are then aligned. This process is much harder with mammographic images because scaling is required, and internal control points cannot be used because one of the aims is to detect asymmetry.

The simplest approach to registration is to spatially reverse one of the images, and to align left and right breast image boundaries as well as possible. This approach ignores the possible differences in size and shape of the images, and just compensates for differences in position. Hand et al. [43] aligned the breast boundaries by detecting and aligning the nipple areas and then minimizing the least squares error between the boundaries. To cater for alignment errors, they smoothed the differences between the statistical feature values which they calculated. Winsberg et al. [107] and Giger et al. [37] both align the images manually, and Giger et al. check later for false alarms due to misalignment.

Noting that the left and right breast images are quite commonly different in shape, size and relative position, Kimme et al. [59] assumed that each section of the breast image would, if normal, match a similar section of the other breast image. They enclosed each breast image within a triangle and divided the triangle into a specific number of strips, which were further divided into a specific number of rectangles. Statistical feature values in correspondingly numbered rectangles were then compared.

More recently, Zhou and Gordon [111] perform a geometric unwarping operation based on the manual input of control points from the left and right mammographic images. The operation is reported to be time consuming and the control-point extraction not easy to automate. Lau and Bischof [65] simplified and automated the process by using only three control points in each breast image. The control points were the nipple and the corner points between the breast edge and chest wall. Using these

control points, one breast image is rotated, translated and scaled to register with the other.

The problem of matching left and right breast images to determine asymmetry is ill-defined. Whilst translation and rotation are grey-level preserving operations, scaling is not, and the benefits, if any, of trying to register the images accurately with scaling are unclear. The only reason to use scaling would be that statistical feature values calculated over the same size areas could be compared directly between breast images. Since scaling is only necessary to make one breast image cover the other, the region not being covered without scaling is the boundary region, which is generally uninteresting except for the possibility of skin thickening. In our opinion it might be far better to do a fast, approximate alignment and then compare features in a qualitative fashion, or to take the approach of Miller and Astley [68] to detect regions of interest and then compare these regions.

The problem of registration and matching of mammographic images is important not just for asymmetry and normalization, but also because of the possibility of using the same technique to find change in an individual breast image over time; a task which has been given no attention from the computing community but which clinicians always do. Registration and matching over time might not be easier than comparing left and right breast images because the degree of breast compression might not be the same.

Although asymmetry between left and right breast images is often quoted as an important sign in diagnosing breast cancer, it should be noted that radiologists are able to diagnose from just one mammogram. This situation arises with women who have had one mastectomy.

2.6 Detection of masses

The usual approach to the detection of malignant masses is first to detect potential sites and check for false alarms, and then to classify the sites into malignant mass or benign mass. The computer literature on mass detection contains many references to asymmetry [65], and the use of values from both left and right breast images. We consider the actual measures and motivation to be important, rather than the use of data from both breasts images which we believe might be detrimental due to the alignment and gain problems discussed previously.

The range of masses which it is required to detect is wide. At one end, it covers those that are characteristically benign with rounded appearance and sharp edges, through at the other end to characteristically malignant with a small, bright central region and bright linear structures radiating outwards (spicules). In between these two

extremes there are masses which have a mixture of benign/malignant characteristics. For example, one type of malignant mass has a well-defined edge around most of its border, but has an ill-defined edge occupying the remainder.

A classical approach to general mass detection would be to apply an edge detector and then to join the edges seeking closed areas. This approach is not appropriate for mammographic images because the edges of interest often have more in common with ramp edges than step edges. This is illustrated by considering an invasive tumour which is slowly growing into the surrounding tissues.

Most radiologists when describing a mass refer to an "area of increased density". In terms of the mammographic image this is an area of increased brightness, and since brightness is easy to measure it is a popular mass detection measure [43], [59], [65], [107]. However, brightness can be misleading as often the mass is only as bright as the surrounding tissues. Most researchers combine a number of measures, including brightness, into an overall measure of suspiciousness or activity.

Many researchers use roughness in a local area as a measure for detecting masses. Roughness is dependent upon the type of examination performed. Xeromammograms tend to be a good deal rougher and appear to have more contrast than screen-film mammograms (due to their high-pass nature). Consequently, spicules and increased ducting in xeromammograms respond well to roughness measures [59]. Other researchers have used roughness as an indicator of activity [43], [87], [107]. For screen-film mammographic images, Lau and Bischof [65], use a normalized local variance measure to indicate roughness due to the structure of stellate lesions, or the presence of well-defined edges.

Due to the ambiguous evidence being provided by their brightness and roughness measures for large homogeneous masses, Lau and Bischof [65] used a combined brightness-roughness measure. This measure provided different values for the various tissues: fatty tissue has a low brightness-roughness measure since it has low brightness and low roughness; glandular tissue has a low brightness-roughness measure since it has medium-high brightness and often high roughness; large masses have a high brightness-roughness measure since they are always bright and have a low roughness value.

Masses tend to be rotationally symmetric, so that a local measure of rotational symmetry might be a suitable mass detector [34]. General rotational symmetry measures have the advantage of a purely asymmetric approach in not needing to define precisely (at least initially) what to look for. The lack of directionality in masses is exploited by Lau and Bischof [65] to remove false alarms due to highly oriented structures such as vessels.

In a classical approach to circumscribed mass detection, Lai et al. [62] used a template matching technique based on the assumption that circumscribed lesions are circular, uniform and brighter than the surrounding area. They tried templates of various sizes which were high-pass and approximately rotationally symmetric:

```
          -1  -1  -1
      -1  -1   0  -1  -1
  -1  -1   0   1   0  -1  -1
  -1   0   1   1   1   0  -1
  -1  -1   0   1   0  -1  -1
      -1  -1   0  -1  -1
          -1  -1  -1
```

If a mass is at all visible, some neighbourhood containing it will have a bimodal distribution. Kimme et al. [59] use the difference in bi-modal peaks over a neighbourhood as a detection measure, whilst Lai et al. [62] use bi-modality as a false alarm check on the masses proposed by their template matching.

The key to many of these detection measures is the choice of neighbourhood size. The neighbourhood size will vary according to the size of the mass being searched for. If the neighbourhood size is too small, then it will probably not be able to contain large masses, and thus record false-negatives. If the neighbourhood size is too large, small masses will have little effect on the measures and consequently be missed. The range of sizes of features within mammographic images indicates that parameterized features will be required.

The need to search mammographic images for small difficult lesions tends to hide the problem of looking for larger lesions. The variance in lesion size is one of the major difficulties to be faced in the detection of masses, and it is vital that the radiologist does not see the computer missing obvious large lesions, even if the small lesions are detected.

The idea of using more than one detection measure (or cue) is appealing, but as pointed out by Lau and Bischof [65], the more measures which are used, the more likely it is that unwanted structures will respond to at least one of them, and consequently more false positives will be recorded. This is especially true if the measures have not been well thought out.

The detection of masses is still in its infancy compared to microcalcifications and this reflects how much more difficult it is. The reason for this difficulty is the number of similar patterns which can occur due to normal tissue, and the fact that masses have approximately the same x-ray attenuation coefficients as fibrous and glandular tissue. Better results might be obtained from the mass detection stage if the features which are

obviously not masses are removed before processing.

2.7 Classification of masses

One of the most common signs reported by radiologists to distinguish between benign and malignant masses is the lesion edge blur: benign masses tend to be well-defined and have sharp edges, while malignant masses tend to have blurry edges. Lai et al. [62] tested for a blurred edge by checking for a gradual drop in their suspiciousness values as the size of their detection template increased. Richter and Claridge [81] [82] try to derive quantitative measures of lesion blur in order to provide an objective measure. Edge blur is quantified by considering the Gaussian smoothing needed to make an ideal sharp edge into the recorded edge (similar to the idea used in auto-focus control). Fredfeldt et al. [34] apply the Sobel operator and then perform a binary morphological closing operation; the mass is considered suspicious if a complete boundary does not result.

Spiculations give a malignant mass an irregular, rough boundary. Consequently, checking the smoothness of the boundary of the suspicious mass is a common classification technique. Giger et al. [37] used two measures of this smoothness. Firstly, they smoothed the spatial coordinates of the boundary and calculated the standard deviation of the fluctuation of the original boundary from this smoothed version, and then they smoothed the boundary using binary morphology and studied the area change. Ackerman et al. [1] rather than checking for boundary roughness, checked specifically for spiculations by studying the relationship between radials from the centre of the mass and tangents at the boundary. Similarly, Hand et al. [43] check for gradients parallel or perpendicular to radials. Determining the presence of spicules is difficult because any smoothing (to find the mass boundary for example) will tend to remove them. Furthermore, spicules are often long and very thin so that any technique based on area differences may not be able to reliably differentiate between spicule removal and general reduction in mass size.

Benign masses tend to appear more circular than malignant masses on mammograms. Ackerman et al. [1] calculated the area to perimeter ratio of the suspect masses to try and quantify the circularity, whereas Fredfeldt et al. [34] calculate the ratio of the circumference of the tumour to the circumference of the circle with the same area.

The apparent homogeniety of the appearance of benign masses compared to malignant masses was measured by calculating the roughness within the part of the image containing the mass by Ackerman et al. [1].

The extra brightness of some tumours would appear to be why the work of Smith

et al. [94] was reportedly so successful. They subtracted the film densities within the suspect mass from a linear approximation to the normal breast densities, and formed the "linear mass ratio": the ratio of the area of the circumscribing rectangle to the actual area found. This worked perfectly in differentiating adenocarcinomas (a type of malignant mass) from masses caused by fibrocystic disease. However, the authors were not confident of extending this work to cover other masses, and indeed were not sure why their method worked anyway ("the apparent success of the linear mass ratio is elusive").

The problem with much of this mass classification work is that no account is made for the imaging conditions and it is therefore highly unlikely that a particular statistic will correlate reliably with malignancy. In particular, the lesion edge blur is affected by scattered radiation, incident exposure, beam hardening, intensifying screen quality, focal spot size and breast compression. Only by keeping these factors constant can any reliable objective values be obtained, and that requires not only modeling the imaging process, but also taking account of breast compression.

2.8 Detection of possible calcifications

Calcification can be a sign of both benign and malignant disease. In some cases, calcification is the only indicator of cancer; often whilst the cancer is still non-palpable. For this reason, calcification is considered to be one of the key mammographic signs, especially with regards to screening which aims to pick up non-palpable lesions.

Calcifications usually appear in a mammographic image as small flecks brighter than the surrounding tissue due to the high x-ray attenuation properties of calcium. Particles of calcification usually appear in clusters, with some individual particles being as small as 0.1mm. The small size and high contrast give the detection criteria. Once all the possible calcifications have been detected, they are classified into malignant, benign, or false alarm.

The most common technique in papers dealing with calcifications has been to assess statistically the diagnostic value of a number of features using test cases, and then to choose the best combination (i.e. most indicative of malignancy). The values for the features usually come from computer calculation, but some researchers have the radiologist entering the relevant answers [36] [78], the computer then being used purely as a statistical correlation tool (a job suited to a neural net). As well as testing the potential for a computer to detect and diagnose cancer, these papers are also testing the notion that objective measures will be more consistent than subjective measures, and there should be feedback to the medical community from their results.

Due to the difficulties in picking out individual calcifications, many authors attempt to enhance them before analysis. Wee et al. [106] sharpened their images whilst Fox et al. [32] applied a matched filter to remove the background and enhance edges. The attempts by Chan et al. [16] for calcification detection have been centred on enhancing the signal, suppressing the signal, and then thresholding the difference. They enhanced the image using a filter matched to a typical calcification, and suppressed the signal using various different filters: median, contrast-reversal, band-pass. In their next papers [15] [17], they performed a detailed analysis of the imaging properties of the calcifications, including investigation of the power spectra, and used the results to derive more appropriate filters.

The high local contrast of calcifications is the key detection sign in most papers whether found by use of a local threshold, edge detector, local maximums, or a local roughness measure [1], [23], [28], [65], [97], [106]. Chan et al. [14] also thresholded the image globally to add an extra calcification check, this was in the knowledge that calcifications often appear as the brightest objects on the image (especially if the pectoral muscle image is either segmented or not present).

After initial detection, it appears that some algorithms do not pick-up the entire calcification. Wee et al. [106] and Fox et al. [32] both trace their detected calcification edges looking for a closed periphery, whilst Fam et al. [28] use region growing.

The main component in detecting possible calcifications is their relative brightness, and yet this varies according to the imaging conditions and degree of compression (as shown in section 7.2). It is surely then imperative that the imaging process is considered, as it is highly unlikely that an algorithm will be robust to a wide range of imaging conditions even if local measures are used. In particular, the use of a global threshold on locally calculated measures will be susceptible to spatial variations in the imaging conditions such as from the anode heel effect. There might also be a case for adjusting the thresholds according to the breast thickness under compression.

2.9 Classification of possible calcifications

It would appear to be relatively easy to detect all the possible calcifications within an image, but to do so without creating a large number of false alarms is far more tricky. The main causes of false alarms are noise and sharp-edged structures which also respond to the detection measures. Fortunately, individual calcifications and clusters of calcifications have a number of properties which can be used to differentiate malignant calcification from benign calcification and false alarms [35], [36], [92], [93]. A cluster of calcifications should have numerous, fine and irregular particles if it is to

be considered malignant; if it has few particles, or if the particles are circular or coarse, then it is likely to be benign.

The shape and significance of a calcification particle is determined by the cavity in which the particle is situated [101]: linear or branching calcifications tend to be in ducts (which are linear structures) and are often malignant; round calcifications tend to be in lobules (which are spherical structures) and are usually benign. Davies et al. [23] take the ratio of perimeter to area as a shape parameter. Wee et al. [106] use a measure based on the distance of the perimeter points from the centre. Fox et al. [32], as one of some 69 values considered, used the aspect ratio. The shape of a calcification is likely to be robust to breast compression; it is not expected that a linear particle can become circular or vice-versa. However, shape is difficult to use as a differentiating measure since the calcifications are so small that the digitizing process has to be extremely good to get any reliable shape measurements.

Lobular calcification can also present with a hollow centre. Tabar and Dean [101], in a paper extolling the virtues of determining the pathological processes which have given rise to the calcification, explain the hollow appearance as calcium settling around the sides of a lobule. Hollowness was one of the measures calculated by Wee et al. [106].

The easiest check on the validity of an individual calcification is size, in terms of both area and linear dimensions. False alarms tend to be due to large well-defined narrow objects (such as vessels) and since calcifications are small an upper bound on size is a suitable classifier [14], [15], [16], [17], [23], [28], [29], [106]. Similarly, noise is suppressed by only considering structures over a certain size. Again, to get reliable measurements requires exceptional digitization.

Individual calcifications are expected to have relatively well-defined edges due to their high x-ray attenuation. Davies et al. [23] calculate the ratio of perimeter squared to area in the belief that blurry edges will provide larger areas and thus a low ratio. They also apply a simple edge detector, as do Fam et al. [28], [29]. In a later chapter, we show how the acuteness of the edges of calcification particles changes with the degree of breast compression: a mammogram of a breast firmly compressed shows calcifications which are more blurred than in a mammogram of the same breast at less compression. This result casts doubt on whether the acuteness of the calcification edge is a reliable indicator of malignancy.

The local clustering of calcification provides more measures which can be used for classification. Since noise is unlikely to be detected as a local cluster, and benign clusters tend to have fewer particles, most researchers put a lower bound on the density of the cluster [14], [15], [16], [17], [23], [28], [29], [106]. In the circumstances, it might also be wise to check that there are not calcifications detected over the entire image.

Karssemeijer [57] takes a unique approach to the detection of microcalcifications by applying stochastic methods to their detection, and transforming the image prior to processing to get a constant absolute noise level across the image. He claims that detecting and then classifying is inadequate because unreliable detection messes up the classification; this is the basis for his use of an iterative stochastic method with labels propagated on the basis of local competition and cooperation. The labels are based on local contrast and shape. Long-range information is also accommodated to include the clustering criterion.

When mammographic images of the same breast from two different views are available, a check can be made to see if the calcifications are detected in both views. Spiesberger [97] assumes that the calcification pattern will correlate well between the two views, and finds a second order polynomial transformation to maximize the cross-correlation. The theory that calcifications should appear in both views is sound, but the assumption that the patterns will correlate well is debatable.

The main result from work on calcifications is that computers can detect all possible calcifications, but as yet an unacceptable number of false alarms are also being reported. This is encouraging, and it was reported by Fam et al. [29] that their system found 4 calcification clusters which the radiologists had not.

This discussion has highlighted the measures used most frequently in the detection and evaluation of calcifications. However, other measures have been tried and some of these have yielded contradicting evidence. For example, Olson et al. [73] and Freundlich et al. [35] both attempted to determine the average distance between calcifications for malignant and benign disease. Olson et al. [73] concluded that the mean of the distance is greater for malignant disease, whereas Freundlich et al. [35] concluded that the mean distance is less. We feel that this disagreement is symbolic of the computational work so far, in that the potential for using the computer as an objective measurer has been undermined by ignoring differences in breast compression and imaging conditions. As will be shown in the chapter on breast compression, the distance between calcification particles changes with breast compression and is therefore not a reliable measure.

2.10 Parenchymal pattern

A controversial sign of risk of breast cancer is the parenchymal pattern. Wolfe [108] classifies the parenchymal pattern of the breast into 4 classes:

N1 : Breast almost exclusively fat and connective tissue trabeculae. Up to 10% of the breast volume could contain dysplastic elements or visible ducts.

P1 : 11-24% of breast volume is visible ducts.

P2 : Breast volume contains 25% or more visible ducts.

DY : Dysplastic changes involve more than 10% of the breast parenchyma. If both visible ducts and dysplastic changes are present in the same breast, the woman is classified by the dominant category.

A woman in class P2 or DY is claimed to be more at risk than N1 and P1, with various probabilities.

The correlation between parenchymal pattern and risk is difficult to prove due to the inter- and intra-observer differences when classifying the pattern. For this reason, ways of making the computer an objective and consistent observer of parenchymal patterns have been attempted.

Texture analysis is an obvious way to try and quantify the parenchymal pattern, but is susceptible to gain. Magnin et al. [66] chose not to normalise their texture values for fear of removing the variations they were looking for. Instead, they chose texture measures less dependent on the imaging conditions: entropy, inertia (or contrast) and local homogeneity. They claim some correlation between their measures and risk, but not in the four discrete classes of Wolfe.

The main criteria of the Wolfe classes is the prominence or otherwise of ducts. Shadagopan et al. [89] attempted to find a figure for the duct area by using knowledge of the breast anatomy: ducts radiate outward from the nipple, frequently in a plane which is not parallel to that of a mammogram. They claim that the reason ducts are seen on a mammogram is because the walls become surrounded by collagen; however, the distribution of collagen is not uniform, and consequently neither is the apparent ductal distribution. In addition, the ducts not only overlap each other but also other collagen material, producing an irregular pattern. Thus they define ducts as being ill-defined light ellipsiods embedded in dark areas, or as linear structures forming clear elliptic spaces. They claim the range of ellipsoid shape and size is narrow. To detect these ducts they segment the breast image, find the nipple and then apply ellipsoid duct templates and from this calculate duct area. They report a continuous correlation between duct area and breast cancer risk.

Considering the mammographic image as three dimensional, with intensity being height, Caldwell et al. [8], [9] fitted a fractal dimension to each image. Apparently, the fractal dimension correlates with risk, although it appears to be more continuous than the four discrete classes which Wolfe proposed. Amongst uses for their method they speculate on finding the fractal dimension of mammographic images taken at intervals and using it to monitor risk, and using the fractal dimension of a baseline

mammographic image with which to suggest appropriate screening frequencies. The authors report only small change in the fractal dimension with different views of the same breast and also found that left and right breast images gave similar values. They showed that the fractal dimension has little variability with film processing, thus indicating that the value might be robust to varying imaging conditions.

Using the computer to quantify parenchymal pattern is interesting and important because the computer is being used as an objective observer for a task previously criticized because of the subjectivity involved. The fact that the mentioned studies have found some form of correlation between pattern and risk, when clinical trials have failed to do so consistently, indicates the possible success of using the computer as an objective observer. It is notable that this is the one area where the imaging process and some of the possible variations have been considered.

2.11 Image enhancement

Image enhancement is an obvious goal in any field where small, subtle signs are important, and the images are of poor quality. Mammography is a particular case in point, because although the images are of a high technical quality, they have to record a wide range of information (where the range is not known until after the mammogram is performed) and they are degraded by several factors in the imaging process.

Of the papers published on image enhancement of mammographic images, all make play of transforming film-screen mammographic images to xeromammogram-like images. This is seen as being desirable because xeromammograms show fine details and image calcifications with greater contrast, particularly in dense breasts. The transformation is made possible by xeromammography having poorer resolution than screen-film mammography.

Dhawan et al. [24], [25], [99], and Gordon and Rangayyan [38], [39] use adaptive neighbourhoods to define contrast, apply a function to the contrast measure, and then transform back. An adaptive neighbourhood is used to counter noise, rather than a varying enhancement threshold, because mammographic images have a wide gradient range and so it is difficult to use a threshold which rules out noise.

The contrast enhancement function used in [39] was the square root (their contrast measure gives numbers from 0 to 1), in [24] they investigated several other functions because the square root was found to enhance noise. The choice of function was prespecified in [25] based on the specific feature which it was required to enhance.

The neighbourhood size was fixed in [24], [38], [39] according to the first maximum of contrast with centre size; where contrast was defined using a central region and

surround of a fixed shape. The authors report that the fixed shape of the neighbourhoods was a source of creation of artifacts. Consequently, in [25] they use a centre and surround which could be of any shape.

All the papers claim significant image enhancement and note the enhancement is not just of edges, but objects and features as well. In [39] the high frequency enhancement was shown by comparing power spectra, in [24] grey level entropy is used to show that their images better utilize the grey levels.

More recently, Tahoces et al. [102] describe an automatic spatial filtering technique which they use to enhance both chest radiographs and mammograms. They simply smooth the original to varying degrees and then add back to the original before performing a non-linear contrast stretch. The smoothing and non-linear stretch appear to be chosen from trial and error.

The papers referred to in this section have dealt with cranio-caudal view mammograms where the segmentation of the breast image from that of the film is trivial. It seems likely that ad-hoc image enhancement of medio-lateral oblique mammograms will depend critically on the segmentation of the pectoral muscle image from that of the breast.

As was pointed out in the introduction, ad-hoc methods are unpredictable and therefore dangerous: the authors of the papers referred to in this section have themselves noted creation of artifacts and amplification of noise. The use of ad-hoc methods in a safety-critical application such as mammography seems particularly ill-considered when there are so many degrading factors which can be modeled.

2.12 Conclusions

Past researchers have concentrated on the detection of calcifications. Masses and disturbances in breast structure have hardly been considered. This is understandable given the difficulty in matching left and right breasts, and the ill-defined nature of the problems compared to calcification detection.

The use of the computer as an objective observer is reasonable, and one taken by many of the published papers with apparent success in quantifying the parenchymal pattern. However, the imaging conditions must not be overlooked, especially as it might be argued that the human observer, with all his/her subjectiveness, might actually be compensating in some fashion for the imaging conditions.

There has been little mention in the papers of the images actually used for the analysis. Many authors appear to work on film density images, where the pixel value is

linearly related to film density, probably on the basis that this is related to attenuation. This approach is possibly at odds with trying to model what the radiologist does, because the radiologist sees the light transmitted through the film, $T_l = I_l 10^{-D}$, where I_l is the intensity of the illuminating light, and D the film density.

The published image enhancement routines have been ad-hoc and therefore unpredictable. This is particularly true for the cases where the authors have found a useful enhancement technique in one field and then looked for applications in another field.

3

Mammographic Process Model

3.1 Introduction

Figure (1.4) showed a schematic representation of the components of a screen-film mammographic system. When a mammogram is performed, a beam of low energy x-ray photons is directed towards a compressed breast. This beam is filtered to remove low energy photons and collimated to the area of interest. The intensity of the beam exiting the breast is related to the thickness and type of tissue in the breast. The x-ray photons leaving the breast have to pass through an anti-scatter grid before reaching a phosphorous intensifying screen. If an x-ray photon is absorbed in the screen, light photons are emitted by the phosphor and these light photons expose a film which is processed to produce a mammogram. The exposure to the breast is stopped once an automatic exposure control, positioned under a section of the breast, has received a set exposure. Several books explain the mammographic process in detail [79], [80], [83] and appendix B contains details of the x-ray attenuating processes dominant in the mammographic energy range.

In this chapter we develop a mathematical model of the analogue mammographic process. As the model is developed, a number of factors which might degrade the mammogram become evident. These factors include: scattered radiation, beam hardening (in consequence of a polyenergetic source), and sometimes poor exposure due to the automatic exposure control being inappropriately located. A number of additional factors make it difficult to analyse mammograms quantitatively. These include vary-

ing processing results when developing films (which might also be called a degrading factor), system geometry, the "anode heel effect", and the response of the system components to x-ray photons of different energy. It is these factors which are the motivation for the model-based image enhancement algorithms proposed in chapters 4 and 5.

Substantial modeling of the mammographic process has taken place previously. This previous work has been inspired by the need to keep the radiation dose to the breast as low as possible, whilst giving an optimal signal-to-noise ratio [54], [60], [72], [90], [98], [109]. Because of the orientation of such work, the modeling has been used to optimise the radiographic equipment involved in mammography. Notably, this has included choice of anode material and x-ray tube voltage.

The model developed in this chapter is similar to those referenced. However, in the related work the authors usually predict the appearance of a mammogram performed on a standard breast and then optimize some contrast measure with respect to radiation dose to the breast; our model works backwards from the mammogram itself to find some measure of the object being imaged. This means that we are able to ignore radiation dose to the breast, but have to take account of the potential degrading factors mentioned above, as well as variations in breast size and composition, rather than assuming idealized imaging conditions and a standard breast.

The mathematical model proposed in this chapter is developed by following the path of the x-ray photons from production to exposure to the film. The assumptions which are necessary for the work on compensating for the spatially varying incident radiation intensity in chapter 4 are set out, as is the reason why this compensation allows pencil beam geometry to be assumed. After the polyenergetic incident radiation has been discussed, a breast model based on the x-ray attenuation properties of breast tissue is proposed. The next step is discussion of the anti-scatter grid and film-screen combination. We detail performance of an exposure of a lucite step wedge which determines the characteristic curve of the combination and therefore calibrates the system. The last part of the chapter derives the equations which enable quantitative measures of the breast tissue to be found. The equations involve both the breast exposure and breast thickness, which were both noted down specifically for us by the radiographers. The derived equations need an estimate of the most significant degrading factor, scattered radiation, and this is studied in chapter 5 where the equations are used with remarkable success on real mammographic images. The attainment of quantitative measures of the breast tissue indicates that the imaging parameters have been removed.

The mammograms used in our work were obtained from a G.E. Senographe 600 TS, with inherent filtration of 0.8mm Be and additional filtration of 0.03mm Mo. The film, screen, and processing equipment were Fuji, but the values used in our work are for the Kodak Ortho-M film and Min-R screen (which has the same phosphor and

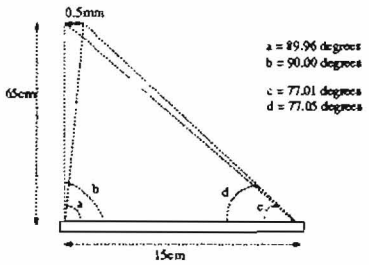

Figure 3.1: A two-dimensional representation of the geometry. Photons from opposite ends of the focal spot hitting the same place on the intensifying screen pass through nearly identical tissue. The focal spot size and horizontal distance are worst-case scenarios.

phosphor thickness as the Fuji screen) due to the lack of data for the Fuji equipment. The anti-scatter grid is a Phillips focused moving grid with paper interspacing.

3.2 Geometry

The x-rays form a divergent beam from the source whose focal spot and anode are situated above the chest wall of the woman currently being examined. The distance from the focal spot to the film is 65cm, and although the specified focal spot size is 0.3mm by 0.3mm the effective focal spot size can be nearer 0.5mm by 0.5mm. The size of the focal spot is a major contributor to overall image blur. This is because a finite focal spot allows x-rays to traverse the same tissue and yet strike the intensifying screen in a different place. This effect is reduced in objects lying nearer the screen, and this is one of the reasons for breast compression.

Using simple geometry it can be shown that two photons coming from opposite ends of the focal spot and passing straight through the breast before striking the intensifying screen at the same point will have traversed nearly identical tissue (figure 3.1). Similarly, the path length of the photons through the tissue can be calculated as a function of the angle at which they exit the focal spot (figure 3.2). The small focal spot size and large distance from source to breast, mean that a model of the source as an infinitesimal spot is reasonable.

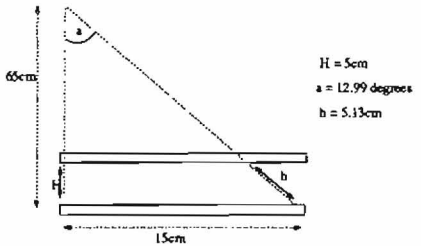

Figure 3.2: A two-dimensional representation of the geometry. Photons from different parts of the focal spot pass through different thicknesses of tissue dependent upon their direction of travel towards the film-screen combination. The focal spot size and horizontal distance are worst-case scenarios.

Despite the length of the path which the photons have to travel varying over the film, the volume of the cone of tissue V irradiated by the diverging beam to expose a fixed area A_p of the film is identical no matter where the area is positioned on the film:

$$V = \int_{65-H}^{65} A(h)dh,$$

where H is the breast thickness in cm and $A(h)$ is the cross-sectional area of the cone at distance h cm from the source. Since $A(h)$ is known to be A_p at a distance of 65 cm, it is known for all h:

$$A(h) = \left(\frac{h}{65}\right)^2 A_p$$

With this, the volume of tissue irradiated can be calculated:

$$\begin{aligned} V &= \int_{65-H}^{65} \left(\frac{h}{65}\right)^2 A_p dh \\ &= \frac{A_p}{3}\left(65 - \frac{(65-H)^3}{65^2}\right) \end{aligned} \tag{3.1}$$

One of the sub-goals of our modeling is to derive some quantitative measure of the composition of each cone of breast tissue. The measure which we choose is the average thickness of each tissue type which must have been present along each x-ray path from source to film to give the observed attenuation. To calculate these thicknesses, Beer's law for pencil beam geometry is to be applied. However, despite the volume of each tissue cone being constant, the beam used in mammography diverges and this needs

to be accounted for. Usually, the intensity of the diverging beam is assumed to be directly proportional to the inverse of the square of the distance from the source. In our modeling, the intensity decay due to the diverging beam is taken into account when we compensate for the spatially varying incident radiation intensity due to the "anode heel effect" (see next section). After the mammogram has been compensated, it appears as it would with a constant incident radiation intensity. We then have a situation where the incident and exiting intensities of the x-ray beam are known for a cone of breast tissue of volume V. The x-ray photons exposing any small area of the film have all traveled approximately equal path lengths through the breast. Application of Beer's law with the known intensities and path length provides an average attenuation as for the case of a non-diverging finite area beam. However, potential error exists in trying to determine the actual volume of each type of breast tissue from the attenuation because it is impossible to determine where the attenuating materials lie with respect to each other, and with respect to the irradiated tissue cone: a smaller volume of tissue at a place nearer the source can provide the same attenuation as a larger volume nearer the film.

3.3 Incident radiation

The incident radiation beam is polyenergetic and has strong characteristic radiation contributions at 17.4keV and 19.6keV from the Molybdenum anode. The beam is filtered by 0.8mm of Beryllium, from the tube window, and 0.03mm of Molybdenum. The incident spectrum used is as suggested by David Dance (personal communication), citing a program by Birch and Marshall, for a tube voltage of 28kVp (the standard tube voltage used for mammography in the UK). In our model, it is assumed that figure (3.3) represents the number of incident photons at each energy relative to the maximum (i.e. the number at 17.4 keV) *anywhere* across the x-ray field.

The energy of the photons is important because lower energy photons are more readily attenuated both in the breast tissue and the various components of the mammographic system. Furthermore, the difference between the attenuation coefficients of the breast tissues rises with lower energy. These facts mean that there is a trade-off between contrast in the mammogram and radiation dose to the breast: low energy photon beams give more contrast, but the breast receives a higher radiation dose. This trade-off is crucial in modeling which aims to optimise radiographic techniques, but can be ignored in our modeling because radiation dose to the breast is irrelevant.

The differential absorption of low energy photons can cause a loss of relative contrast in dense breast areas through "beam hardening". This is the effect whereby the average energy of the beam rises as the beam is attenuated. As well as loss of contrast, beam

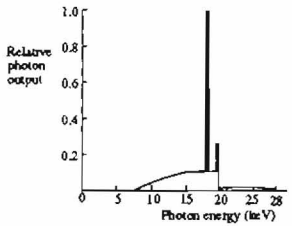

Figure 3.3: The x-ray spectrum of the beam used in the model for a tube voltage of 28kVp with a molybdenum anode. The beam is filtered by 0.8mm of Beryllium, from the tube window, and 0.03mm of Molybdenum.

hardening can also cause the automatic exposure control to terminate the exposure early. Both of these effects will be examined fully in due course.

The total number of incident photons is directly proportional to the tube current (fixed at 100mA) and time of exposure, which is given by an mAs (milli-Ampere seconds) value when the mammogram is performed. The incident exposure in mAs can vary between 30mAs and 500mAs depending on how large and dense the breast is; the actual value is determined by the automatic exposure control.

The incident spectrum is assumed uniform across the x-ray field, and so the number of photons incident on any part of the breast (N_0^{real}) is simply the integral of the number of photons over all energies, and is directly proportional to the mAs figure (X_c):

$$N_0^{real} = \int_0^{28} N_0^{real}(E)dE = \phi' X_c, \tag{3.2}$$

where ϕ' is some constant which will shortly be divided by another constant to form ϕ. There is no area term in equation (3.2) because pencil beam geometry is assumed.

The number of incident photons at any particular energy level, $N_0^{rel}(E)$, relative to the peak number of incident photons (which occurs at 17.4keV) is assumed constant, irrespective of the mAs value:

$$N_0^{rel}(E) = \frac{N_0^{real}(E)}{N_0^{real}(17.4)} \tag{3.3}$$

Rearranging (3.3) and substituting into (3.2):

$$N_0^{real} = \int_0^{28} N_0^{rel}(E)\, N_0^{real}(17.4)\, dE$$

$$= N_0^{rel}(17.4) \int_0^{28} N_0^{rel}(E)\, dE$$
$$= \phi' X_e$$

Let:

$$\phi = \frac{\phi'}{\int_0^{28} N_0^{rel}(E) dE}$$

Then

$$N_0^{rel}(17.4) = \phi X_e \tag{3.4}$$

This equation is used later to calculate the expected energy imparted to the intensifying screen. It is important because it illustrates the relationship between the mAs exposure value X_e and the peak number of photons.

The angle at which the anode of the x-ray tube is placed defines the spatial variations in the incident intensity due to the anode heel effect. The anode heel effect causes the intensity of the incident radiation to decrease away from the chest wall. The x-ray intensity also varies due to the diverging nature of the beam, although this effect is small given that the distance from the source to the intensifying screen is large relative to the radiation field size. The spatial intensity variation can be seen by exposing a film with no object present, with the mammography machine set to an mAs exposure of 4mAs (equivalent to a time of 0.04 seconds since the tube current is set at 100mA). The apparently blank film which is produced can be examined with a densitometer, and a graph showing the spatial variations of the incident radiation can be obtained by converting the densities back into energy imparted to the intensifying screen (figure 3.4). Since we have assumed that the incident radiation spectrum is uniform across the x-ray field, the anode heel effect is assumed to be due to the spatial variation of the number of photons. We assume that the ratio of number of incident photons between any two points remains constant no matter what the mAs value is. Chapter 4 shows how a digitized mammogram can be corrected for the spatial variations using the apparently blank film.

3.4 X-ray attenuation properties of breast tissue

The normal breast consists of fibrous, glandular and adipose tissue, and sometimes calcium. Adipose tissue is fibrous connective tissue packed with fat cells. There have been only two papers dealing with the attenuation of x-rays by the different types of breast tissue, and they reach different conclusions about the consistency of each type.

In order to estimate the absorbed radiation dose to the breast, Hammerstein et al. [42] determined the elemental compositions and densities of fat, adipose tissue, skin and glandular tissue. They found that skin and fat yielded consistent results, but that

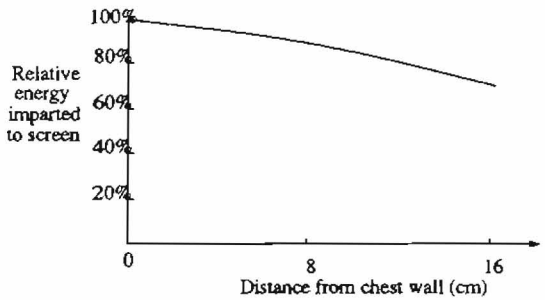

Figure 3.4: The combined effect of the anode heel effect and diverging beam on the incident radiation intensity. The graph was found by performing an exposure with no object present and calculating the energy which must have been imparted to the intensifying screen to give the measured film density.

the carbon and oxygen components varied greatly in adipose and glandular tissue. They ascribe this variation to difficulty in removing fibrous stroma from the adipose tissue, and from removing fatty material from the glandular tissue. Johns and Yaffe [56] do not report such difficulties, and include neoplastic tissue in their study. It seems likely that the consistency of the results of Johns and Yaffe stems from their looking at the components of adipose tissue separately (fatty tissue and fibrous tissue). Table (3.1) gives the linear attenuation coefficients reported by Johns and Yaffe.

For our purposes it suffices to refer to fibrous, glandular and cancerous tissue (which have similar linear attenuation coefficients) as "interesting tissue", as distinct from fat which has a much lower linear attenuation coefficient. We assume that skin and blood can also be classified as interesting tissue from the point of view of x-ray attenuation. This grouping of different tissue types is adequate for our purposes since we are interested in image enhancement rather than tissue classification.

Using figures from [88], the linear attenuation coefficient for calcium at 18keV is 26.1, at 20keV it is 19.28, and at 25keV it is 10.8. These relatively large values indicate the high attenuation of calcium, but since calcium occurs only in small quantities, the total attenuation is often more comparable to that of the other breast tissues. In our model, it is assumed either that calcium is not present or that it can be detected prior to further processing (a number of authors have claimed high detection rates [17],

Tissue type	No. patients		μ (cm^{-1}) at energy (keV)		
			18	20	25
Fat	7	Minimum	0.538	0.441	0.314
		Mean	0.558	0.456	0.322
		Maximum	0.585	0.476	0.333
Fibrous (Glandular) (Parenchymal)	8	Minimum	1.014	0.791	0.499
		Mean	1.028	0.802	0.506
		Maximum	1.045	0.816	0.516
Infiltrating duct carcinoma	6	Minimum	1.061	0.826	0.519
		Mean	1.085	0.844	0.529
		Maximum	1.137	0.884	0.552

Table 3.1: The linear attenuation coefficients for various breast tissue types reported by Johns and Yaffe [56]

[22]). With this assumption the remaining breast tissues can be classified according to their linear attenuation coefficients into interesting tissue or fat. This assumption is necessary to reduce the number of unknowns in the system and to allow correction for beam hardening. However, due to the importance of calcium in diagnosis, careful analysis of our proposed model-based image enhancement techniques takes place to ensure that the visibility of calcium is not diminished (such analysis is in section 5.3.7).

The linear attenuation coefficients of Johns and Yaffe cover the energy range from 18keV upwards (their work was directed towards dual energy imaging), but the mammographic energy range starts at 10keV. The linear attenuation coefficients for the rest of the range need to extrapolated.

In the mammographic energy range, the photoelectric absorption component (μ_τ) of the linear attenuation coefficient (μ) varies with the cube of the photon energy, whilst the scatter component (μ_σ) is near constant:

$$\mu(E) \approx \frac{\lambda}{E^3} + \mu_\sigma, \tag{3.5}$$

where λ is a constant related to the atomic numbers and densities of the materials being considered. Using this equation and the values in the table above, the linear attenuation coefficients for the different tissues can be extrapolated to cover the entire mammographic energy range. The result of this is shown in figure (3.5).

Using the linear attenuation coefficients, the number of primary photons (N_p^{real}) at energy E after the incident beam has passed through h_{int} centimetres of interesting

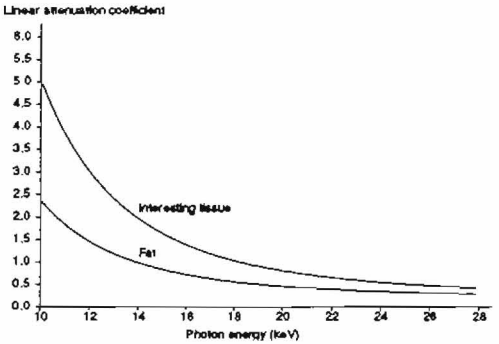

Figure 3.5: Values of the linear attenuation coefficients used for fat and interesting tissue. These are the averages of the values reported by Johns and Yaffe [56], with suitable extrapolation to cover the entire mammographic energy range.

tissue and h_{fat} centimetres of fat can be determined by applying Beer's law:

$$N_p^{real}(E) = N_0^{real}(E)e^{-(h_{int}\mu_{int}(E)+h_{fat}\mu_{fat}(E))}, \tag{3.6}$$

where (N_0^{real}) is the number of incident photons and $\mu_{int}(E)$ and $\mu_{fat}(E)$ are the linear attenuation coefficients of interesting tissue and fat respectively.

This leads to an equation giving the total number of photons in the primary beam:

$$N_p^{real} = \int_0^{28} N_p^{real}(E)dE = \int_0^{28} N_0^{real}(E)e^{-(h_{int}\mu_{int}(E)+h_{fat}\mu_{fat}(E))}dE \tag{3.7}$$

When a mammogram is performed, the breast is firmly compressed in order to produce better images. The word compression, taken in an engineering sense, is misleading as the the breast tissues do not compress but deform and displace with no loss of volume [85]. This is important because no change of volume implies no change in density and thus the linear attenuation coefficients of the tissues remain constant.

Let the distance between the compression plates be H cm and let h_{int} be the thickness of interesting tissue on any x-ray path and h_{fat} be the thickness of fat on the same path:

$$H = h_{int} + h_{fat} \tag{3.8}$$

Equation (3.7) can be rewritten to include this relationship and reduce the number of tissue unknowns to just one, namely h_{int}:

$$N_p^{real} = \int_0^{28} N_p^{real}(E)dE = \int_0^{28} N_0^{real}(E)e^{-(h_{int}\mu_{int}(E)+H\mu_{fat}(E)-h_{int}\mu_{fat}(E))}dE \tag{3.9}$$

The top compression plate is sometimes at an angle to the bottom compression plate rather than being parallel, but this is easily measured and corrected for. Equation (3.8) is incorrect at the breast edge with the film where the total thickness of tissue is reduced. Later in this thesis we model the breast edge as consisting of pure fat (section 5.5.1) and use detection of the reduced thickness as a verification test of the model (section 5.4).

To obtain quantitative measures of the breast tissues, all the x-ray attenuating factors in the system have to be considered. In addition to the breast, the major attenuators are the anti-scatter grid, intensifying screen and compression plate. To measure the attenuation it is necessary to consider energy imparted to the intensifying screen rather than the number of photons. After considering each of the system components, it will be shown how the attenuation expected with h_{int} cm of interesting tissue and h_{fat} cm of fat can be calculated.

3.5 Anti-scatter grid

Photons exiting from the breast have to pass through an anti-scatter grid before reaching the intensifying screen and film. Scatter was not recognised as a problem in mammography until around 1978, when Barnes and Brezovich [4] measured the number of scattered and primary photons reaching a NaI(Tl) crystal detector having passed through a circular lucite phantom 14cm in diameter. They varied the thickness of the lucite and the diameter of the circular radiation field (lucite is chosen because of its similar absorption and scattering properties to a breast consisting of half fat, half interesting tissue). The measurements were carried out without a grid and were taken beneath the centre of the lucite, figure (3.6) shows one of the results. As a consequence of the Barnes and Brezovich paper, anti-scatter grids were introduced into mammography with apparently dramatic effects [20],[21]. However, grids also remove some of the primary beam necessitating an increase in dose to the breast in order that the film is satisfactorily exposed. The increase in radiation dose to the breast is often double (the "Bucky factor"). Scatter reduction can be obtained with no increase in dose to the breast by introducing an air gap between the breast and film, but this introduces unacceptable blurring through magnification. Due to the increased exposure using a grid, their use is likely to remain an issue of debate, especially for women with small breasts. Carlsson et al. [11] report that in Sweden, where grids haven't been used in screening, experience has shown that their use would reduce the number of healthy women recalled to the assessment clinic. Modeling of the mammographic process and of the effects of scattered radiation could provide an alternative to using a grid, and hence could halve the radiation dose to the breast.

An anti-scatter grid is composed of a series of thin parallel lead strips separated by

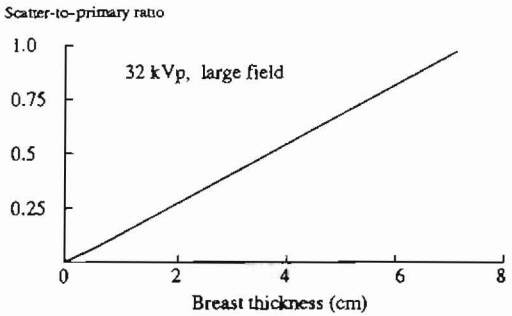

Figure 3.6: Variation of scatter to primary ratio with phantom thickness when no anti-scatter grid is used, according to Barnes and Brezovich [4]. As well as illustrating the high scatter component of the signal, this graph also shows the benefits of firm breast compression in reducing the scattered radiation component of the signal.

paper. The grid is oriented and focused so that photons emitted from the focal spot are mostly able to pass straight through. Grids can be moving or stationary. Moving grids are more expensive but are commonly used as they are less likely to produce grid lines in the mammograms. Figure (3.7) shows the relative transmission of the anti-scatter grid to primary photons at different energies, and figure (3.8) shows the relative transmission of scattered photons with direction, integrated over the azimuthal angle. Both graphs are as reported by Dance and Day [20].

Scatter-to-primary ratios calculated with and without an anti-scatter grid, as reported by Carlsson et al. [11], are shown in table (3.2). These ratios are averages over the breast shadow, and do not include extra-focal radiation. Carlsson et al. report that the scatter-to-primary ratio in the centre of the breast is around 15% higher than the average.

The anti-scatter grid is obviously effective in reducing the scatter component, but as we will show in chapter 5 it makes digital scatter removal more difficult by making the scatter component of a higher frequency through it becoming more reliant on the local tissue.

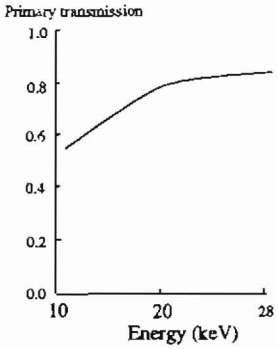

Figure 3.7: Relative transmission ratios through a moving anti-scatter grid of primary photons at different energies, according to Dance and Day [20].

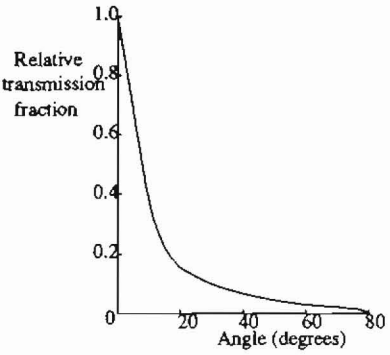

Figure 3.8: Relative transmission ratios through a moving anti-scatter grid of scattered photons at various angles, according to Dance and Day [20]. The values are relative to the transmission of primary photons with energies between 12.5 and 25 keV, and they have been integrated over the azimuthal angle.

Composition	Tissue thickness(cm)	S/P	S/P grid
Fat	2	0.2340	0.0376
	5	0.4832	0.0899
	8	0.7578	0.1469
50/50	2	0.2527	0.0425
	5	0.5412	0.1041
	8	0.8244	0.1630
Glandular	2	0.2695	0.0481
	5	0.6018	0.1173
	8	0.9070	0.1868

Table 3.2: Scatter-to-primary ratios calculated with and without an anti-scatter grid, and for different breast compositions, as reported by Carlsson et al. [11]. These ratios are averages over the breast shadow, and do not include extra-focal radiation.

3.6 Film and intensifying screen

X-ray photons passing through the breast and anti-scatter grid also have to pass through the film before being absorbed by an intensifying screen which produces visible light. It is this light that exposes the film and creates the image, although a small percentage of the x-ray photons are absorbed as they pass through the film. We assume that the exposure to the film is directly proportional to the energy imparted to the intensifying screen. The greater the exposure to the film, the darker it becomes and this darkness is usually measured in terms of film density, D:

$$D = \log_{10}\left(\frac{I_i}{T_i}\right), \tag{3.10}$$

where I_i is the intensity of the illuminating light (usually from a light box) and T_i is the intensity of the light transmitted through the film.

There are three primary sources of noise in film/screen mammography: film granularity, the limited number of x-ray quanta, and random inhomogeneities in the intensifying screen. At low and high film densities, and for spatial frequencies greater than 5 cycles/mm, film granularity is the dominate source. For medium film densities at spatial frequencies less than 5 cycles/mm quantum noise dominates. The noise in film-screen mammograms has been studied extensively elsewhere [3], [5], [58] and is not studied in this thesis.

An intensifying screen is used in mammography because it acts as a signal amplifier. Although use of an intensifying screen dramatically reduces x-ray dose to the breast, it also increases image unsharpness. The intensifying screen increases unsharpness

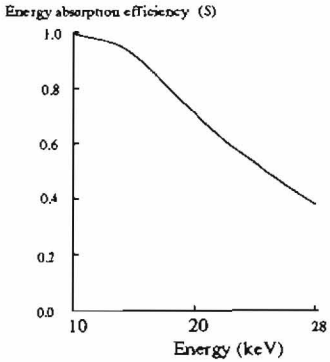

Figure 3.9: Relative absorption of primary photons by the intensifying screen, as reported by Dance and Day [20].

because when the x-ray photons are absorbed in the phosphor, light photons are emitted isotropically. The greatest exposure to the film is near where the x-ray photon was absorbed, but the overall effect is a blur rather than a precise point. The degree of this blur depends upon the energy of the x-ray photons in a non-trivial manner. This effect is termed glare. We have not tried to model this phenomenon due to the complexity of estimating the degree of blur and the lack of empirical data. Figure (3.9) gives the relative absorption of the different energy photons by the intensifying screen, as reported by Dance and Day [20].

The film-screen response to energy imparted to the intensifying screen is given by a characteristic curve (figure 3.10). The characteristic curve changes with the film processing conditions and must therefore be checked regularly if quantitative measures are required. Ideally, the energy imparted to the intensifying screen would be measured and simply plotted against film density. However, determining the energy imparted to the intensifying screen accurately is difficult. We approximate the characteristic curve by using a lucite step wedge and simulating the attenuation of the x-ray beam by the different thicknesses of lucite (this is explained in detail in appendix E). A small correction for scattered radiation is made, and the logarithm of the calculated relative energy imparted is plotted against film density, which is measured with a densitometer. We performed an exposure of the step wedge before every mammogram used in this thesis. It is assumed that the film-screen characteristic curve remains the same over a short period of time (i.e. the period between developing the step wedge and mammogram), and between cassettes. Exposing the step wedge with randomly

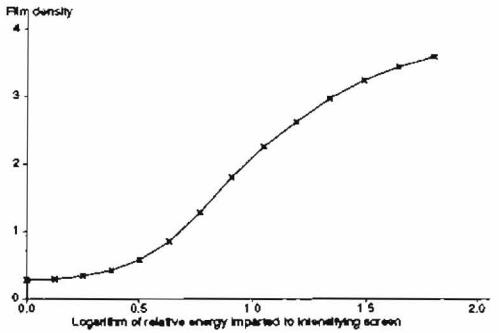

Figure 3.10: Film-screen characteristic curve found by exposing a lucite step wedge, measuring the film densities with a densitometer and plotting them against the results of a simulation to determine the relative energy imparted to the intensifying screen.

chosen film-screen cassettes on different days has not shown any great change in the characteristic curve.

The minimum film density is in the range 0.15 - 0.17 (called the base-fog), and the characteristic curve is approximately linear between film densities of 0.6 and 3.0. The automatic exposure control aims to keep most of the film densities between 1.0 and 2.2. The linear approximation is adequate for exploring the system characteristics, but a more realistic approximation is needed for quantitative work. In this thesis, the linear approximation is used to derive analytical expressions, whilst a piecewise linear approximation is used to find the relative energy imparted for any film density.

Let D be the film density for some area of the film, and let E^{real} be the energy imparted to the screen in this area and E^{real}_{ref} be the energy used as a reference. Define E^{rel} to be the energy imparted relative to the reference:

$$E^{rel} = \frac{E^{real}}{E^{real}_{ref}} \tag{3.11}$$

With the linear assumption in the region of interest the following equation can be written with γ the film/screen gradient, and β the other linear constant:

$$\begin{aligned} D &= \gamma \log_{10} E^{rel} + \beta' \\ \beta' &= \gamma \log_{10} \beta \\ D &= \gamma \log_{10}(\beta E^{rel}) \end{aligned} \tag{3.12}$$

The gradient γ is found from the characteristic curve and is taken to be the value which

best fits the data. Typically this has a value of just over 3.0 and is independent of the imparted energy being used as a reference. The value of β is related to speed. The higher that β is, the lower the imparted energy required to produce a certain film density and the faster the film. The value of β is difficult to find, principally because it changes significantly over time due to reciprocal law failure but also because it is dependent on the energy used as a reference.

The reciprocity law states that the density produced on a film depends only on the total amount of light energy employed. This law has been found to fail in mammographic film (when a screen is used), with greater exposures needed to produce the same film density as the time of exposure rises. Stanton [98] quotes Haus' assertion that to create the same film density Kodak Ortho-M film needs an increase in exposure (as measured in mAs) of 7%, 17% and 36% as the time of exposure is increased from 0.5 seconds to 1s, 2s and 4s respectively. Kimme-Smith et al. [60] found that reciprocal law failure occurred to similar degrees in all modern film-screen combinations, including Fuji. Arnold [2] concluded that the main consequence of reciprocal law failure is on the speed of the film, thus we assume that γ does not change due to it.

The choice of reference energy is important because it has to be a value which can be used not only to write other imparted screen energies in, but also later to write expected imparted energy knowing only the exposure in mAs. The characteristic curve in figure (3.10) is drawn relative to the energy imparted to the screen after the x-ray photons have passed through the greatest thickness of lucite in the step-wedge. In this thesis it is most convenient to work in terms of energy imparted relative to the energy imparted when an exposure of X_{ref} mAs is taken with no breast present ($E^{real}_{X_{ref}}$). This reference energy is found by taking an exposure at 4 mAs and measuring the largest density on the film, $D_{X_{ref}}$. This will be where the film has been exposed most (i.e. where most energy has been imparted to the screen) and will be beneath the anode. The tube current is set at 100mA and thus the time of exposure is 0.04 seconds. Using the values for reciprocal law failure given above, the mAs exposure value of 4mAs is corrected to be more consistent for the time of exposure of each specific mammogram, and this is the value X_{ref}.

The actual energy imparted to the intensifying screen E^{real} can be written relative to $E^{real}_{X_{ref}}$. Write equation (3.12) to be relative to $E^{real}_{X_{ref}}$:

$$D = \gamma \log_{10}\left(\beta \frac{E^{real}}{E^{real}_{X_{ref}}}\right) \tag{3.13}$$

When $E^{real} = E^{real}_{X_{ref}}$, $D = D_{X_{ref}}$ thus:

$$\beta = 10^{D_{X_{ref}}/\gamma} \tag{3.14}$$

Rearranging (3.13) and substituting in (3.14):

$$\begin{aligned} E^{real} &= \frac{1}{\beta} 10^{D/\gamma} E^{real}_{X_{ref}} \\ &= 10^{(D-D_{X_{ref}})/\gamma} E^{real}_{X_{ref}} \end{aligned} \tag{3.15}$$

3.7 Automatic exposure control (AEC)

The automatic exposure control (AEC) measures the amount of radiation reaching the film under a certain portion of the breast. It is meant to be positioned under the densest part of the breast to ensure good exposure in the area most likely to contain a carcinoma. The AEC on the G.E. Senographe is a half-cylinder with a radius of 3.5cm. The automatic exposure control can give poor results due to limitations in x-ray detection, beam hardening, reciprocal law failure and poor positioning [33].

The position of the densest breast tissue within the breast varies, and it is extremely difficult to determine before exposure. Consequently, the AEC is occasionally in the wrong position to ensure good overall exposure. The AEC is set to give a mean film density of around 1.5 in the film area directly above it. This is in the so-called useful range of film densities from 0.25 to 2.0 above base-fog (this is the range seen directly by a human viewing a mammogram on a light box).

Some measure of breast thickness tracking has to be built into the AEC in order that an adjustment for beam hardening can be made; otherwise, the high energy photons which make it through the thicker/denser breasts can cause early termination of the exposure. The setting of the AEC can be adjusted to suit individual radiologists. In the next chapter a model of an ideal AEC is proposed, and is used to decrease/increase the exposure theoretically to create mammograms which are similar to those produced in practice.

3.8 Calculation of quantitative breast values

3.8.1 Introduction

In this section, the aim is to derive equations to find quantitative values for the breast tissues. These values can be found by comparing the actual x-ray attenuation, derivable from the film densities and calibration data, to the theoretical x-ray attenuation calculated by using the linear attenuation coefficients of the various breast tissues. The

attenuation measure $\overline{h\mu}$ is defined as follows:

$$\overline{h\mu} = \ln\left(\frac{\text{Energy imparted to screen if no breast present}}{\text{Energy imparted to screen from primary radiation}}\right) \tag{3.16}$$

In this equation, scattered radiation is not considered, so that in the practical situation some correction for scatter is necessary, whilst in the theoretical situation only the primary contribution to the energy imparted is considered.

3.8.2 Calculating the energy imparted to the screen if no breast present

The energy imparted to the screen in the reference situation (X_{ref} mAs) is given by:

$$E^{real}_{X_{ref}} = \int_0^{28} N_0^{real}(E)\; E\; S(E)\; G(E)\; e^{-\mu_{lucE}(E)h_{plate}}\, dE, \tag{3.17}$$

where $N_0^{real}(E)$ is the number of incident photons with energy E, $S(E)$ is the absorption ratio of the screen to primary photons of energy E (figure 3.9) and $G(E)$ is the transmission ratio of the grid for primary photons of energy E (figure 3.7). The final factor gives the absorption of the primary photons by the compression plate. The plate is made of lucite (linear attenuation coefficient μ_{luc}, see appendix E) and is h_{plate} cms thick. For our system $h_{plate} = 0.4$cm. The effect of air is considered negligible.

The number of incident photons is related to the mAs exposure value which can be seen by substituting equations (3.3) and (3.4) into equation (3.17):

$$\begin{aligned} E^{real}_{X_{ref}} &= N_0^{real}(17.4)\int_0^{28} N_0^{rel}(E)\; E\; S(E)\; G(E)\; e^{-\mu_{lucE}(E)h_{plate}}\, dE \\ &= \phi X_{ref}\int_0^{28} N_0^{rel}(E)\; E\; S(E)\; G(E)\; e^{-\mu_{lucE}(E)h_{plate}}\, dE, \end{aligned} \tag{3.18}$$

where X_{ref} is the mAs exposure value.

The energy expected to be imparted to the screen for an exposure of X_c mAs can be written similarly:

$$E^{real}_{X_c} = \phi X_c \int_0^{28} N_0^{rel}(E)\; E\; S(E)\; G(E)\; e^{-\mu_{lucE}(E)h_{plate}}\, dE \tag{3.19}$$

This allows a simple calculation of the *relative* expected imparted energy for an exposure of X_c mAs by dividing (3.19) by (3.18) and rearranging:

$$\begin{aligned} E^{real}_{X_c} &= \phi X_c \int_0^{28} N_0^{rel}(E)\; E\; S(E)\; G(E)\; e^{-\mu_{lucE}(E)h_{plate}}\, dE \\ &= \frac{X_c}{X_{ref}} E^{real}_{X_{ref}} \end{aligned} \tag{3.20}$$

3.8.3 Calculating the theoretical x-ray attenuation

The value of $\overline{h\mu}$ can be calculated for the theoretical situation in which there is a thickness of h_{int} cms of interesting tissue, and h_{fat} cms of fat. Only the primary component of the energy imparted is considered.

Let E_p^{real} be the energy imparted to the screen from the primary photons when a breast is present:

$$E_p^{real} = \phi X_c \int_0^{28} N_0^{rel}(E)\, E\, S(E)\, G(E)\, e^{-\mu_{lac}(E)h_{plate}}\, e^{-h\mu(E)} dE, \qquad (3.21)$$

where $h\mu$ is the combined linear attenuation factor:

$$h\mu(E) = h_{int}\mu_{int}(E) + h_{fat}\mu_{fat}(E)$$

Rearranging equation (3.8) and substituting in gives:

$$h\mu(E) = h_{int}\mu_{int}(E) + (H - h_{int})\mu_{fat}(E) \qquad (3.22)$$

The effective attenuation, $\overline{h\mu}$, is defined mathematically as:

$$\overline{h\mu} = \ln \frac{E_{X_c}^{real}}{E_p^{real}}$$

Substituting in equations (3.18,3.21) and cancelling:

$$\overline{h\mu} = \ln \frac{\int_0^{28} N_0^{rel}(E)\, E\, S(E)\, G(E)\, e^{-\mu_{lac}(E)h_{plate}}\, dE}{\int_0^{28} N_0^{rel}(E)\, E\, S(E)\, G(E)\, e^{-\mu_{lac}(E)h_{plate}}\, e^{-h\mu(E)}\, dE}$$

Substitute equation (3.22) into this:

$$\overline{h\mu} = \ln \frac{\int_0^{28} N_0^{rel}(E)\, E\, S(E)\, G(E)\, e^{-\mu_{lac}(E)h_{plate}}\, dE}{\int_0^{28} N_0^{rel}(E)\, E\, S(E)\, G(E)\, e^{-\mu_{lac}(E)h_{plate}}\, e^{-h_{int}\mu_{int}(E) - (H - h_{int})\mu_{fat}(E)}\, dE} \qquad (3.23)$$

If the value of $\overline{h\mu}$ is known then this equation has only one unknown, h_{int}. However, it is extremely difficult to evaluate this integral equation directly to find h_{int}. The problem is alleviated by trying all feasible values of h_{int} and numerically integrating. This leads to a series of look-up tables from the $\overline{h\mu}$ value to h_{int} for each different breast thickness H. Figure (3.11) shows the relationship between h_{int} and $\overline{h\mu}$ in a breast with compressed thickness (H) of 8 cm. The ability to calculate h_{int} allows correction for beam hardening, to produce an image which would have been obtained using a monoenergetic source. The effect of beam hardening on the total linear attenuation from one material with increasing thickness of material (h) is shown in figure (3.12); as the thickness rises the linear relationship is lost.

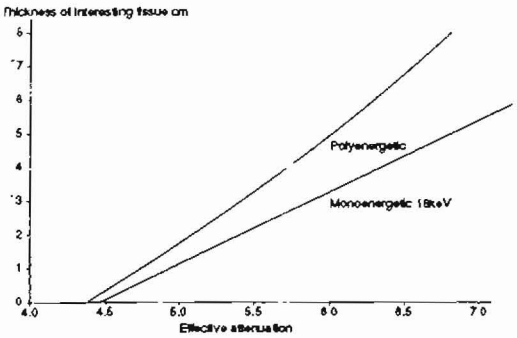

Figure 3.11: The relationship between effective attenuation coefficient $\overline{h\mu}$ and the thickness of interesting tissue h_{int} for a breast compressed to 8cm. Also shown is the attenuation if the beam had been monoenergetic with photon energy 18keV

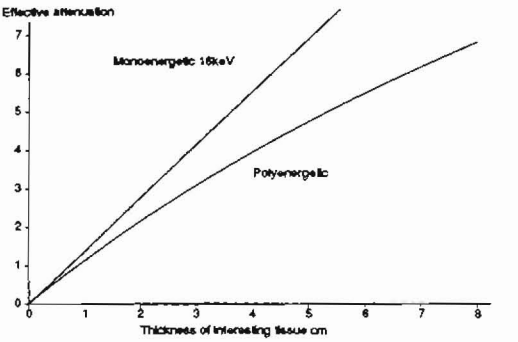

Figure 3.12: The effect of beam hardening on the attenuation properties of *just* interesting tissue with increasing thickness (h cm). Also shown is the attenuation with a 16keV monoenergetic beam.

3.8.4 Calculating the practical x-ray attenuation

The energy imparted to the screen E^{real} has a primary E_p^{real} and scattered component E_s^{real}:

$$E^{real} = E_p^{real} + E_s^{real} \tag{3.24}$$

Let

$$E_s^{rel} = \frac{E_s^{real}}{E_{X_{ref}}^{real}}$$

Rearrange (3.24) and substitute in (3.15):

$$\begin{aligned} E_p^{real} &= E^{real} - E_s^{real} \\ &= 10^{(D-Dx_{ref})/\gamma} E_{X_{ref}}^{real} - E_s^{rel} E_{X_{ref}}^{real} \\ &= (10^{(D-Dx_{ref})/\gamma} - E_s^{rel}) E_{X_{ref}}^{real} \end{aligned}$$

This equation is combined with equation (3.20) to find $\overline{h\mu}$:

$$\begin{aligned} \overline{h\mu} &= \ln\left(\frac{E_{X_c}^{real}}{E_p^{real}}\right) \\ &= \ln\left(\frac{X_c}{X_{ref}(10^{(D-Dx_{ref})/\gamma} - E_s^{rel})}\right) \end{aligned} \tag{3.25}$$

This equation is important because it means $\overline{h\mu}$ can be found practically without knowing the value of $E_{X_{ref}}^{real}$. Given an accurate knowledge of the scatter component (which we provide in chapter 5), the value of $\overline{h\mu}$ matches with a theoretical attenuation from the previous section to give a thickness of interesting tissue h_{int}.

3.9 Summary of chapter

In this chapter a model of the analogue mammographic process has been constructed which is the basic building block for later chapters. The first part of the modeling gave the assumptions which are vital in compensating an image for the spatially varying incident radiation intensity (which is explained in section 4.6):

- Assume that the relative incident radiation spectrum is spatially uniform across the x-ray field.
- Assume that the anode heel effect is due to the spatial variation of the number of photons (this must be the case if the incident radiation spectrum is uniform).
- Assume that the ratio of the number of incident photons between any two points remains constant no matter what the mAs value is.

- Assume that the total number of photons is directly proportional to the exposure value X_c mAs.

Once the image has been compensated for the spatially varying incident radiation intensity, the problem can be modeled with pencil, rather than diverging, beam geometry, and it becomes pertinent to deal with thicknesses of tissue:

- The compressed breast is of thickness H cm, and consists of fat and interesting tissue:

$$H = h_{int} + h_{fat},$$

where h_{int} is the thickness of interesting tissue and h_{fat} is the thickness of the fatty tissue.

- The theoretical attenuation of the beam, $\overline{\mu h}$ by h_{int} centimetres of interesting tissue and $H - h_{int}$ centimetres of fat can be calculated:

$$\overline{h\mu} = \ln \frac{\int_0^{28} N_0^{rel}(E)\, E\, S(E)\, G(E)\, e^{-\mu_{luc}(E) h_{plate}}\, dE}{\int_0^{28} N_0^{rel}(E)\, E\, S(E)\, G(E)\, e^{-\mu_{luc}(E) h_{plate}}\, e^{-h_{int}\mu_{int}(E) - (H - h_{int})\mu_{fat}(E)}\, dE}$$

where E is the photon energy, $N_0(E)$ is the relative number of incident photons at energy E, $S(E)$ is the relative screen absorption, $G(E)$ the relative grid transmission of primary photons, h_{plate} the lucite compression plate thickness, and μ_{fat}, μ_{int} and μ_{luc} are the respective linear attenuation coefficients.

The attenuation found in practice along an x-ray path can be calculated:

- The film density D can be written in terms of the illuminating light intensity I_l and intensity of the light transmitted through the film T_l, and also, for a limited range of D, in terms of the relative energy imparted to the intensifying screen:

$$\begin{aligned} D &= \log_{10} \frac{I_l}{T_l} \\ &= \gamma \log_{10} \beta E, \end{aligned}$$

where β and γ are calculated from calibration data.

- The practical attenuation is found from the film density and mAs exposure value X_c:

$$\overline{h\mu} = \ln \left(\frac{X_c}{X_{ref}(10^{(D - D_{X_{ref}})/\gamma} - E_s)} \right),$$

where X_{ref} comes from the calibration data, and is corrected for film reciprocal law failure, $D_{X_{ref}}$ comes from the calibration data, and E_s is a scatter estimate.

Comparison of the found practical attenuation with the calculated theoretical attenuation gives a quantitative measure of the breast tissue, h_{tm}.

In terms of the overall aim of our modeling, this chapter has shown how to move from film density D to thickness of interesting tissue h_{tm} given the exposure X_r mAs, a scatter estimate F_s, and calibration data obtained from a lucite step wedge. Chapter 4 explains how film density is measured in a mammogram, and chapter 5 provides the scatter estimate as well as producing enhanced images using the values of h_{tm}.

4

Fundamentals of Mammographic Image Processing

4.1 Introduction

This chapter transfers the analogue model developed in chapter 3 to the digital domain, and explains the fundamentals of model-based mammographic imaging processing: digitization, display, simulation of the automatic exposure control and correcting for the spatially varying incident radiation intensity.

Transferring the analogue model to the digital domain simply requires the addition of spatial variables, and the recognition that any non-specific areas become the area of one pixel as determined by the digitization. Thus, rather than discuss the energy imparted to a non-specific area A of the intensifying screen, the discussion becomes centred around the energy imparted to a fixed area corresponding to a pixel with specific spatial coordinates.

The digitizing and displaying of the mammographic images are crucial to the success of any model-based image processing. The digitizing is crucial because quantitative values of the object being imaged are required, and it is therefore necessary to remove the digitizing parameters. The display is crucial because it is pointless performing carefully planned enhancement if an unknown transform is to be applied before the image is viewed.

Simulating the automatic exposure control and correcting for the spatially varying

incident radiation are fundamental to the more advanced model-based work described in chapter 5. Correcting for the spatially varying incident radiation intensity allows pencil beam geometry to be used, and later algorithms to be performed as convolutions. The automatic exposure control model proposed in this chapter provides the mechanism whereby images can be created which look similar to real mammograms. Notably, the automatic exposure control model allows appropriate amplification of the primary signal which is found by the scatter removal algorithms described in chapter 5.

The chapter starts with an explanation of how mammograms are digitized, and how the images are displayed to keep the same brightness relationships as in the original mammogram. This is followed by examples of mammographic images transformed into images which represent the energy imparted to the intensifying screen. The model of the analogue mammography process is then used to simulate the changes in the mammographic images which occur when the mAs exposure is altered, or when the automatic exposure control setting or position is adjusted. The theory behind compensating for the spatially varying incident radiation intensity is then set out, and the chapter concludes with a flow chart and discussion of the various relationships between not only the digital transforms but also the analogue process and digital process.

4.2 Digitization

Mammography is not as yet digital, although it promises to become so within the near future. The reason that it has not yet become digital is the concern that the quality of the digital images is not yet good enough to satisfactorily image the smallest mammographic abnormalities. However, Karssemeijer et al. [58] claim that diagnosing from a mammogram digitized to 2000 by 2000 pixels is already as good as diagnosing directly from the films themselves since it appears that the loss of resolution can be compensated for by increased contrast. Parkin et al. [77] report that their directly digital mammography system, although suffering from noise and the difficulty of getting left and right mammographic images into positions where asymmetry can be checked for, does allow improved performance in dense breasts.

A mammogram can be digitized by a variety of instruments, but when quantitative measures of the imaged object are desired the imaging parameters must be known. Initially, we used a CCD camera but these images were abandoned because the relationship between pixel value and film density was hard to determine, apparently due to a hidden gain control within the camera (appendix D). Instead, a Joyce-Loeblescanning microdensitometer was used (by kind permission of the Royal Marsden Hospital,

London). This produces an extremely high resolution (4200 x 3072), 8-bit grey-scale image, where the pixel value is linearly related to the film density (rather than the light transmitted through the film which is picked up by a CCD camera):

$$D(x,y) = \frac{P(x,y) - 273.2}{-91.07}$$

The mammographic images in this thesis are of a smaller size (700 x 512). The smaller images were derived from the larger ones using a median filter. The median filter was chosen because of its structure preserving properties.

Recording film density rather than the intensity of the light transmitted through the film is preferable because the film density is independent of the illuminating light intensity level. Calculation of film density can be made robust to spatial variations in the illuminating light intensity by measuring the illuminating light intensity at the same time as the transmitted light intensity, rather than measuring it once and assuming that it remains constant.

The Joyce-Loeble scanning microdensitometer scans the entire mammogram with a 50 micron beam calculating diffused, rather than specular, film density. Diffused film density is calculated using the integral of the intensity of the light being transmitted through the film over all angles, whereas specular film density uses the integral of the intensity of the light over a much smaller, more direct, range of angles. Diffused film density is the correct choice for our work, because not only is it the measure calculated by most densitometers, but also the computer screen is a diffuse device: each pixel spreads light in all directions.

The Joyce-Loeble scanning microdensitometer is a highly accurate piece of equipment. However, it can only measure film densities within the range 0.2 to 3, and any film densities greater than 3 are set to 3. Fujl mammographic film contains information over the film density range 0.2 to 3.7, so that the breast edge of the digital images is slightly curtailed. This does not appear to be a serious problem as the nipple area is easily identifiable on most of the digitized mammograms (figure 5.27); although it is part of the reason that some of the breast images look to have a rough, rather than smooth, outline.

Of the film density range stored on the mammograms, only the film densities between 0.2 and 2.2 can be seen on a standard light box (without the use of a "hot" light). This implies that in both the film and digital mammographic image there is information that the viewer does not normally perceive.

The Joyce-Loeble scanning microdensitometer has a fixed film density to pixel value transform. Unfortunately, although this allows a simple pixel value to film density transform, it also introduces excess quantization error when the mammogram does not contain film densities spanning the entire 0.2 to 3 film density range. This is especially

true of cranio-caudal view mammograms where few films have densities lower than 0.8 within the breast area. In this situation, the pixel values corresponding to film densities from 0.2 (pixel value 255) to 0.8 (pixel value 200) are not being used.

As well as quantization error, any digitizing equipment also introduces additional noise and blur into the system. Caldwell and Yaffe [10] restored their mammographic images in order to compensate for resolution degradation due not only to the digitizing aperture, but also the finite size of the focal spot and glare in the intensifying screen. They did this by applying, in the frequency domain, an inverse filter based on the modulation transfer function.

4.3 Displaying mammographic images

When a film is on a light box, the eye receives the light transmitted through the film (T_l):

$$T_l = I_l 10^{-D}, \tag{4.1}$$

where I_l is the intensity of the illuminating light and D is the film density. The digital images photographed for this thesis have the luminance of each pixel set to be directly proportional to the light transmitted through the film in the corresponding area. This means that if an area on the film is twice as bright as another area (i.e. has twice the light being transmitted through the film), then that area in the digitally displayed image is also twice as bright (i.e. has twice the luminance).

For the particular terminal screen on which the work in this thesis was carried out, the luminance L from each pixel (x, y) was directly proportional to the square of the pixel value P:

$$L(x, y) = \alpha P^2(x, y), \tag{4.2}$$

where α is the constant of proportionality. The luminance L is required to be directly proportional to the intensity of the light transmitted through the film in the area corresponding to (x, y):

$$L(x, y) = \lambda T_l(x, y), \tag{4.3}$$

for some λ. To obtain this relationship:

$$P(x, y) = \left(\frac{\lambda}{\alpha}\right)^{1/2} T_l^{1/2}(x, y) \tag{4.4}$$

Substituting in the film density equation (4.1), and assuming I_l to be constant:

$$P(x, y) = \left(\frac{\lambda I_l}{\alpha}\right)^{1/2} 10^{-D(x,y)/2} \tag{4.5}$$

The dynamic range of the terminal screen (i.e. the ratio of highest luminance to lowest luminance) is around 40, for the screen in question. This corresponds to being able to perceive luminance at around a pixel value of 40 and still being able to see increasing luminance up to a pixel value of 255. This dynamic range is well below that of a film on a light box, which is approximately 100 (taking film densities of 0.2 and 2.2 as being the extremes seen). Consequently, to display the images and have the required relationship between luminance and "transmitted light", the transmitted light range has to be reduced. Fortunately, the lowest film density is rarely below 0.6, especially on cranio-caudal view mammograms, and using this as the minimum density reduces the dynamic range required to just under 40. Setting a film density of 0.6 to give a pixel value of 255 provides the constant in equation (4.5):

$$\begin{aligned}\left(\frac{\lambda I_t}{\alpha}\right)^{1/2} &= P(x,y)/10^{-D(x,y)/2} \\ &= 255/0.501 \\ &= 508.8 \end{aligned} \tag{4.6}$$

Figure (4.1) shows mammographic images transformed from the original to an image corrected for the terminal screen (i.e. to make luminance directly proportional to pixel value), and then into a "transmitted light" image calculated from equation (4.5) with the constant set to 508.8.

4.4 Energy imparted to the intensifying screen

The first stage in model-based image processing is to remove the imaging parameters in order to obtain quantitative measures of the imaged object. In the case of mammography this process has several steps, some of which require extensive modeling. In this section the digitizing parameters and film-screen parameters are removed. Removal of the digitizing parameters is simple since there is a fixed transform between pixel value and film density. Removal of the film-screen parameters requires calibration of the system as described in chapter 3. The calibration provides the characteristic curve and this allows transformation of the film densities into values representing the relative energy imparted to the intensifying screen. Using the linear approximation to the characteristic curve, the transformation is as in equation (3.12):

$$E(x,y) = \frac{1}{\beta} 10^{D(x,y)/\gamma}$$

Figure (4.1) shows "energy imparted" images, the value of γ is 3.2, and the value of β is 5.6. In both cases, the energy imparted images are displayed with luminance directly proportional to the energy imparted.

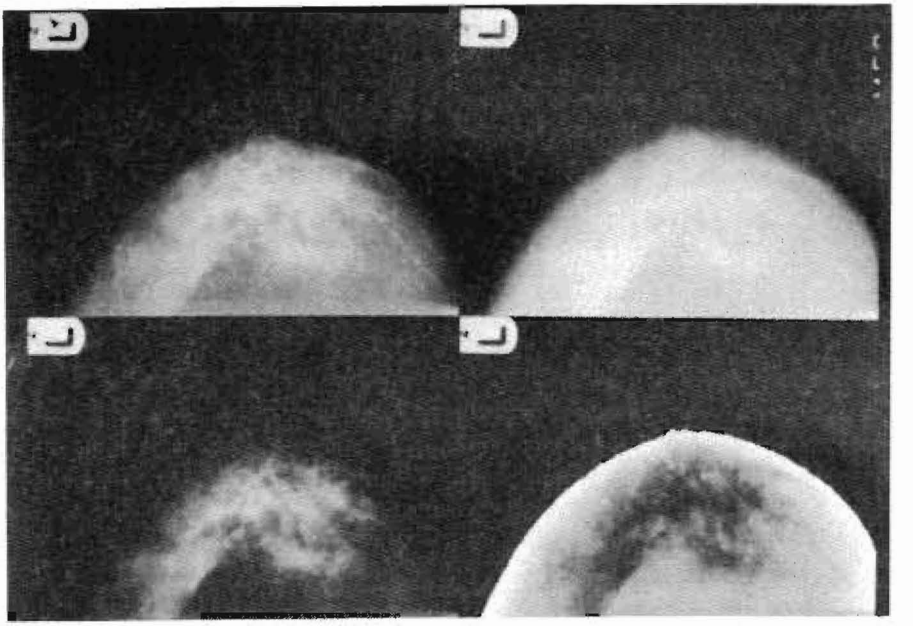

Figure 4.1: Images of breast MML1 (top) and FDL1 (bottom). The top left image is the original from the digitizer, the top right image is the original transformed to make luminance directly proportional to pixel value. The bottom left image is the image which would be seen if the mammogram were put on a light box: $P(x,y) = 508.8\ 10^{-D(x,y)/2}$, where D is the film density. The bottom right image has luminance directly proportional to energy imparted to the intensifying screen.

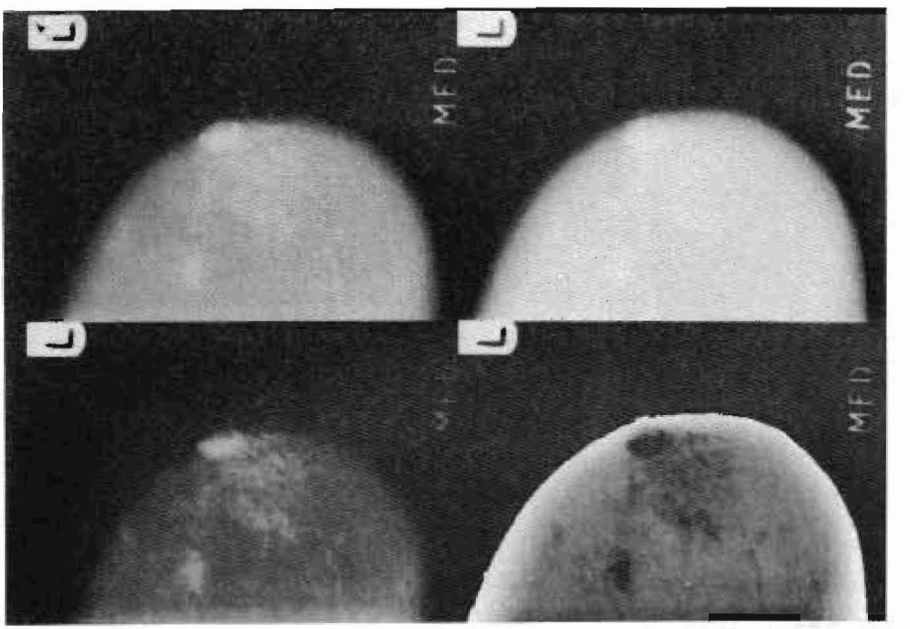

4.5 Simulating different exposures

4.5.1 Introduction

As explained during the development of the analogue model, the automatic exposure control is meant to control the amount of radiation reaching the film under a dense area of the breast, and to terminate the exposure when a certain average film density has been reached in the area. There are two major potential problems in this apparently simple task. The first is that the AEC might be poorly positioned so that it is under a fatty area of the breast when in fact there is a dense area present. The second problem is that beam hardening can cause the average photon energy to be unexpectedly high. Consequently, breast thickness tracking has to be built into the AEC in order that it can adjust. If tracking is not provided then beam hardening can make the AEC cause early termination of the exposure. In this section we explain two ways of increasing/decreasing the exposure and show how to simulate the corresponding changes in the mammographic images.

4.5.2 Adjusting the mAs exposure value manually

To correct a mammographic image for under- or over-exposure, it can be changed to simulate manipulation of the mAs exposure value. Let X_c mAs be the exposure at which the original mammogram was performed, and let X_c' mAs be the new exposure value. The energy imparted to the intensifying screen has both primary and scattered components:

$$E(x,y) = E_p(x,y) + E_s(x,y) \tag{4.7}$$

Recall equation (3.21) which gives the energy imparted to the intensifying screen due to primary photons, and insert spatial coordinates:

$$E_p(x,y) = \phi X_c \int_0^{28} N_0^{rel}(E)\, E\, S(E)\, G(E)\, e^{-\mu_{tissue}(E) h_{tissue}}\, e^{-h_\mu(x,y;E)} dE$$

Replace the part not dependent on X_c by $E_p^{nd}(x,y)$:

$$E_p(x,y) = X_c E_p^{nd}(x,y) \tag{4.8}$$

If there are N incident photons and N_s of these are scattered to reach a point on the image, then it can be estimated that $2N_s$ scattered photons will reach the image when there are $2N$ incident photons. It is reasonable therefore to assume that the scattered component is also directly proportional to the mAs exposure value:

$$E_s(x,y) = X_c E_s^{nd}(x,y), \tag{4.9}$$

where $E_s^{unf}(x,y)$ is not dependent on the exposure. Substitute equations (4.8) and (4.9) into equation (4.7):

$$E(x,y) = X_c(E_p^{unf}(x,y) + E_s^{unf}(x,y))$$

The energy imparted at (x,y) with the new exposure can be written similarly:

$$\begin{aligned} E'(x,y) &= X_c'(E_p^{unf}(x,y) + E_s^{unf}(x,y)) \\ &= \frac{X_c'}{X_c} E(x,y) \end{aligned} \tag{4.10}$$

Figure (4.2) shows an original mammographic image performed with an exposure of 106.0 mAs, and figure (4.3) shows the result of simulating an increase in exposure to 121.0 mAs. The transformed image was created by calculating the new energy imparted values E' and re-applying the relationship depicted in the characteristic curve to find the film density.

4.5.3 Theoretical automatic exposure control

Instead of manually adjusting the exposure, the action of an automatic exposure control unit can be modeled. We model the action of the AEC as aiming to produce an average film density in an certain area. This simple model of the AEC is not affected by beam hardening because it works on the values within the film itself.

Let $\overline{E}_{AEC}$ be the average energy imparted to the screen in an area $\mathcal{A}$, directly above the automatic exposure control, with n the total number of pixels in $\mathcal{A}$, and E the energy imparted corresponding to the pixel (x,y):

$$\overline{E}_{AEC} = \frac{1}{n} \sum_{(x,y)\in\mathcal{A}} E(x,y) \tag{4.11}$$

Let $\overline{E}'_{AEC}$ be the average energy imparted required, and let $E'(x,y)$ be the energy imparted at each pixel which obtains this average. The automatic exposure control setting might equally be set by specifying an average film density, this value giving $\overline{E}'_{AEC}$ when converted to energy imparted.

In the new image, $\overline{E}'_{AEC}$ is the average of the new energies imparted in the area $\mathcal{A}$:

$$\overline{E}'_{AEC} = \frac{1}{n} \sum_{(x,y)\in\mathcal{A}} E'(x,y) \tag{4.12}$$

Divide this equation by equation (4.11):

$$\sum_{(x,y)\in\mathcal{A}} E'(x,y) = \frac{\overline{E}'_{AEC}}{\overline{E}_{AEC}} \sum_{(x,y)\in\mathcal{A}} E(x,y) \tag{4.13}$$

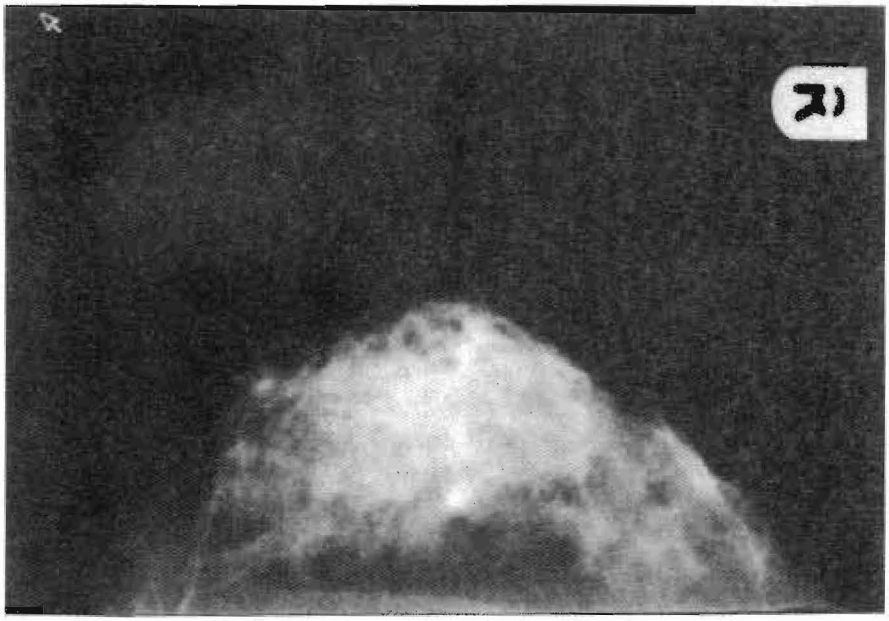

Figure 4.2: The original mammographic image MMR1. The densest tissue is forward of the automatic exposure control and consequently the image looks underexposed.

Figure 4.3: This image has the automatic exposure control positioned at the back wall (the usual place), and the exposure is set to 121 mAs rather than 106 mAs, which was the original exposure.

From equation (4.10) it is known that increases/decreases in overall exposure have a multiplicative, rather than additive effect on each individual energy imparted. Thus the following relationship must hold for some λ:

$$E'(x,y) = \lambda E(x,y) \tag{4.14}$$

If $\lambda > 1.0$ then the exposure is increased, if $\lambda < 1.0$ then the exposure is decreased. Combining equation (4.13) with (4.14):

$$\lambda = \frac{\overline{E'}_{AEC}}{\overline{E}_{AEC}} \tag{4.15}$$

The image given in chapter 1, figure (1.11), has the "control set" to give an average film density of 1.8, this results in an almost identical image to figure (4.3). More information is visible in the dense central areas, but information disappears in the darker areas (effectively through over-exposure).

As well as adjusting the setting of the automatic exposure control, it is also possible to adjust the position it is in. The automatic exposure control unit can be fixed into any one of three positions underneath the breast, figure (4.4) shows the positions. To model a change in AEC position is a just a simple process of changing the position of area $\mathcal{A}$. Figure (4.5) shows the effect on the original mammographic image depicted in figure (4.2) of moving the automatic exposure control forward towards the nipple.

4.5.4 Analysing the image changes analytically

The effect of increasing/decreasing the exposure can be partly analysed by examining the affect on the individual transmitted light values. Combining equations (4.1) and (3.12) gives:

$$T'_l(x,y) = \frac{I_l}{(\beta E'(x,y))^\gamma}, \tag{4.16}$$

where T'_l represents the transmitted light through the film after the increase/decrease in the exposure. Let λ be the multiplicative factor by which the imparted energies were changed:

$$E'(x,y) = \lambda E(x,y)$$

Substitute this into equation (4.16):

$$\begin{aligned} T'_l(x,y) &= \frac{I_l}{(\beta \lambda E(x,y))^\gamma} \\ &= \frac{I_l}{(\beta E(x,y))^\gamma \lambda^\gamma} \\ &= \frac{T_l(x,y)}{\lambda^\gamma} \end{aligned}$$

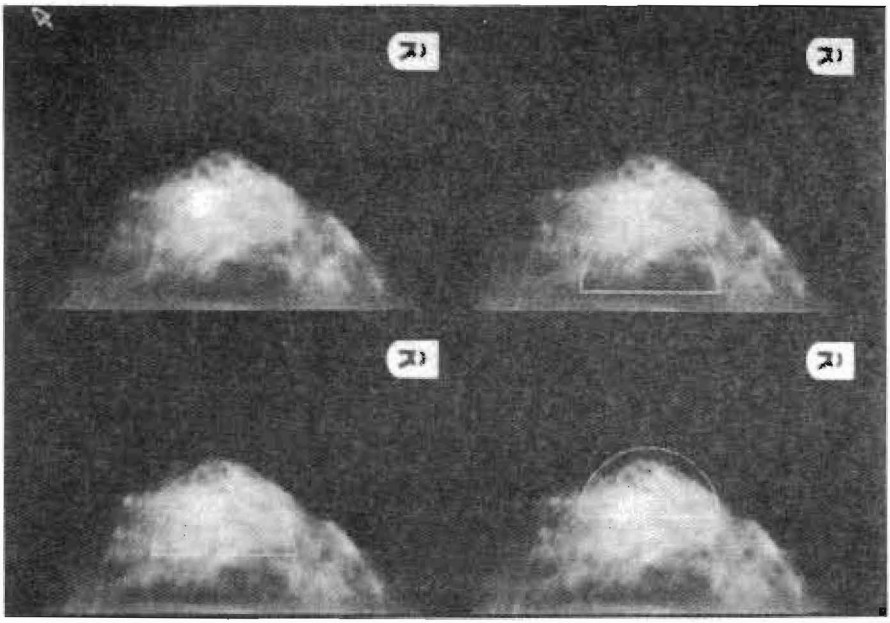

Figure 4.4: Original mammographic image, MMR1 with the automatic exposure control unit marked in all the different possible positions.

If $\lambda > 1.0$ then the exposure is being increased and the intensity of the light transmitted through the film falls; if $\lambda < 1.0$ then the exposure is being decreased and the intensity of the light transmitted through the film rises. Since $\gamma \approx 3$, doubling the exposure ($\lambda = 2$) reduces the transmitted light values by a factor of 8.

The effect of different exposures can also be viewed in terms of the range of transmitted light. Let $T_{l\,range}$ be the initial transmitted light range:

$$\begin{aligned} T_{l\,range} &= T_{l\max} - T_{l\min} \\ &= \frac{I_l}{(\beta E_{min})^\gamma} - \frac{I_l}{(\beta E_{max})^\gamma} \end{aligned}$$

Substituting in the new imparted energies gives the new transmitted light range:

$$\begin{aligned} T'_{l\,range} &= T'_{l\max} - T'_{l\min} \\ &= \frac{I_l}{(\beta E_{min})^\gamma \lambda^\gamma} - \frac{I_l}{(\beta E_{max})^\gamma \lambda^\gamma} \\ &= \frac{1}{\lambda^\gamma} T_{l\,range} \end{aligned}$$

Figure 4.5: Image MMR1 with the automatic exposure control positioned as far as it goes outwards to the nipple in practice, and set to give an average density of 1.5. The control unit is around 3cm further in than was used in the original mammogram. The original image is shown in figure 4.2

Taking the example above, doubling the exposure ($\lambda = 2$) reduces the range of transmitted light by a factor of 8.

The simulation of increasing/decreasing exposure described in this section not only idealizes the functioning of the automatic exposure control unit, but also the mammographic process: in practice, an increase in exposure would reduce the quantum noise, and a decrease in exposure would increase the quantum noise.

4.6 Correcting for spatially varying incident radiation intensity

The incident radiation intensity varies spatially because of the anode heel effect and diverging beam (figure 3.4). It is assumed that the variation is due to the number of incident photons varying across the image rather than the relative incident energy spectrum changing. The main variation is a smooth intensity reduction from the back of the film out towards the nipple, and this can be as great as 25% of the maximum value. The variation along the back of the film is much smaller. The spatial variation of the incident radiation intensity is usually accepted under the premise that the breast is less dense near the nipple and so the reduction in incident radiation intensity results in a mammogram with more equal film densities.

The variation of the incident radiation intensity can be measured by performing an exposure with no object present, and the mammography machine set to 4mAs (a very low exposure). The result of such an exposure is an apparently blank film with film densities (on our system) in the range 2.1 to 2.5.

The film density on a mammogram is created by an exposure due to scattered radiation, and an exposure due to primary radiation:

$$\begin{aligned} D(x,y) &= \gamma \log_{10} \beta E(x,y) \\ &= \gamma \log_{10} \beta + \gamma \log_{10}(E_p(x,y) + E_s(x,y)) \end{aligned} \tag{4.17}$$

It is known from equations (3.4) and (3.21) that $E_p(x,y)$ is related to $N^{real}_{0(17.4)}(x,y)$, the number of incident x-ray photons with energy 17.4 keV at position (x,y):

$$\begin{aligned} E_p(x,y) &= N^{real}_{0(17.4)}(x,y) \int_0^{28} N^{rel}_0(E)\, E\, S(E)\, G(E)\, e^{-\mu_{tar}(E) h_{plate}}\, e^{-h\mu(x,y,E)}\, dE \\ &= N^{real}_{0(17.4)}(x,y) E^{rel}_p(x,y), \end{aligned} \tag{4.18}$$

where $E^{rel}_p(x,y)$ is the part of the equation not dependent on $N^{real}_{0(17.4)}(x,y)$. Making the assumption that the scatter contribution is also directly proportional to the total number of photons, the scatter contribution can be written relative to $N^{real}_{0(17.4)}(x,y)$ for some $E^{rel}_s(x,y)$:

$$E_s(x,y) = N^{real}_{0(17.4)}(x,y) E^{rel}_s(x,y) \tag{4.19}$$

Substitute equations (4.18) and (4.19) into the film density equation (4.17):

$$D(x,y) = \gamma \log_{10} \beta + \gamma \log_{10}(N^{real}_{0(17.4)}(x,y) E^{rel}_p(x,y) + N^{real}_{0(17.4)}(x,y) E^{rel}_s(x,y))$$

This equation gives the film density on the original film; this is the film density with the spatially varying incident radiation intensity. It can be rewritten as:

$$D(x,y) = \gamma \log_{10} \beta N^{real}_{0(17.4)}(x,y) + \gamma \log_{10}(E^{rel}_p(x,y) + E^{rel}_s(x,y))$$

Let the film density required be that from an incident photon number of $N^{real}_{0(17.4)}$, where this is the maximum incident number of photons along any ray over the image; this will be beneath the anode. Call the required film density $D'(x,y)$:

$$D'(x,y) = \gamma \log_{10} \beta N^{real}_{0(17.4)} + \gamma \log_{10}(E^{ad}_p(x,y) + E^{ad}_s(x,y))$$

then

$$D'(x,y) = D(x,y) + \gamma \log_{10}\left(\frac{N^{real}_{0(17.4)}}{N^{real}_{0(17.4)}(x,y)}\right) \tag{4.20}$$

If a film is directly exposed to incident radiation, the spatially varying incident radiation intensity becomes evident. For such a directly exposed film the energy imparted is given by equation (3.17):

$$\begin{aligned} E_0(x,y) &= N^{real}_{B(17.4)}(x,y) \int_0^{28} N^{rel}_0(E)\, E\, S(E)\, G(E)\, e^{-\mu_{tot}(E) h_{plate}}\, dE \\ &= N^{real}_{B(17.4)}(x,y) E^{ad}_0, \end{aligned} \tag{4.21}$$

where $N^{real}_{B(17.4)}(x,y)$ is the number of photons arriving at the point (x,y), and E^{ad}_0 is the part of the equation not dependent on $N^{real}_{B(17.4)}(x,y)$. This imparted energy gives a film density on the apparently "blank" image of:

$$D_B(x,y) = \gamma \log_{10} \beta' N^{real}_{B(17.4)}(x,y) E^{ad}_0,$$

where γ is the same as for the actual mammogram, but β may have changed to β' (possibly due to film reciprocal law failure). At the point where $N^{real}_{0(17.4)}(x,y) = N^{real}_{0(17.4)}$ in the actual mammogram (i.e. beneath the anode), the density in the apparently blank image is:

$$D^A_B = \gamma \log_{10} \beta' N^{real}_{B(17.4)} E^{ad}_0$$

Subtracting,

$$D^A_B - D_B(x,y) = \gamma \log_{10}\left(\frac{N^{real}_{B(17.4)}}{N^{real}_{B(17.4)}(x,y)}\right) \tag{4.22}$$

It was assumed in the model that the ratio of number of incident photons between any two points remains constant no matter the mAs value, so that:

$$\frac{N^{real}_{0(17.4)}}{N^{real}_{0(17.4)}(x,y)} = \frac{N^{real}_{B(17.4)}}{N^{real}_{B(17.4)}(x,y)}$$

Thus, if the directly exposed image is registered with the mammographic image the film density which is required $D'(x,y)$ is given by substituting equation (4.22) into equation (4.20):

$$D'(x,y) = D(x,y) + (D^A_B - D_B(x,y)) \tag{4.23}$$

Figure (4.6) shows the effect of this transform on two mammographic images. As expected, the images are slightly darker towards the nipple than the originals.

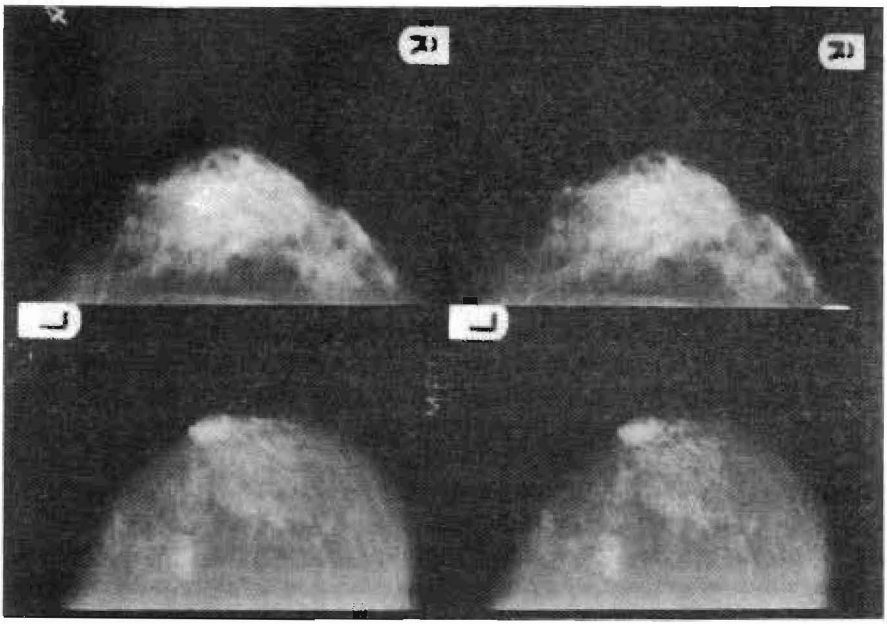

Figure 4.6: The images on the left are original mammographic images displayed as on a light box. The images on the right are the images transformed to be as if a spatially uniform incident radiation intensity was used. The images are darker towards the nipple.

4.7 Summary of chapter

In this chapter it has been explained how mammograms are digitized, and how mammographic images are displayed to preserve relative brightness. Furthermore, the algorithms and theory which we consider to be fundamental to model-based mammographic image processing have been explained. Figure (4.7) shows the relationships between the various images, and the analogue and digital domains.

In terms of the overall aim of our modeling, this chapter has filled in the early stages:

- The pixel values in the mammographic images can be converted to film densities, using a fixed linear relationship:

$$D(x,y) = \frac{P(x,y) - 273.2}{-91.07}$$

- The film densities can be corrected to the values which would have been recorded had the incident radiation intensity been spatially uniform:

$$D'(x,y) = D(x,y) + (D_B^A - D_B(x,y)),$$

where D_B^A is the maximum film density on an apparently blank film which has been exposed to the x-rays with no attenuation material in the way, and $D_B(x,y)$ is the film density on this apparently blank film at the position (x,y).

With the corrected film density and a scatter estimate (given in chapter 5) the equations in chapter 3 can be used to find the thickness of interesting tissue and a mammographic examination using a monoenergetic beam can be simulated (also in chapter 5). Alternatively, from the film density the relative energy imparted to the intensifying screen can be found and different exposures simulated:

- $E(x,y) = \frac{1}{\beta} 10^{(D(x,y)/\gamma)}$
- Change the mAs exposure value from X_c to X_c':

$$E'(x,y) = \frac{X_c'}{X_c} E(x,y)$$

Similarly, the automatic exposure control can be modeled to manipulate the image. The automatic exposure control model which was devised in this chapter is based on adjusting the imparted energies in a multiplicative way within a certain region of the image until the required average is found. It is this simple model which is used in chapter 5 to "terminate" the theoretical exposure once the image has become dark enough.

To display the new images, the imparted energies are transformed back into film densities which are then converted to pixel values using an equation designed to keep the same relationship between luminance on the terminal screen and transmitted light through the film:

- Convert energy imparted to film density:

$$D(x,y) = \gamma \log_{10}(\beta E(x,y))$$

- Convert film density to pixel value:

$$P(x,y) = 508.8\, 10^{-D(x,y)/2}$$

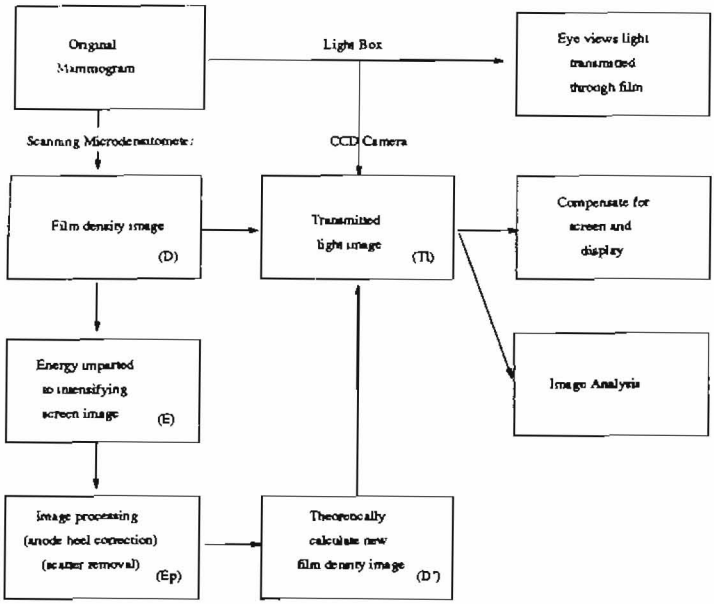

Figure 4.7: Flow chart of relationships between transforms explained in this chapter.

5

Modeling Scatter

5.1 Introduction

We consider scattered radiation to be the key degrading factor in mammographic images. We believe this because not only does scatter significantly degrade the image, but removal of the scatter component from the signal allows quantitative measures of the breast tissue to be found, and with these measures simulation of the mammographic process with a monoenergetic beam can take place. In this chapter we propose two models of scatter, and subsequently simulate a monoenergetic examination.

Scattered radiation degrades mammographic images through imparting a smoothly varying energy component to the intensifying screen. The scatter component carries no information about the breast tissue on the specific x-ray path from source to pixel, although as we show in the section (5.3.3) it does contain information about the breast tissue in the local area (in fact, our second scatter model uses the reverse of this finding to estimate the scatter component given some measure of the local tissue). The image degradation due to scattered radiation is usually considered in terms of either a contrast measure or "scatter degradation measure"; both of which are appropriate in simplistic cases, but not in real cases with complex imagery.

Few papers on the removal of the effects of scattered radiation from x-ray images have been published, and none specifically for mammographic images. One approach has been to consider the scatter component as a blurred version of the original and then to subtract it [71]. This is similar to the second model we propose in this chapter

except that we work on an image with the imaging parameters removed and not the original. Another approach is to consider the original as blurred, and to sharpen it by estimating the point spread function for scattered radiation and deconvolving [86]. The first approach is more appropriate with mammographic images because scattering is a contrast forming phenomena, as well as a contrast reducing phenomena.

There are two different contributors to what we term scattered radiation: the breast, and various components of the mammographic system. The amount of scatter reaching the intensifying screen within the breast shadow has been dealt with in several papers, but the scatter reaching the intensifying screen around the edge of the breast is much less well documented. At the breast edge a substantial scatter component is present (figure 5.16), despite the scatter from the breast tissue coming only from one side. The increased scatter component is apparently due to extra-focal radiation (the x-ray beam is collimated to the area of the film, not the area of the each specific breast), and breast edge effects. "Breast edge effects" refers to the curved nature of the breast edge which allows easier passage of scattered photons to the intensifying screen.

There have been a number of papers in the medical physics literature on scattered radiation in mammography, and these papers together with their results will be introduced as the scatter models are developed. These previous papers have mostly been written with a view to estimating the quantity of scatter, and to investigating the trade-off between the benefits of using an anti-scatter grid and increased radiation dose to the breast. Furthermore, none of these papers has been written with a view to digital removal of the effects of scatter. However, it is these papers which provide much of the evidence for the scatter models which we propose in this chapter.

The problem of scattered radiation in radiography is similar to problems which occur in remote sensing and other vision areas. In particular, techniques developed in lightness computation, such as homomorphic filtering, appear at first sight to be directly relevant since the scatter component is additive once the original image is transformed into an energy imparted image. Such filtering relies on determining, and being able to use, a property of the unwanted signal component which enables it to be distinguished from the wanted signal component. Typically, the unwanted signal is assumed to vary spatially smoothly, while the wanted signal has many sharp changes corresponding to localised structures such as calcifications. The blurred appearance of mammographic images suggests this is a reasonable assumption to make about the scatter (unwanted) and primary (wanted) components. We experimented with homomorphic filtering to remove the scatter component but gave up when it became apparent that the primary and scatter components have overlapping characteristics; which theoretically rules out use of the approach. For example, although the scatter component varies smoothly across the image, in places the primary component also varies smoothly.

Having failed to satisfactorily (let alone reliably) remove the effects of scattered radiation with conventional techniques, we returned to the ideology of this thesis and studied the physics of the system to develop two scatter models. The first model (the "constant scatter model") simply assumes that scatter is a uniform flood of radiation after the spatially varying incident radiation intensity has been compensated for. The second model (the "weighted scatter model") is less naive and is based on the (reasonable) conjecture that the scatter component $E_s(x_c, y_c)$ is related to the values of the energy imparted to the intensifying screen $E(x, y)$ for (x, y) in a neighbourhood $\mathcal{N}$ surrounding the pixel (x_c, y_c).

After developing the second model we verify the results by transforming the primary component $E_p(x_c, y_c)$ at each pixel into the thickness of interesting tissue which must have been present between the pixel and x-ray source (using the equations in chapter 3). Several tests have been performed on the "interesting tissue" images, and the results are extremely encouraging. On the basis of knowing the thickness of interesting tissue h_{int} for each pixel, the results of simulating the mammographic process with a *mono*energetic beam are shown with various photon energies. In this way any contrast loss due to beam hardening is corrected, and the energy of x-ray beam optimised for image quality, rather than for low radiation dose to the breast. The chapter concludes with the automation of the choice of photon energy.

5.2 Constant scatter model

The first scatter model which we propose is based on the observation that in many radiographic problems, scattered radiation can be considered as a uniform flood of radiation over the image surface. Assuming this is not as dumb as might be thought; in fact the assumption holds for small objects, but not for large objects such as breasts. This model is not offered as a serious model, but rather to illustrate what might be achieved if such a model were available.

In terms of the mammographic model proposed in chapter 3, the constant scatter observation translates to the scatter component of the energy imparted to the intensifying screen being constant across the image. To make the observation more realistic for mammography, we assume that the energy imparted to the screen due to scattered radiation is constant *after* the image has been corrected for the spatially varying incident radiation intensity. With this assumption, the effects of scattered radiation can be removed without knowing the absolute value of the constant.

After compensating the image for the spatially varying incident radiation intensity, the energy imparted to the intensifying screen in the area corresponding to pixel (x_c, y_c)

can be found by rearranging equation (3.12):

$$E(x_c, y_c) = \frac{1}{\beta} 10^{D(x_c, y_c)/\gamma} \tag{5.1}$$

This energy is assumed to be equal to a primary component (E_p), which varies from pixel-to-pixel and a scatter component (E_s) which is assumed constant across the image:

$$E(x_c, y_c) = E_p(x_c, y_c) + E_s$$

Let E_{min} be the minimum energy imparted to the breast image (after segmentation of the breast area from the film and, if appropriate, pectoral muscle). This energy corresponds to those pixels in the image with the minimum imparted energy due to primary photons, E_{pmin}, and the minimum film density, D_{min}:

$$\begin{aligned} E_{min} &= \frac{1}{\beta} 10^{D_{min}/\gamma} \\ &= E_{pmin} + E_s \end{aligned}$$

Since the scatter component E_s is assumed constant across the image, the difference between the primary component at pixel (x_c, y_c) and that at the minimum can be calculated:

$$\begin{aligned} E_p(x_c, y_c) &= E_p(x_c, y_c) - E_{pmin} \\ &= (E(x_c, y_c) - E_s) - (E_{min} - E_s) \\ &= E(x_c, y_c) - E_{min} \\ &= \frac{1}{\beta} 10^{D(x_c, y_c)/\gamma} - \frac{1}{\beta} 10^{D_{min}/\gamma} \\ &= \frac{1}{\beta} (10^{D(x_c, y_c)/\gamma} - 10^{D_{min}/\gamma}) \end{aligned}$$

The mammographic process is designed to show relative changes in imparted energy. It is therefore appropriate to transform E_p back to a film density as if it were re-exposing the film using equation (3.12):

$$D(x_c, y_c) = \gamma \log_{10} \beta E(x_c, y_c)$$

However, naive application of this process (substituting E_p for $E(x_c, y_c)$) yields logarithms of numbers less than one. To solve this problem an offset φ is added to E_p:

$$D(x_c, y_c) = \gamma \log_{10} \beta (E_p(x_c, y_c) + \varphi)$$

The offset is determined by calculation of the additional imparted energy needed to make $D(x_c, y_c)$ give the minimum film density displayable when $E_p(x_c, y_c) = 0$. The complete constant scatter algorithm is shown in table (5.1).

The need for an offset corresponds to the fact that if anti-scatter grids are improved in terms of their rejection of scatter then the radiation dose to the breast has to be increased in order to produce a viewable image on the film. This increase in radiation dose to the breast is a powerful argument for intelligent software removal of the effects of scattered radiation rather than the hardware solution provided by the grid.

Figure (5.2) shows the output from the constant scatter algorithm when presented with the original image shown in figure (5.1). Another example is shown in figure (5.4), with the original in figure (5.3). A further example was given in figures (1.1) and (1.6) in chapter 1.

The constant scatter algorithm clearly enhances the images and it is easy to see why it should. The transmitted light (T_l) coming through the film in the area corresponding to pixel (x_c, y_c) is related to film density:

$$T_l(x_c, y_c) = I_l 10^{-D(x_c, y_c)}$$

The film density $D(x_c, y_c)$ is in turn related logarithmically to $E(x_c, y_c)$:

$$D(x_c, y_c) = \gamma \log_{10}(\beta E(x_c, y_c))$$

Thus:

$$\begin{aligned} T_l(x_c, y_c) &= I_l 10^{-\gamma \log_{10}(\beta E(x_c, y_c))} \\ &= I_l(\beta E(x_c, y_c))^{-\gamma} \\ &= \frac{I_l \beta^{-\gamma}}{E(x_c, y_c)^{\gamma}} \end{aligned}$$

Given that $\gamma > 3.0$, it is evident that for the same absolute range of $E(x_c, y_c)$, the smaller the absolute values, the greater the range of T_l, and the greater the contrast. The constant scatter algorithm simply shifts the absolute values of imparted energy down to where the transmitted light range is maximised for the absolute energy range. It follows that the constant scatter algorithm will enhance any image whose minimum density is greater than the minimum displayable - in this study the minimum value is 0.6, although a film and lightbox can display densities down to 0.2. The transformation between input transmitted light and output transmitted light is shown in figure (5.5) for various D_{min}. In essence, the information in the output image is the same as it was before scatter removal, but the displaying of this information is being optimised.

The constant scatter algorithm algorithm is susceptible to noise in that an erroneous value of D_{min} (possibly from poor segmentation of the breast from the background) seriously limits the enhancement. It might therefore be better to make the algorithm more robust by, for example, setting D_{min} to the first value with a certain number of occurrences.

	Constant Scatter Algorithm
Assume	After the spatially varying incident radiation intensity has been compensated for, the scattered energy component imparted to the intensifying screen is constant across the image.
Input	Original mammogram $D(x,y)$, film/screen gradient γ, reference density D_{ref} and "blank" image $D_B(x,y)$.
(1)	Compensate for spatially varying incident radiation: $D'(x,y) = D(x,y) + (D_B^A - D_B(x,y))$ Where $D'(x,y)$ is the corrected film density, $D(x,y)$ is the original film density, D_B^A is the film density on the "blank" image beneath the anode and $D_B(x,y)$ is the film density on the "blank" image
(2)	Calculate β from the reference density this is also the density under the anode (D_B^A): $\beta = 10^{D_{ref}/\gamma}$
(3)	Find D'_{min} from the compensated mammographic image (after careful segmentation of the breast area from the image).
(4)	For each pixel calculate the assumed difference in imparted primary energy between the pixel and the pixel where D'_{min} is situated: $E_p(x,y) = E_p(x,y) - E_{p_{min}}$ $E_p(x,y) = \frac{1}{\beta}(10^{D'(x,y)/\gamma} - 10^{D'_{min}/\gamma})$
(5)	Calculate offset (φ), this is to ensure that the final image has a minimum film density of 0.6 (i.e. when $E_p = 0$): $\varphi = \frac{1}{\beta}10^{0.6/\gamma}$
(6)	Calculate new energy imparted : $E^{new}(x,y) = \varphi + E_p(x,y)$
(7)	Calculate new film density: $D^{new}(x,y) = \gamma \log_{10}(\beta E^{new}(x,y))$

Table 5.1: The "constant scatter algorithm"

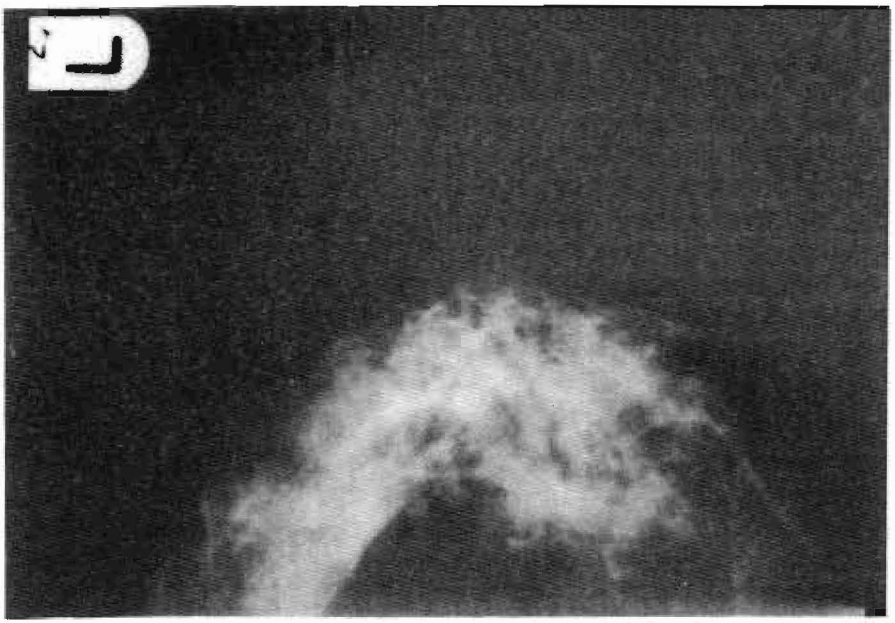

Figure 5.1: Original mammographic image MML1

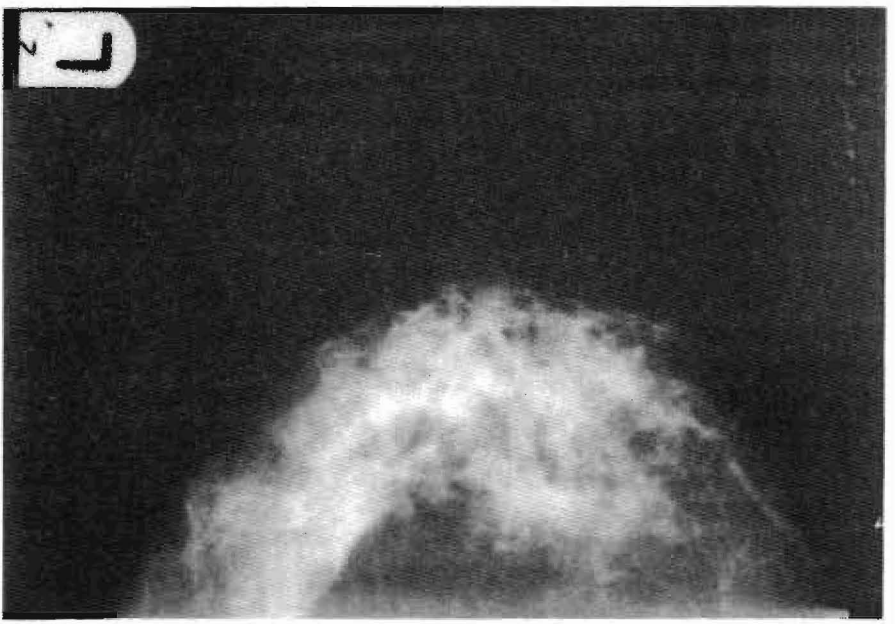

Figure 5.2: Result of the constant scatter algorithm for image MML1. The image has been corrected for the anode heel effect, had a constant scatter factor removed and has then been transformed back to an image recognisable by a radiologist.

Figure 5.3: Original mammographic image FDL1

Figure 5.4: Result of the constant scatter algorithm for image FDL1. The image has been corrected for the anode heel effect, had a constant scatter factor removed and has then been transformed back to an image recognisable by a radiologist.

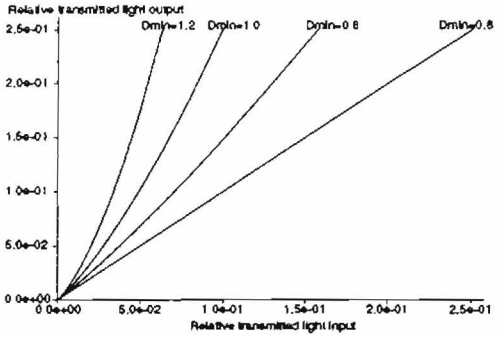

Figure 5.5: The transformation between input transmitted light and output transmitted light from the constant scatter algorithm. The transmitted light is given relative to I_I, so that a film density of 1.0 is plotted as $T_I = 10^{-1.0} = 0.1$. The algorithm sets a variable depending upon the value of the lowest film density D_{min} within the breast image, and these values are marked on the curves.

The constant scatter algorithm works by reducing the imparted energies to the intensifying screen by a constant. Reducing the overall exposure to the breast does not achieve similar results because changing the overall exposure has a multiplicative effect on imparted energy (as shown in equation 4.10) rather than an additive one. It should also be noted that quantum noise is inversely related to exposure; thus with this algorithm a large T_I range is obtained as for a smaller exposure whilst retaining the smaller noise effects of a larger exposure. Ignoring a constant energy term in practice increases photon noise as well as running into the problem of estimating how much of the signal must be ignored, not knowing the breast consistency to begin with.

There are other possibilities for mapping from E_p to film density. One such possibility is to find the range of E_p and interpolate this onto the range of energies which produce film densities in the visible range. However, such a scheme whilst certainly improving contrast in the bright areas might also reduce contrast in the dark areas, and would be in general unpredictable. A more sensible method would be to estimate the absolute scatter component, remove it, and then apply the AEC model from chapter 4, but since the constant scatter assumption is simplistic such an estimate should not be made.

5.3 Weighted scatter model

5.3.1 Introduction

The "weighted scatter model" is based upon the conjecture that the amount of scattered radiation $E_s(x_c, y_c)$ is related to the values of $E(x, y)$ for (x, y) in a neighbourhood $\mathcal{N}$ surrounding the pixel (x_c, y_c). The nature of this relationship is highly complex and is inevitably approximated. In effect, the values of $E(x, y)$ in a neighbourhood are used to estimate the composition of the local tissue, and from this composition the scatter component is estimated from published data. However, tissues nearer to the central pixel effect the scatter component more than those tissues further away, and so the values of $E(x, y)$ need to be weighted to reflect this.

The method of weighting is based upon defining a "scatter volume", which represents where the scattered photons reaching an area of the intensifying screen corresponding to a pixel actually come from. We derive a scatter volume from the empirical published data reported by Barnes and Brezovich [4] for a homogeneous lucite phantom with no anti-scatter grid. The formula of Dance and Day [19] for an anti-scatter grid is then used to estimate where the scattered photons reaching a pixel actually come from with a grid. From this, a weighting mask $w(x, y)$ is derived which represents for each pixel in a neighbourhood $\mathcal{N}$ of the central pixel what percentage of the total scattered radiation comes from the vertical column of lucite at that pixel.

The aim is to convolve the weighting mask w with the imparted energy image E to give an image U:

$$U(x_c, y_c) = \sum_{(x_c - x, y_c - y) \in \mathcal{N}} E(x_c - x, y_c - y) w(x, y) \tag{5.2}$$

The values in image U are input to a "scatter function" s which estimates the scatter component $E_s(x_c, y_c)$ at each pixel (x_c, y_c). The scatter function s is found using three example cases where the entire volume of breast tissue being irradiated is considered to be: 100% fat; 100% interesting tissue; 50/50 fat/interesting tissue by mass. For each of these cases an estimate of the energy imparted due to the primary component ($E_p(x, y)$) is made using the breast thickness (H) and exposure (X, mAs). The values of Carlsson et al. [11] for the scatter-to-primary ratio ($\frac{E_s}{E_p}$) in the three examples cases are then used to estimate the total energy imparted $E(x, y)$:

$$\begin{aligned} E(x, y) &= E_p(x, y) + E_s(x, y) && (5.3) \\ &= E_p(x, y) + \tfrac{E_s}{E_p} E_p(x, y) && (5.4) \\ &= E_p(x, y)(1 + \tfrac{E_s}{E_p}) && (5.5) \end{aligned}$$

Using $E(x, y)$, the value of U can be determined for the three example cases and the

relationship between U and E_s found, giving the scatter function s:

$$E_s(x_c, y_c) = s(U(x_c, y_c)) \tag{5.6}$$

Application of the weighting mask at the breast edge with the film has to take into consideration the effects of extra focal radiation and the breast edge shape, both of which are significant. To model these effects, the amount of scattered radiation at the breast edge is estimated from the values reported by Lam and Chan [63]. This enables the value to be used when the weighting mask falls on a pixel outside of the breast shadow, but on the film, to be found (E_{out}). If the weighting mask falls outside of the image altogether a value of zero is used. This reflects the fact that the radiation field is collimated to the area of the film.

The mammographic images in this thesis are cranio-caudal views of the breast, while those produced by screening programmes are usually of the medio-lateral view. Medio-lateral view mammograms show the pectoral muscle diagonally across the back of the image. This would not present a problem to the weighted scatter algorithm since the pectoral muscle is highly absorbing, and the amount of scattered radiation emanating from it and reaching the important part of the image (i.e. the breast area) is minimal and can be treated as zero.

Given the weighting mask, scatter function and edge effect value E_{out}, the primary component of the energy image can be found. This component cannot be used directly to re-expose the film theoretically because it is too small to create a decent image (the film would appear under-exposed). To get around this the automatic exposure control is modeled as in chapter 4, and this is used to increase the primary component to a large enough level to produce a perceivable final image.

The calculation and removal of scatter using the "weighted scatter model" is outlined in figure (5.6). The method described is a variant of a common way to enhance features and edges: subtracting a blurred version of the original from itself. The differences are that in our case the original has been transformed to an energy imparted image first, and all the variables have been derived from measured data. Thus, for example, there is no need to guess the degree of blurring required or a suitable mask size. There are of course approximations and simplifications in the work, and these are pointed out as the details of the algorithm are presented.

5.3.2 Defining scatter volume with no grid

The first step in the algorithm shown in figure (5.6) is to define where the scattered photons reaching an pixel (x_c, y_c) come from without an anti-scatter grid. No data has been published for this, but it is derivable for lucite (which approximates 50% fat and

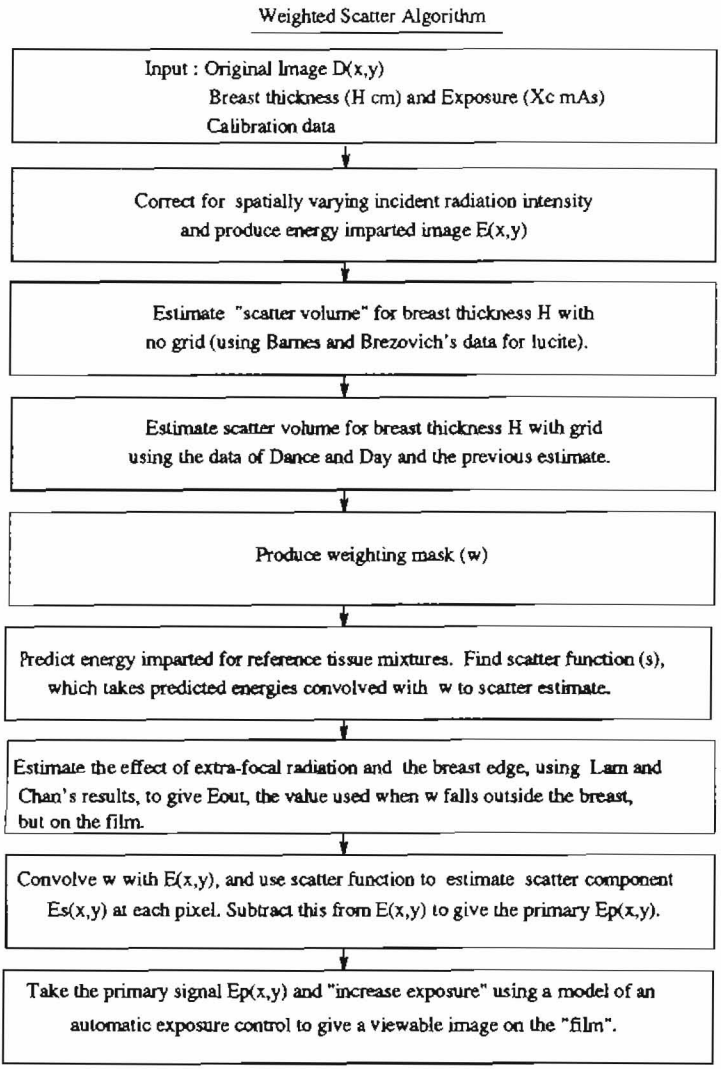

Figure 5.6: Outline of weighted scatter algorithm

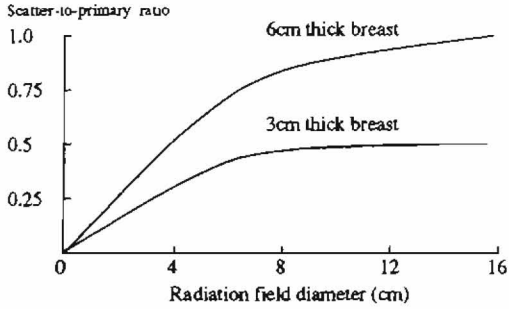

Figure 5.7: Variation of scatter to primary ratio with radiation field diameter when no anti-scatter grid is used, according to Barnes and Brezovich [4].

50% interesting tissue by mass) using the results published by Barnes and Brezovich [4].

Barnes and Brezovich measured the number of scattered and primary photons reaching a NaI(Tl) crystal detector having passed through a circular lucite phantom 14cm in diameter. They varied the thickness of the lucite and the diameter of the circular radiation field. The measurements were carried out without an anti-scatter grid and were taken beneath the centre of the lucite. Although the exact circumstances which they used are different from those in modern mammography, their results are appropriate because it is not the exact values of scatter-to-primary which are required, but the percentage of the total scatter coming from various distances.

Figure (5.7) gives the measured scatter-to-primary ratio for different diameters of the radiation field. The thickness of the phantom is fixed for each curve, thus the primary component is constant. That is, the rate of change of the curve gives the rate of change of the scatter component with increasing field size, and so it is possible to determine the percentage of the total scatter reaching the detector from various distances.

In order to accommodate any breast thickness, a linear relationship between the scatter-to-primary ratio and phantom thickness is assumed for any fixed field diameter. This allows us to interpolate, or extrapolate, to find the scatter-to-primary ratios for phantom thicknesses other than 3 or 6 cm. This assumption is in agreement with the linear relationship Barnes and Brezovich found between scatter-to-primary ratio and phantom thickness for a large radiation field diameter, figure (3.6).

Let $\frac{s}{p}(r)$ be the scatter-to-primary ratio for a phantom of thickness H, radiation field radius r, and let dr be a small increment in the radius. Let $E_s(r)$ be the total energy imparted to the detector due to scattered radiation from the lucite phantom when the radiation field has radius r, and let $E_p(r)$ be the primary component of the total energy. The amount of scattered radiation $dE_s(r)$ coming from the cylinder of lucite defined by the inner radius r and outer radius $r + dr$ (as shown in figure 5.8) can be calculated as follows:

$$\begin{aligned} dE_s(r) &= E_s(r + dr) - E_s(r) \\ &= E_p(r + dr)\tfrac{s}{p}(r + dr) - E_p(r)\tfrac{s}{p}(r) \\ &= E_p\left(\tfrac{s}{p}(r + dr) - \tfrac{s}{p}(r)\right), \end{aligned} \tag{5.7}$$

using the fact that the primary component E_p is constant with a fixed phantom thickness H.

The amount of scattered radiation reaching the detector effectively stops increasing once the field radius is greater than some radius R. The stopping radius R increases with phantom thickness H. At this radius, the scatter-to-primary ratio is $\frac{s}{p}(R)$, and the total scatter can be written as follows:

$$E_s(R) = E_p\tfrac{s}{p}(R) \tag{5.8}$$

Thus the proportion of the total amount of scattered radiation coming from any cylinder as described above is:

$$\frac{dE_s(r)}{E_s(R)} = \frac{\frac{s}{p}(r + dr) - \frac{s}{p}(r)}{\frac{s}{p}(R)} \tag{5.9}$$

This equation allows the percentage of the total amount of scattered radiation coming from the hollow cylinder with the width of a pixel and various radii to be estimated. Figure (5.9) gives the results from these approximations for the situation in which the detector is considered to be the centre pixel and the radius is in terms of pixels.

These results form the basis for deriving the weighting mask w which represents where in a neighbourhood around each pixel the scattered photons come from. The derivation assumes that the mask derived for lucite is similar to that which would be found for fat and interesting tissue. This is only an approximation as shown by apparent differences in the scatter distributions of different materials and different photon energies [55], [61], [70]. There is also differential absorption of the scattered photons, depending upon incident angle, by the intensifying screen.

In order to apply the grid data to the results presented, some knowledge is needed of the angle at which the scattered photons arrive. This requires an assumption about the height of the scattering locations within each hollow cylinder. We assume that the initial scattering locations are distributed evenly. Consider a typical hollow cylinder,

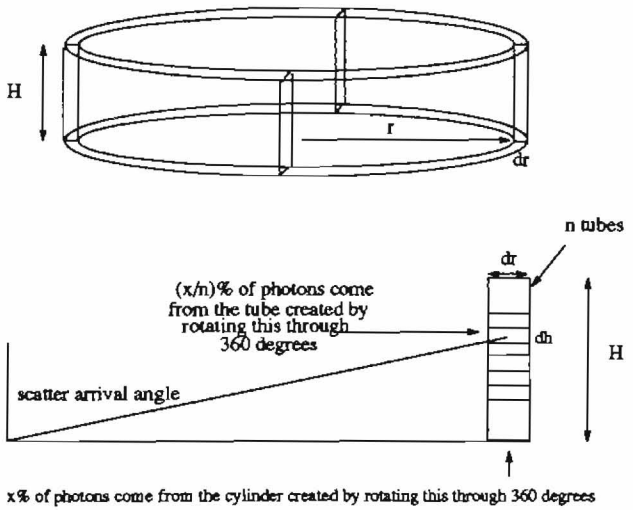

Figure 5.8: The data reported by Barnes and Brezovich [4] allows us to estimate the percentage of the total scattered photons coming from any chosen cylinder (top) and reaching the detector. In order to use the grid data reported by Dance et al. [20], the scatter arrival angle needs to be known. In order to know this, we divide the cylinder into n horizontal tubes and assume an equal percentage of the scattered photons comes from each tube.

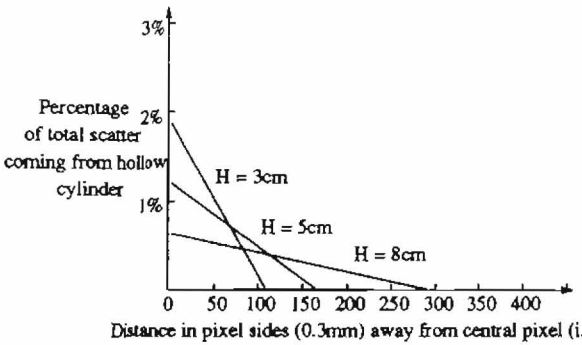

Figure 5.9: Percentage of total scatter coming from the hollow cylinder with the width of a pixel (0.3mm) and various radii for a lucite phantom of various thickness. Derived using the results of Barnes and Brezovich [4].

and divide this into n horizontal tubes, figure (5.8). Let $x\%$ be the percentage of the total scattered photons reaching the central pixel from the cylinder. The percentage of the total scattered photons reaching the centre from each tube in the cylinder is $x/n\%$ with our assumption. In our implementation, each hollow cylinder is divided into 1mm high tubes, so that $n = 10H$. Let $p(r, h)$ be the percentage of the total scattered photons coming from the tube with inner radius r, outer radius $r + dr$, lower height h and upper height $h + dh$. From the assumption of even distribution:

$$p(r, h) = \frac{dF_s(r)}{F_s(R)n} \tag{5.10}$$

The evenly distributed assumption is made on the basis that although photons scattered nearer to the detecting pixel have less tissue to pass through and are therefore less likely to be attenuated, the actual number of photons further away from the detecting pixel is far greater.

The possibility of a scattered photon reaching the intensifying screen having been multiply scattered is not considered in this model because the scattering location being found is the initial scattering site, rather than the final scattering site. This has consequences when the grid data is applied because the angle from initial scattering site to pixel is used rather than the final angle. It is conjectured that this will not be significant and the results in the next section appear to vindicate this.

5.3.3 Defining scatter volume with grid

Mammography in the UK is always performed with the aid of an anti-scatter grid. This grid prevents photons traveling in unexpected directions (with respect to the source and position on the film) from reaching the film. Dance and Day [19] derived a formula expressing the transmission of photons through the grid as a function of varying directions and their later paper [20] reproduced the results with the transmission values integrated over the azimuthal angle, figure (3.8). This figure shows the values for transmission relative to that of primary photons. The primary photon transmission versus energy is shown in figure (3.7). The values given in these figures are for photons with energies between 12.5keV and 25keV. This does not quite cover the range of energies used in mammography but suffices since a massive proportion of the photons are within this range. Let $t(\theta)$ be the relative transmission through the grid for a photon with scatter arrival angle θ.

Using the scatter volume derived from the work of Barnes and Brezovich, the percentages of scatter from the various initial locations are redefined by application of Dance and Day's grid transmission values for the angle at which the photon would have arrived at the grid if singularly scattered. For simplicity, rotational symmetry is assumed and the grid transmission values integrated over the azimuthal angle are used. Let $p_g(r, h)$ be the percentage of the total scattered photons, when an anti-scatter grid is used, coming from the tube with inner radius r, outer radius $r + dr$, lower height h, upper height $h + dh$:

$$\theta = \tan^{-1}\left(\frac{r}{h}\right)$$

$$p_g(r, h) = p(r, h)t(\theta) \tag{5.11}$$

Figures (5.10) and (5.11) show $p_g(r, h)$ summed over h for each r, for phantoms 3cm and 6cm thick respectively (effectively showing the amount of scatter from each cylinder). As expected, a greater proportion of the scattered photons come from nearer the centre pixel when an anti-scatter grid is used. This effect is unavoidable if the primary signal is not to be attenuated greatly.

The values of $p_g(r, h)$ are quantized into weighting masks w where the value (or height) at each pixel is directly proportional to the percentage of the total scattered radiation coming from the column of tissue above that pixel and reaching the central pixel. The masks vary for each breast thickness; the thicker the breast the more likely that the scattered photons come from further away. Figures (5.12) and (5.13) show the masks for 3cm and 6cm as three dimensional plots.

The reduction in scatter-to-primary ratio that application of the grid formula predicts is of the same order that Carlsson et al. [11] report in their theoretical study (a reduction factor of between 5 and 6). The values are not directly comparable because

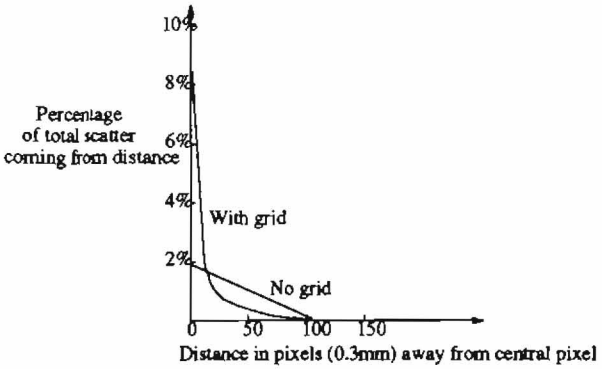

Figure 5.10: Percentage of total scatter coming from the cylinder with radii as marked, for a lucite phantom of thickness 3cm. The curves for both with and without grid are marked. Notice how the grid makes the scatter much more dependent on the local tissue.

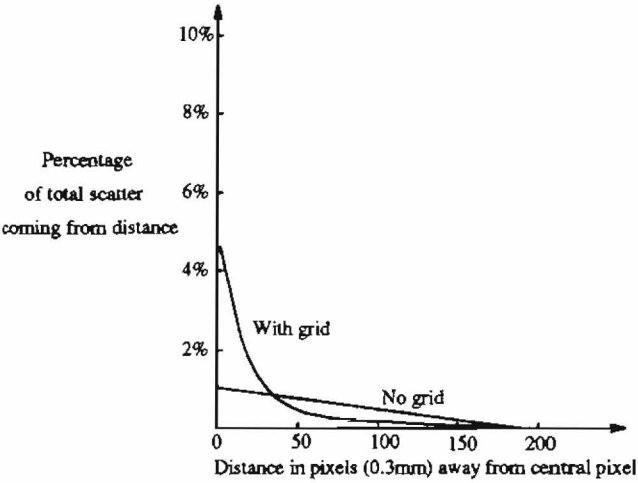

Figure 5.11: Percentage of total scatter coming from the cylinder with radii as marked, for a lucite phantom of thickness 6cm. The curves for both with and without grid are marked.

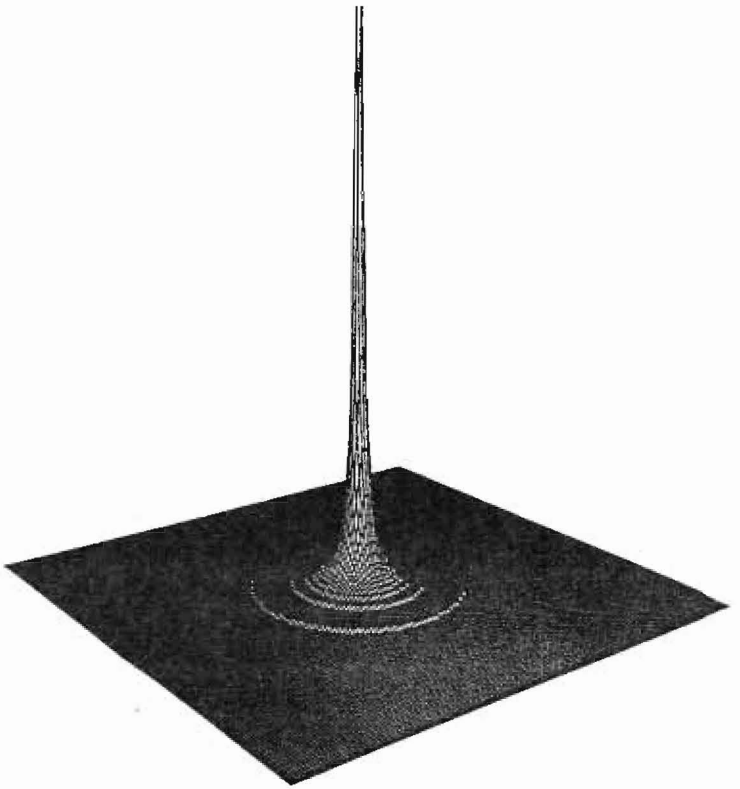

Figure 5.12: The weighting mask derived for a breast of thickness 3cm. This mask represents where the scattered radiation comes with the centre of the mask being the pixel of interest, and the height being directly proportional to the amount of scatter coming from that column of tissue.

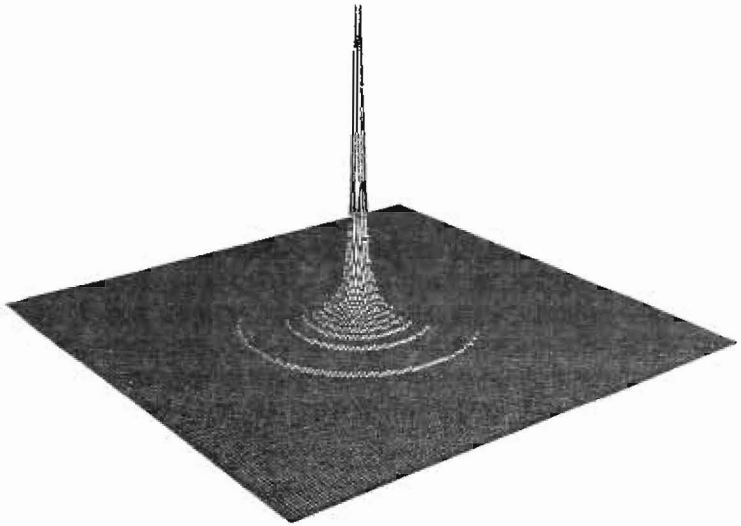

Figure 5.13: The weighting mask for a breast of thickness 6cm. This mask represents where the scattered radiation comes from with the centre of the mask being the pixel of interest, and the height being directly proportional to the percentage of the total scatter coming from that column of tissue. The range from which the scattered photons come increases with breast thickness, and thus this mask is shorter but broader than the previous one.

Carlsson et al. use breast tissue rather than lucite, and photon energy has an important bearing on the result. As an example, our method predicts a reduction factor of 5.8 in the scatter-to-primary ratio when the primary transmission is considered at 20keV and the lucite is 5cm thick, compared to the reduction by a factor of 5.2 which Carlsson et al. report for a 5cm thick breast consisting of 50% fat and 50% glandular tissue by mass. This supports our earlier assumptions about the initial scattering locations and scatter arrival angle.

The use of an anti-scatter grid obviously reduces substantially the amount of scattered radiation. Despite this, it is of concern that using the grid makes the scatter component more reliant on the local tissue, and is thus of a higher frequency than would be the case with no grid. This suggests that removing the scattered radiation digitally when a grid is *not* used might be a good deal easier than when a grid is used with the enormous consequences of avoiding the large increase in radiation dose to the breast which occurs with grid use.

5.3.4 Estimate "scatter function"

A weighting mask $w(x, y)$ has been calculated which represents the percentage of the total scatter reaching the central pixel coming from the column of lucite above each pixel in the neighbourhood $\mathcal{N}$. The aim now is to estimate the amount of scattered radiation at the central pixel by convolving the weighting mask with the imparted energy image $E(x, y)$, and using the resultant convolution sum as the input to a "scatter function" s. It is this function which is determined here.

Let $U(x_c, y_c)$ be the convolution sum at the pixel (x_c, y_c):

$$U(x_c, y_c) = \sum_{(x_c - x, y_c - y) \in \mathcal{N}} E(x_c - x, y_c - y) w(x, y), \tag{5.12}$$

where $\mathcal{N}$ is a neighbourhood around (x_c, y_c) assumed initially to lie completely within the breast shadow. The neighbourhood required contains most of the initial scatter locations, and can be determined when creating the weighting mask. The neighbourhood size increases with breast thickness. The relationship between U and scatter is determined using three example cases.

Carlsson et al. [11] calculated theoretically the scatter-to-primary ratios for blocks of both homogeneous tissue (100% fat, 100% interesting) and blocks of 50/50 fat to interesting tissue. These ratios are shown in table (3.2). The scatter-to-primary ratios given by Carlsson et al. do not include the effects of extra-focal radiation and are averages over the breast shadow. They report that the scatter-to-primary ratio for a point in the centre of the breast is around 15% higher than the average.

For each of the example blocks of tissue the relative energy imparted to the intensifying screen due to primary photons can be estimated from equations (3.18) and (3.21) for each specific breast thickness and exposure :

$$F_p(x_c, y_c) = \frac{F_p^{real}(x_c, y_c)}{F_{X_{ref}}^{real}}$$

$$= \frac{X_c}{X_{ref}} \frac{\int_0^{28} N_0^{ref}(E)\, E\, S(E)\, G(E)\, e^{-\mu_{tar}(E) h_{plate}}\, e^{-h\mu(x_c, y_c; E)} dE}{\int_0^{28} N_0^{ref}(E)\, E\, S(E)\, G(E)\, e^{-\mu_{tar}(E) h_{plate}} dE}, \quad (5.13)$$

where $h\mu(x, y; E)$ is the combined linear attenuation at energy E of the different tissue combinations.

Once $F_p(x_c, y_c)$ is known, the scatter-to-primary ratio can be used to find $F_s(x_c, y_c)$ from equation (5.5). Knowing this, the convolution sum $U(x_c, y_c)$ can be found for each of the different blocks of tissue at the specific breast thickness as can the energy imparted to the screen due to scatter:

$$F_s(x_c, y_c) = F_p(x_c, y_c) \times \frac{F_s}{F_p} \quad (5.14)$$

The function s from convolution sum to scatter can be approximated with the three known values of the convolution sum and energy imparted due to scatter. In fact, this function turns out to be linear, figure (5.14). Since 100% fat and 100% interesting tissue are the two extreme situations, any heterogenous tissue block will have a value of U between them.

We propose that using this function the scatter component at any pixel in an image of a heterogeneous breast can be found by using the appropriate weighting mask for the breast thickness convolved with the real imparted energy $E(x, y)$ as the input. In effect, we are using the convolution sum to estimate the composition and placement of the local breast tissue, and then mapping this estimate to a value of the scatter component.

The model does not, and cannot, differentiate between a block of fat with a layer of interesting tissue at the bottom and a block of fat with a layer of interesting tissue at the top. In both these cases the primary energy imparted will be the same, yet it is likely that the scattered radiation distribution will be different. No data is available to indicate the potential error here.

A further source of concern is that the scatter model depends on the relationship between energy imparted to the surrounding neighbourhood and scatter component at the central pixel. In fact, the energy imparted to the surrounding neighbourhood itself depends on the scattered radiation coming from the tissue outside the neighbourhood. Again, it is difficult to judge the error, but one might consider a two-pass algorithm in which the second pass uses the predicted primary components to predict more accurately the scattered components, which are then used to update the primaries.

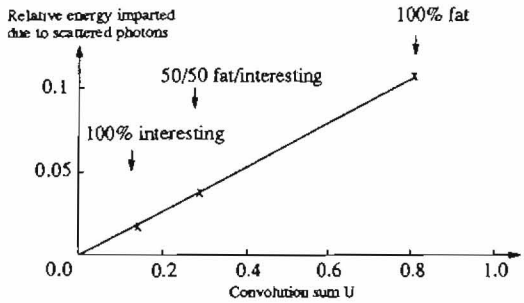

Figure 5.14: The scatter function s from the convolution sum U to scatter component, for breast thickness 6.5cm. The convolution sum U for the three references cases are marked.

5.3.5 Estimating extra-focal and breast edge effects

The scatter function s and weighting mask w are an effective way of describing the relationship between the energy imparted to the screen in an area around a pixel and the scatter component of the imparted energy at that pixel. However, this relationship only holds in the areas of the breast away from the breast edge. As the breast edge is approached extra-focal radiation and breast edge effects become apparent [20], [63].

At the edge of the breast (i.e. at the border with the film, not at the border with the chest wall), the thickness of the breast decreases rapidly. This has two effects: the amount of scatter produced in this area of the breast and travelling towards the screen is reduced, but scatter has to pass through less tissue to reach the screen.

Lam and Chan [63] investigated the image improvement obtained when a balloon full of water (similar attenuation properties to our interesting tissue) was put around the edge of the breast. They found significant image enhancement by this process and concluded that one of the reasons was the reduction of scattered radiation (along with compression of the dynamic range).

Figure (5.15) shows the scatter-to-primary ratios which are derived from the scatter fraction reported by Lam and Chan for a series of points along one radial of their 4.5cm thick water phantom, an anti-scatter grid was not used. There is a large decrease in the ratio towards where the chest wall would be. This decrease is due to the scattered

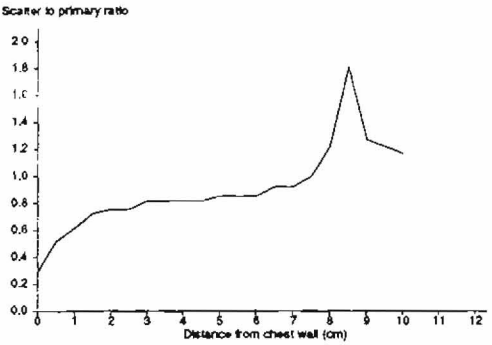

Figure 5.15: Scatter-to-primary ratio found by Lam and Chan [63] for a 4.5cm thick water phantom without an anti-scatter grid. The phantom has uniform thickness up to 8.5cm. The decrease at the chest wall is due to scattered radiation only coming from one side. The increase at the breast/film interface is due to breast edge effects and extra-focal radiation. The ratio dips close to the edge due to the water phantom thickness decreasing rapidly and the consequent rise in the primary component, rather than the scatter component reducing.

radiation only coming from one side. Towards the phantom edge there is a large increase. It is here that extra-focal radiation and the phantom edge play their part. The scatter-to-primary ratio starts to increase well within the phantom (before the thickness starts to decrease at 8.5cm); this reflects the penetration of the extra-focal radiation. The decrease in the scatter-to-primary ratio after 8.5cm reflects the fact that the primary is now rising rapidly due to the decreasing phantom thickness. Figure (5.16) shows the relative scatter component of the signal computed by multiplying the scatter-to-primary ratios by the relative primary components, which were also reported by Lam and Chan.

When the weighting mask w is applied at the very edge of the breast, around half of the mask falls outside the breast area and half inside. Thus, without taking any account of the edge effects, the scatter component at the edge is already being partly estimated. In fact, the estimate is similar to that at the chest wall where the convolution uses zero if the mask falls outside the breast image. Taking this into consideration, the edge effect value E_{out} (the value to use when the mask falls outside the breast area but on the film) must refer only to the excess scattered radiation reaching the film and extra-focal radiation. Letting $\mathcal{B}$ be the breast area, and $\mathcal{I}$ be the whole image, the convolution sum

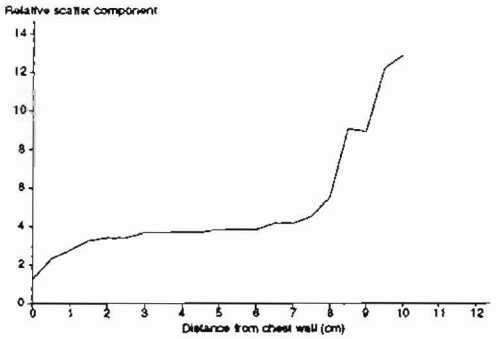

Figure 5.16: Relative scatter component for a 4.5cm water phantom, calculated from the values reported by Lam and Chan [63]. Notice that the scatter component rises rapidly near the breast edge with the film, this is in spite of the fact that the scattered radiation from the breast itself is only coming from one side (the same as near the chest wall). Extra-focal radiation and the breast edge are obviously having a large effect.

U becomes:

$$\begin{aligned} U(x_e, y_e) &= \sum_{(x_e-x, y_e-y)\in(\mathcal{N}\cap\mathcal{B})} F_t(x_e - x, y_e - y)w(x, y) + \sum_{(x_e-x, y_e-y)\in(\mathcal{N}\cap\mathcal{B}^c\cap\mathcal{I})} F_{out}w(x, y) \\ &= \sum_{(x_e-x, y_e-y)\in(\mathcal{N}\cap\mathcal{B})} F_t(x_e - x, y_e - y)w(x, y) + F_{out} \sum_{(x_e-x, y_e-y)\in(\mathcal{N}\cap\mathcal{B}^c\cap\mathcal{I})} w(x, y) \end{aligned}$$

In order to find F_{out}, the minimum and maximum scatter contributions are estimated along a line from the middle of the chest wall out to near the nipple. The minimum scatter exists at the back of the breast, well away from the breast edge and extra-focal radiation. Consequently, it is possible to use the weighting mask w and scatter function s to determine the minimum scatter F_{smin}. The ratio of maximum to minimum scatter from the data of Lam and Chan is now used to determine the maximum scatter F_{smax}. Let U_{max} be the convolution sum necessary to be entered to the scatter function s in order to give F_{smax}:

$$U_{max} = s^{-1}(F_{smax})$$

It is this sum which is required when the weighting mask is applied at the breast edge (x_e, y_e), and hence F_{out} can be determined:

$$F_{out} = \frac{U_{max} - \sum_{(x_e-x, y_e-y)\in(\mathcal{N}\cap\mathcal{B})} F_t(x_e - x, y_e - y)w(x, y)}{\sum_{(x_e-x, y_e-y)\in(\mathcal{N}\cap\mathcal{B}^c\cap\mathcal{I})} w(x, y)}, \tag{5.15}$$

The ratio of maximum to minimum scatter has to be taken slightly inside the breast edge because the digitizer cuts off film densities over 3.0, and therefore the breast edge on our images is slightly curtailed. The ratio of maximum scatter to minimum scatter that we use is 5.7, this was calculated by taking the maximum scatter as recorded by Lam and Chan when the film density reached 3.0. It seems reasonable to assume that this ratio holds not only for different breast thicknesses but also when a grid is used, since both minimum and maximum scatter values are affected by breast thickness in the same way, and the grid removes a percentage of the scatter rather than an absolute value.

Application of this technique gives an increasing scatter contribution as more of the weighting mask falls onto the film. The scatter contribution is equal to the sum of the weights lying outside the breast multiplied by the edge effect value, E_{max}. The amount of penetration of the extra-focal radiation which this method gives depends on the distance at which the values in the weighting mask drop off (figures 5.10 and 5.11), and compares favourably with the results reported by Lam and Chan for their 4.5cm thick water phantom.

One mammographic sign to be aware of while dealing with extra-focal radiation and the breast edge effect is skin thickening. This presents as a white edge to the breast image and is exactly what would be seen if the scatter component were overestimated at the edge. It is therefore critical that the effects of the breast edge and extra-focal radiation are treated carefully. The results from the model verification process explained in section (5.4) indicate that we have modeled the edge effects sufficiently accurately.

5.3.6 Finding primary component and displaying

Using the weighted scatter algorithm, the scatter and thus the more important primary, component of the energy imparted can be determined. Figure (5.17) shows six reduced mammographic images, and figure (5.18) shows the scatter component computed for each image. The primary component determined for the image in figure (5.1) is given in figure (5.19).

In order to generate an image which the radiologist can more easily understand it is necessary to convert the primary component back to the form in which the radiologist usually sees it. Unfortunately, direct methods fail because the primary component by itself is not large enough to expose the film to give a viewable image. The approach taken is to apply the automatic exposure control model described in chapter 4 to set an appropriate theoretical exposure. This effectively applies a multiplier to the energies imparted due to the primary component until the average film density in the automatic

exposure control area is as required. Using the automatic exposure control model makes the display process far more robust to noise since an average over a large area is being taken. Of course, this area does not have to be the area which the real automatic exposure control covers, but we seek to show the effects of scatter removal, and not the effects of optimal placement of the automatic exposure control.

5.3.7 Results from removal of scattered radiation effects

Figure (5.20) shows the original mammographic image GML1. The measured breast thickness was 5.40 cm, and the exposure was 76.1 mAs. The average film density above the AEC was 1.61. Figure (5.21) shows the result of scatter removal, and then re-exposure to get the same film density beneath the AEC. There is notable feature sharpening.

Figure (5.22) shows the original mammographic image FDL1. The measured breast thickness was 5.55 cm, and the exposure was 70.5 mAs. The average film density above the AEC was 1.42. Figure (5.23) shows the result of scatter removal.

Figure (5.24) shows an original mammographic image MMR1, and figure (5.25) shows the result from the weighted scatter algorithm. Both images are made to have the same average film density above the AEC. Again, there is notable feature enhancement particularly in the dense areas which is where the radiologist has most interest.

The final example is figure (5.26) which shows segments taken from mammographic images before and after scatter removal. The figure contains several microcalcifications which have been verified by a radiologist.

The weighted scatter removal algorithm is essentially a local high-pass operation, and this means that we can be certain that calcifications, if present, will be enhanced, despite not being included in the breast model; the images in figure (5.26) confirm this.

5.4 Verification of model

Verification of the model starts with comparing the calculated scatter-to-primary ratios with those predicted theoretically by Carlsson et al. [11] (shown in table 3.2). The measured breast thickness and exposure in mAs for each image is shown in table (5.2), whilst table (5.3) shows the calculated scatter-to-primary ratios for our model. The ratios are of the same order as those predicted by Carlsson et al. and maybe a little higher which is to be expected since the values of Carlsson et al. are averages over the whole breast. The lowest scatter-to-primary ratio is found at the chest wall, and

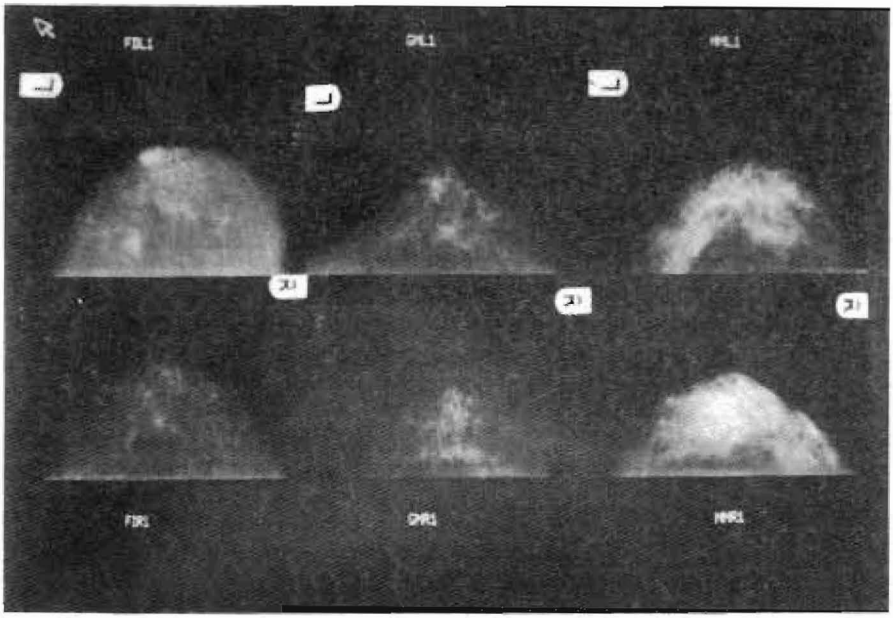

Figure 5.17: This is a selection of the images which the weighted scatter removal algorithm has been applied to.

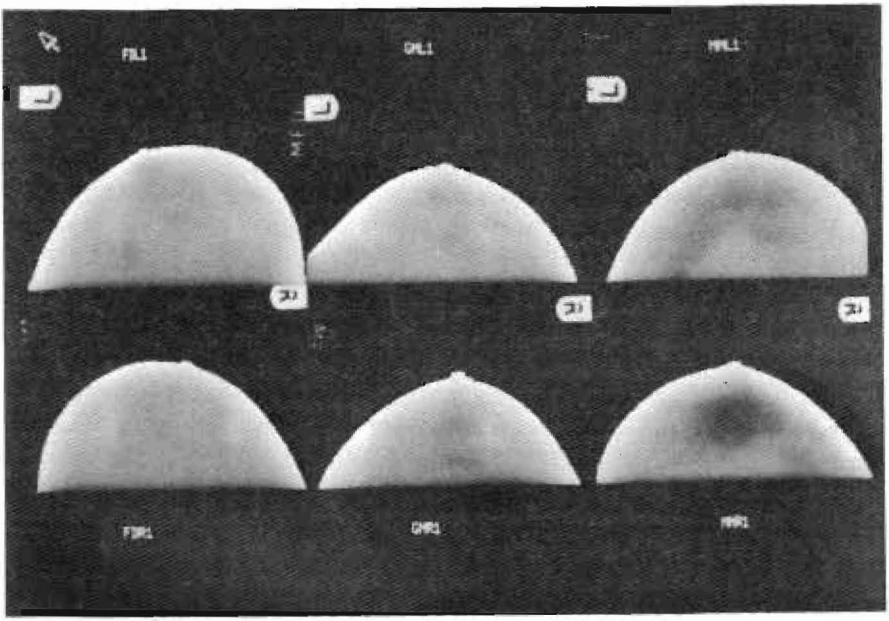

Figure 5.18: The computed scatter components for the images shown above. The film area outside of the breast area has been kept artificially dark.

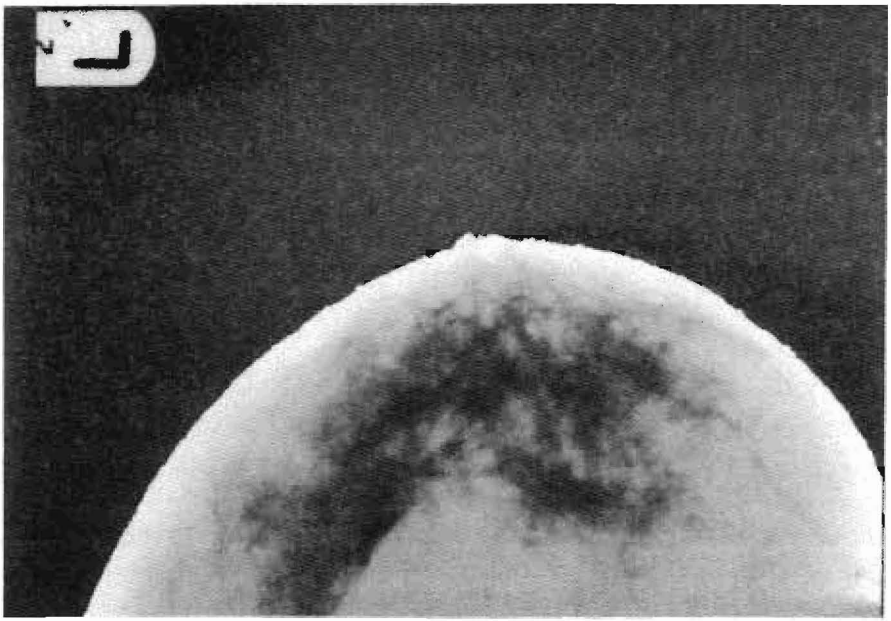

Figure 5.19: The primary component for image MML1 which is shown in figure 5.1. The film area outside of the breast area has been kept artificially dark.

the highest near the breast edge. In all the cases the maximum scatter-to-primary ratio is quite large. This is to be expected since the values of Carlsson et al. come from homogeneous blocks of tissue, but in real images it is possible to have a highly attenuating area surrounded by a less attenuating area, which gives a high scatter component and low primary component.

Significant verification tests of the whole model can be made by calculating the thickness of interesting tissue and fatty tissue through which the photons must have passed to give the calculated imparted energy at each pixel. The thickness can be estimated using equations (3.23) and (3.25). There are several possible verification tests which can be performed:

(V1) The thickness of interesting tissue calculated must be less than the length of the photon path through the breast.

(V2) The calculated thicknesses of interesting tissue over the whole breast must rise or fall according to the image perceived, thus high values are expected for "dense looking" breasts and low values are expected for "fatty looking" breasts. Since

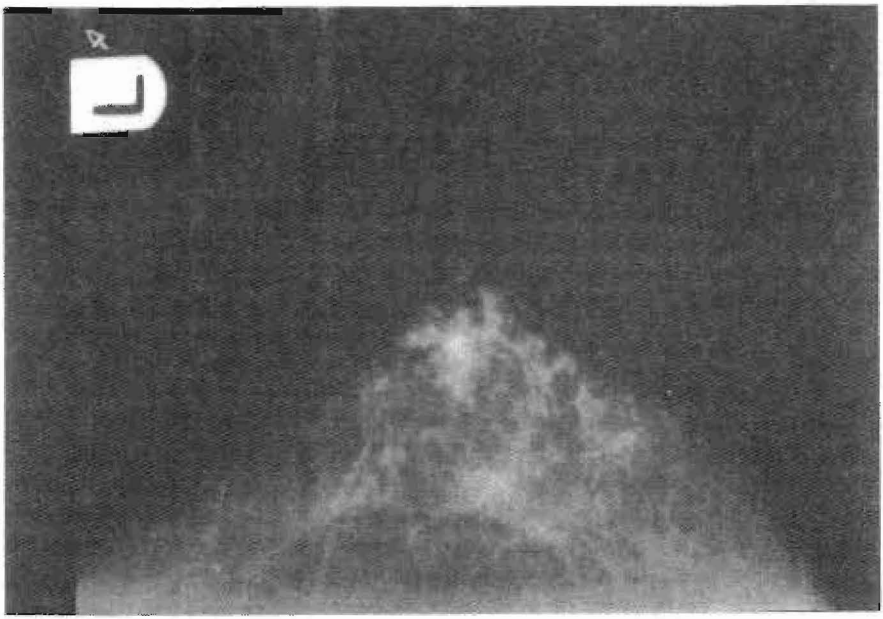

Figure 5.20: Image GML1, this is the original mammographic image of a breast of thickness 5.4cm, with exposure 76.1 mAs. The average density on the film above the AEC is 1.61.

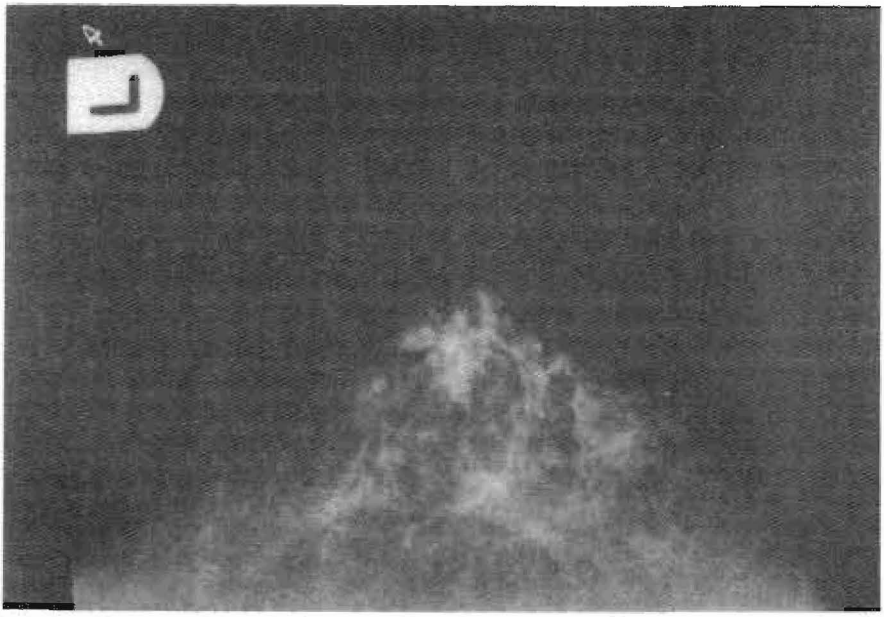

Figure 5.21: This is the scatter removed image for image GML1. The average density on the film above the AEC is 1.61.

Figure 5.22: Image FDL1, this is the original mammographic image of a breast of thickness 5.55cm, with exposure 70.5 mAs. The average density on the film above the AEC is 1.42.

Figure 5.23: This is the scatter removed image for image FDL1. The average density on the film above the AEC is 1.42.

Figure 5.24: Image MMR1, this is the original mammographic image of a breast of thickness 5.60cm, with exposure 106.0 mAs. The average density on the film above the AEC is 1.34.

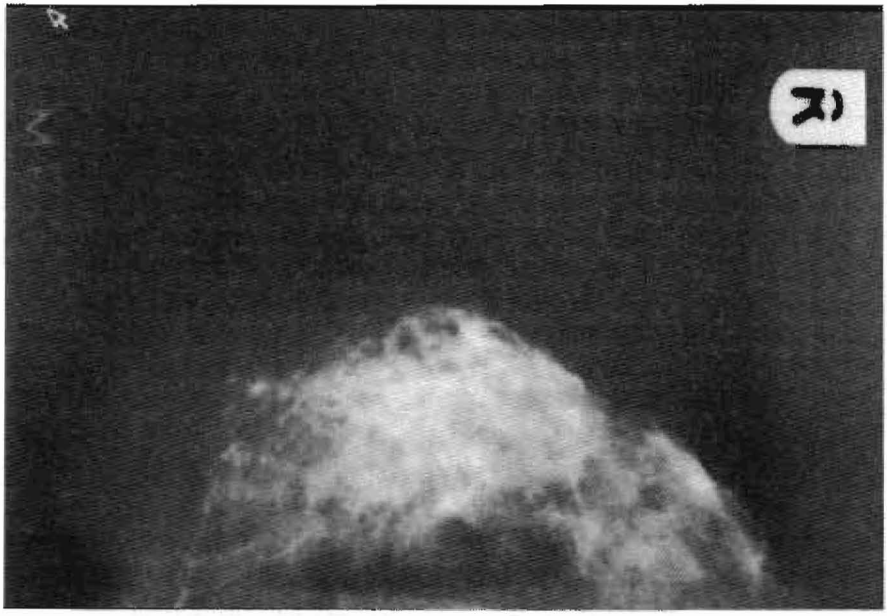

Figure 5.25: This is the scatter removed image for image MMR1. The average density on the film above the AEC is 1.34.

Image	Exposure (mAs)	Breast thickness (cm)
FDL1	70.5	5.55
FDR1	68.0	5.60
GML1	76.1	5.40
GMR1	72.9	4.95
MML1	90.0	5.09
MMR1	106.0	5.60

Table 5.2: The exposures and breast thicknesses for the some of the images shown in this chapter. The values are similar between left and right breasts, but, as we show in chapter 6, a difference of 0.5cm in the breast thickness can lead to gross differences in the mammographic images. Reduced versions of each of these images are shown in figure (5.17).

Image	$\frac{E_s}{E_p}$ min	$\frac{E_s}{E_p}$ average	$\frac{E_s}{E_p}$ max
FDL1	0.036	0.122	0.212
FDR1	0.054	0.124	0.293
GML1	0.061	0.119	0.230
GMR1	0.059	0.111	0.183
MML1	0.044	0.117	0.179
MMR1	0.038	0.128	0.214

Table 5.3: The calculated scatter-to-primary ratios from the weighted scatter algorithm. The average scatter-to-primary ratios are in the range which the theoretical work of Carlsson et al. [11] predicted. The maximum values of the ratios come from near the breast edge.

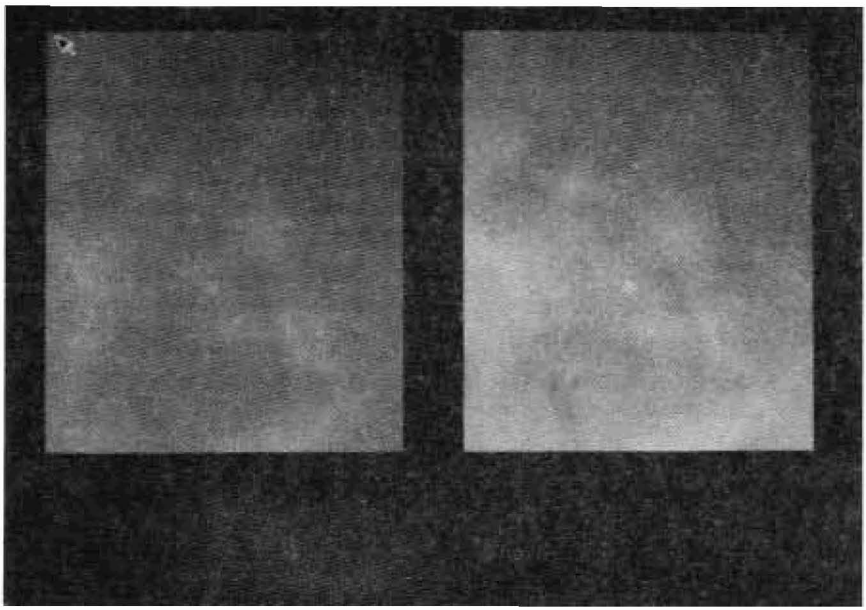

Figure 5.26: This is a segment taken from a mammogram, it shows several tiny microcalcifications. The segment on the left is the original. The microcalcifications have been enhanced by the use of the scatter removal algorithm. Over a small area such as this, the scatter component is practically constant.

this kind of calculation has not been performed before it is more revealing to use an estimate of the volume of interesting tissue.

(V3) The uniform breast thickness is lost at the edge of the breast, and since the breast edge is mostly fat, the thickness of interesting tissue found should actually be less than zero; indicating that the measured attenuation was too low even for 11 cm of pure fat.

(V4) The amount of interesting tissue estimated from two images of the same breast at different compressions should correspond on a pixel basis and be the same on a global basis. Correspond on a pixel basis implies that the thickness of interesting tissue found at corresponding pixels within the breast area is unlikely to rise with more compression.

Table (5.4) shows a summary of the interesting tissue calculations performed on

Image	Maximum h_{int}	Average h_{int}	Percentage of interesting tissue
FDL1	2.054	1.016	16.8
FDR1	2.800	0.538	8.5
GML1	2.750	0.980	16.7
GMR1	3.118	1.242	23.3
MML1	3.461	1.861	35.6
MMR1	3.808	1.866	31.8

Table 5.4: Results from the interesting tissue calculations. h_{int} is the thickness of interesting tissue which must have been present to give the calculated attenuation knowing the breast thickness and exposure. The equations for this calculation were developed in chapter 3. The percentage of interesting tissue is an estimate of the volume of interesting tissue in the breast as compared to the total volume. It is only an estimate as explained in section (3.2). The images referred to are all in figure (5.17).

the images shown in this chapter. The percentage of the breast which is interesting tissue comes from using the system geometry to estimate the respective volumes, with an approximation to include the volume of fat at the breast edge. The percentage of interesting tissue is low compared to that usually deemed to be standard for radiation dose calculations: 50/50 interesting tissue to fat by mass. This is partly due to work on estimating radiation dose assuming a straight edge breast, whereas here a volume of fat has been added to represent the breast edge. Clearly, verification test (V1) is satisfied. Furthermore, verification test (V2) is satisfied because the h_{int} values and percentages correlate exceptionally well with the perceived denseness of the breasts. For example, breast FDR1 is fatty whereas breast MMR1 is dense, and this shows up in both the average h_{int} values and percentages of volume of interesting tissue to volume of breast.

Verification test (V3) can be checked by transforming the original images to "interesting tissue" images, where the luminance is directly proportional to h_{int}. These images have very low contrast and show the extent to which mammography amplifies small differences in x-ray tissue attenuation. Figure (5.27) shows the various images transformed to interesting tissue images. The extremely white area around each breast edge represents where the thickness of interesting tissue was found to be less than zero. On all the images processed, a band like this has been found around the edge, and this satisfies the verification test (V3).

Verification test (V4) requires mammographic images of the same breast taken at different compressions. These images are supplied by the research described in chapter 6. Comparing the percentages of interesting tissue between the images with the

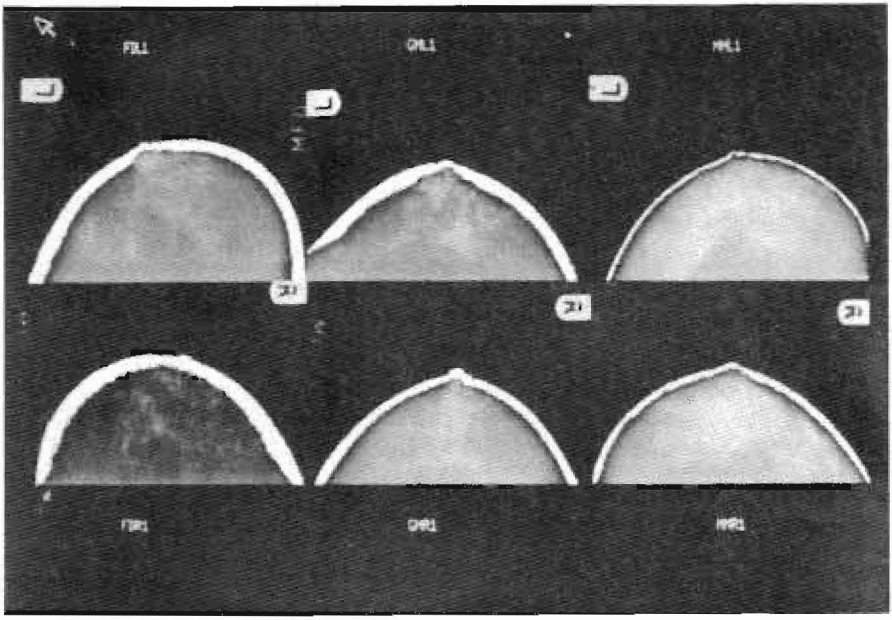

Figure 5.27: This represents the thickness of interesting tissue found for each pixel in various images. The brighter the value the greater the thickness of interesting tissue, except at the breast edge with the film. The extremely bright area around the edge represents where the thickness of interesting tissue was found to be less than zero. This is where the breast thickness starts to decrease rapidly.

compressed and less compressed breast consistently showed that the percentage of interesting tissue in the breast taken at less compression was greater than that in the breast taken at normal (full) compression. Investigating this, it appears that the mammograms performed at less compression do not have a constant breast thickness. As explained in chapter 6, the mammogram at most compression is performed first, the compression plate is let off, and then another mammogram is performed. It would appear that when the compression plate is let off, the breast fills the available space near the chest wall but fails to fill the space near the nipple; this was confirmed by the radiographers. Consequently, the less compressed breast images require a varying total thickness. The volumes of the breast and of the interesting tissue can be matched between the two images taken at different breast compressions by adjusting H by trial and error. Typically, this requires that the front of the breast (near the nipple) is given a

thickness increase of around half of that expected. This situation emphasises the need for accurate knowledge of the breast thickness.

Two further problems in matching volumes between the breasts exist. One is that as the breast is compressed blood appears to be compressed out of it, reducing the interesting tissue content. The other problem is that the digitizer only picks up film densities down to 3.0, and so the breast images might have different volumes of tissue actually imaged.

The thicknesses of the compressed breasts on which the mammograms were performed in this thesis are between 5 and 6 cm and this is fairly standard. In order to be complete in the verification two extreme examples were taken. In these cases the mammograms have not been digitized but the thickness of the breast and exposures were noted down. The first case was of a very thin breast which compressed to 3.3cm, and registered an exposure of 37.6mAs. Table (5.5) shows a mapping from film density to interesting tissue thickness with a scatter-to-primary ratio estimate of 0.1 taken across the film density range. If a film density of 1.5 is taken as the average, then the average h_{int} is 2.38cm, a large thickness given that the breast was compressed to only 3.3cm, and this reflects the reportedly dense nature of the breast. The second example was of a very thick breast which compressed to 7.5cm and registered an exposure of 314mAs. Table (5.6) shows a mapping from film density to interesting tissue thickness with a scatter-to-primary ratio of 0.15 taken across the film density range. If the average film density is taken to be 1.5, then the average interesting tissue thickness is around 2.175cm, which since the breast is 7.5cm thick is relatively small and implies the breast was fatty, as the radiographer reported.

The values found for thickness of interesting tissue correspond remarkably well to how the images look, and given the success of the verification tests with a variety of real images, which covered the extremes, we consider the model (both of scatter and of the breast) to be reliable.

5.5 Performing a monoenergetic examination

5.5.1 Theory

Given that the weighted scatter model appears reliable, simulation of a mammographic examination with a monoenergetic beam can take place. This is considered worthwhile for two reasons. The first is that beam hardening can degrade the contrast in dense or thick areas of the breast (figures 3.11 and 3.12), and the second is that the x-ray beam used in mammography is chosen as the result of a compromise between radiation dose

Film density	h_{int} cm
3.00	$* < 0$
2.75	0.264
2.50	0.660
2.25	1.089
2.00	1.485
1.75	1.914
1.50	2.376
1.25	2.805
1.00	3.267
0.75	$* > H$

Table 5.5: Relationship between film density and interesting tissue measurements, for a thin breast compressed to a thickness of 3.3cm and an exposure of 37.6 mAs. The scatter to primary ratio is taken to be 0.10. The * indicates when the interesting tissue thickness is either over the breast thickness, or when the attenuation is not large enough to have come from even pure fat. This mammogram was taken from the cranio-caudal direction, and the breast looked dense, as the interesting tissue thicknesses imply.

Film density	h_{int} cm
3.00	$* < 0$
2.75	$* < 0$
2.50	0.150
2.25	0.675
2.00	1.125
1.75	1.650
1.50	2.175
1.25	2.700
1.00	3.225
0.75	3.750

Table 5.6: Relationship between film density and interesting tissue measurements, for a thick breast compressed to a thickness of 7.5cm and an exposure of 314 mAs. The scatter to primary ratio is taken to be 0.15. This mammogram was performed from the medio-lateral direction, and the breast looks fatty, as the interesting tissue thicknesses imply.

to the breast and image quality. This compromise is redundant in our work since we are dealing only with the final images and it might be that simulating a different incident spectrum would improve the quality of the mammographic image.

Let E be the photon energy chosen for the monoenergetic simulation, then the primary component of the signal at pixel (x_c, y_c) is given as follows:

$$P_p(x_c, y_c) = N_0 F_E e^{-\mu h(x_c, y_c; E)}, \tag{5.16}$$

where N_0 is the number of photons, and $\mu h(x_c, y_c; E)$ is the estimate of the attenuation found from knowledge of h_{int} for the pixel and the linear attenuation coefficients at the appropriate energy. This equation can be expanded to illustrate the effect of the monoenergetic simulation :

$$\begin{aligned} P_p(x_c, y_c) &= N_0 F_E e^{-\mu h(x_c, y_c; E)} \\ &= N_0 F_E e^{-(\mu_{int}(E) h_{int}(x_c, y_c) + \mu_{fat}(E) h_{fat}(x_c, y_c))} \\ &= N_0 F_E e^{-(\mu_{int}(E) h_{int}(x_c, y_c) + \mu_{fat}(E)(H - h_{int}(x_c, y_c)))} \\ &= N_0 F_E e^{-(\mu_{int}(E) h_{int}(x_c, y_c) + H\mu_{fat}(E) - \mu_{fat}(E) h_{int}(x_c, y_c))} \\ &= N_0 F_E e^{-(\mu_{int}(E) - \mu_{fat}(E)) h_{int}(x_c, y_c) - H\mu_{fat}(E)} \\ &= N_0 F_E e^{-H\mu_{fat}(E)} e^{-(\mu_{int}(E) - \mu_{fat}(E)) h_{int}(x_c, y_c)} \end{aligned} \tag{5.17}$$

Across any image, the only factor in this equation that changes is $h_{int}(x_c, y_c)$. This means that the value of $\mu_{int}(E) - \mu_{fat}(E)$ has important implications for the contrast which the final image displays and the radiologist interprets from: the higher this difference, the greater the change of $P_p(x_c, y_c)$ with $h_{int}(x_c, y_c)$. The difference between the two attenuations coefficients rises as the photon energy is reduced, as shown in figure (3.5). The problem with having too low a photon energy is that the imparted energy range of values becomes too great to display. In practice, a low photon energy causes excessive radiation dose to the breast.

The area around the breast edge with the film which was found to have $h_{int} < 0$ is considered to consist of pure fat, and the attenuation found in this area is mapped to a thickness of fat only, h_{fat}. The monoenergetic photon beam in the simulation is attenuated theoretically by this thickness of fat before reaching the film-screen combination at the breast edge.

In terms of the final image, the amount of light transmitted through the theoretical film, T_l can be written as follows:

$$T_l(x_c, y_c) = \frac{I_l}{(\beta P_p(x_c, y_c))^\gamma}, \tag{5.18}$$

where I_l is the illuminating light intensity, and β and γ are the linear constants of the characteristic curve. Substituting equation (5.17) into this gives:

$$T_l(x_c, y_c) = \frac{I_l}{(\beta N_0 F_E)^\gamma} e^{H\mu_{fat}(E)\gamma} e^{(\mu_{int}(E) - \mu_{fat}(E)) h_{int}(x_c, y_c)\gamma} \tag{5.19}$$

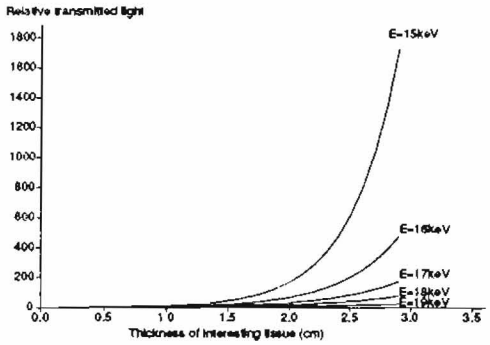

Figure 5.28: Variation of T_l with $h_{,nl}$ for different photon energies. The value of T_l shown is the varying factor and does not include the parts of the equation which are constant across any one image. The $h_{,nl}$ range corresponds to that found for image GML1. Although at 15keV there would obviously be a great deal more contrast, the dynamic range of T_l is far too great to be displayed (a range of 100 is the maximum on a film, and 40 is the maximum on the terminal screen - section 4.3). In real mammography, the range required is reduced by making low $h_{,nl}$ invisible unless a "hot light" is used.

Note that β and N_0 are multiplicative constants across the image, and that β is dependent on the reference energy used. The value of β used earlier in this work is not appropriate here because the energy values have now changed reference. However, this is of no great concern because the value of N_0 is to be manipulated by the automatic exposure control model in order to present a decent image, and it doesn't matter therefore what the value of β is since N_0 will be adjusted automatically. Figure (5.28) shows the relative variation of T_l in equation (5.19) with $h_{,nl}$ for different photon energies. Clearly, contrast is greatest at the low photon energies. However, the problem with high contrast is that it does not allow a large range of values to be shown. The problem can be overcome to some extent by altering the value of N_0, to show the particular range of interest. Figure (5.29) shows the effect of altering N_0 in equation (5.19) for a breast with an interesting tissue thickness range of 2.7cm. This figure shows the transmitted light relative to the illuminating light, and has the values cut-off at $D = 0.6$ and $D = 2.2$ to illustrate the visible range on the film.

Figure (5.30) shows the effect of having pixels with $h_{,nl} = 1.5$cm set to a film density of 1.5 for a range of different photon energies. This is effectively modeling the action of an automatic exposure control.

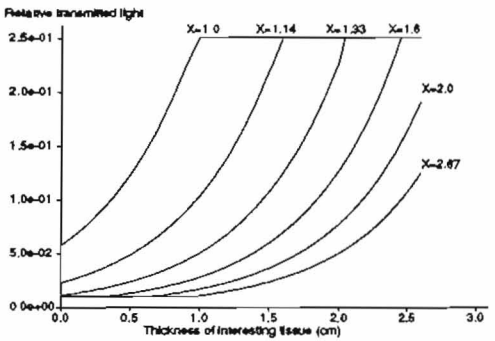

Figure 5.29: Variation of T_l with $h_{,,t}$ for different settings of N_0 at a photon energy of 18keV. The higher N_0 is, the higher the exposure (X) and thus the darker the film. The curves are marked relative to the minimum exposure. The T_l axis represents transmitted light in terms of the illuminating light. For example, 0.25 means $T_l = 0.25 I_t$, and this represents a film density of 0.6 ($10^{-0.6} = 0.25$). The graph shows that for very low N_0 (low X) settings most of the image is saturated, whereas for high N_0 settings the image is very dark. A value of between 1.6 and 2.0 X would be optimal.

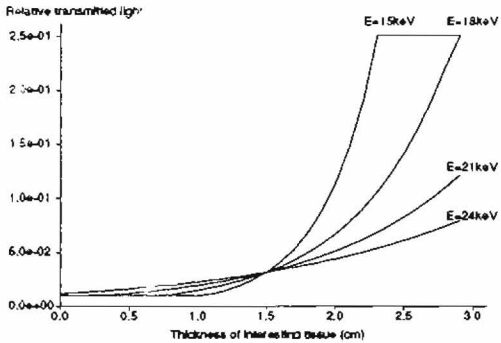

Figure 5.30: Variation of T_l with h_{int} for different photon energies. At each energy the exposure is being set so that $h_{int} = 1.5$ gives a film density of 1.5, which corresponds to a relative transmitted light value of 0.0316. The T_l axis represents transmitted light in terms of the illuminating light. For example, 0.25 means $T_l = 0.25 I_l$, and this represents a film density of 0.6 ($10^{-0.6} = 0.25$). In this situation, a photon energy of between 18 and 21 keV is optimal.

Figure (5.31) shows the result of theoretically performing a monoenergetic examination on breast MML1 four different photon energies: 15keV, 18keV, 21keV, 24keV. At the low photon energies there is far too much contrast and the image is saturated, as the energy rises the contrast is reduced and the entire image can be viewed without saturation. Further examples of the monoenergetic simulation are shown in the next section after a way of automating the choice of photon energy has been explained.

5.5.2 Automating the choice of photon energy

If the characteristic curve of the film-screen combination is kept the same, then for any pixel there are four unknowns in equation (5.19): a multiplicative constant (k), the photon energy E, the thickness of interesting tissue $h_{int}(x_c, y_c)$, and the transmitted light which comes through the film T_l. Rewrite the equation making these unknowns explicit:

$$T_l(x_c, y_c) = k e^{(\mu_{int}(E) - \mu_{fat}(E)) h_{int}(x,y)\gamma}, \tag{5.20}$$

where

$$k = \frac{I_l}{(HN_0E)^\gamma} e^{H\mu_{fat}(E)\gamma} \tag{5.21}$$

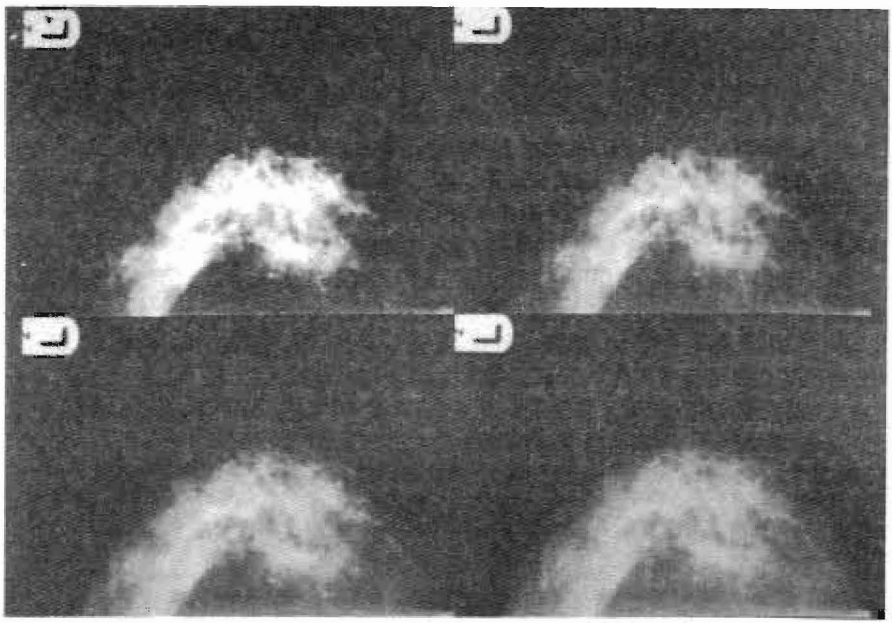

Figure 5.31: This shows the result of different photon energies in the monoenergetic simulation on breast MML1, with the automatic exposure control set to give an average density of 1.5. The top left image is for a photon energy of 15keV, the top right is 18keV, the bottom left is 21keV, and the bottom right is 24keV. As the photon energy increases the contrast is reduced, and the dynamic range decreases allowing the image to be viewed without saturation.

If two values of h_{im} are to be set to two specific film densities, then the two unknowns k and E can be calculated. For example, one possible mapping of the maximum h_{im} is to a film density of 0.6 (the minimum film density displayable). Another possible mapping is the average h_{im} across the image to a film density of 1.5 (the usual AEC setting). Let h_{im1} be mapped to D_1 and let h_{im2} be mapped to D_2. Replacing T_l by $I_l 10^{-D}$, cancelling the I_l from the equation for k, and then putting in the set values gives the following two simultaneous equations:

$$10^{-D_1} = ke^{(\mu_{mat}(E)-\mu_{fat}(E))h_{im1}}$$

$$10^{-D_2} = ke^{(\mu_{mat}(E)-\mu_{fat}(E))h_{im2}}$$

Dividing one equation by the other and rearranging yields an equation from which the required photon energy can be found by minimizing the error:

$$\mu_{int}(E) - \mu_{fat}(E) = \frac{(D_2 - D_1)\log_e 10}{(h_{int1} - h_{int2})\gamma}, \tag{5.22}$$

from this the constant k can be determined:

$$k = 10^{-D_1} e^{-(\mu_{int}(E) - \mu_{fat}(E))h_{int1}\gamma} \tag{5.23}$$

Figures (5.32), (5.33), (5.34) and (5.35) present four examples of the monoenergetic simulation, the choice of photon energy is given in each case. The automation of the choice of photon energy works well for most cases, although it is susceptible to noise (through using the maximum value of h_{int}), and the decision to set the average h_{int} over the entire breast to a film density of 1.5 might not be ideal in all situations.

The final example is figure (5.36) which shows a segment taken from a mammographic image before and after scatter removal. The image contains several microcalcifications which have been verified by a radiologist, and they have been greatly enhanced.

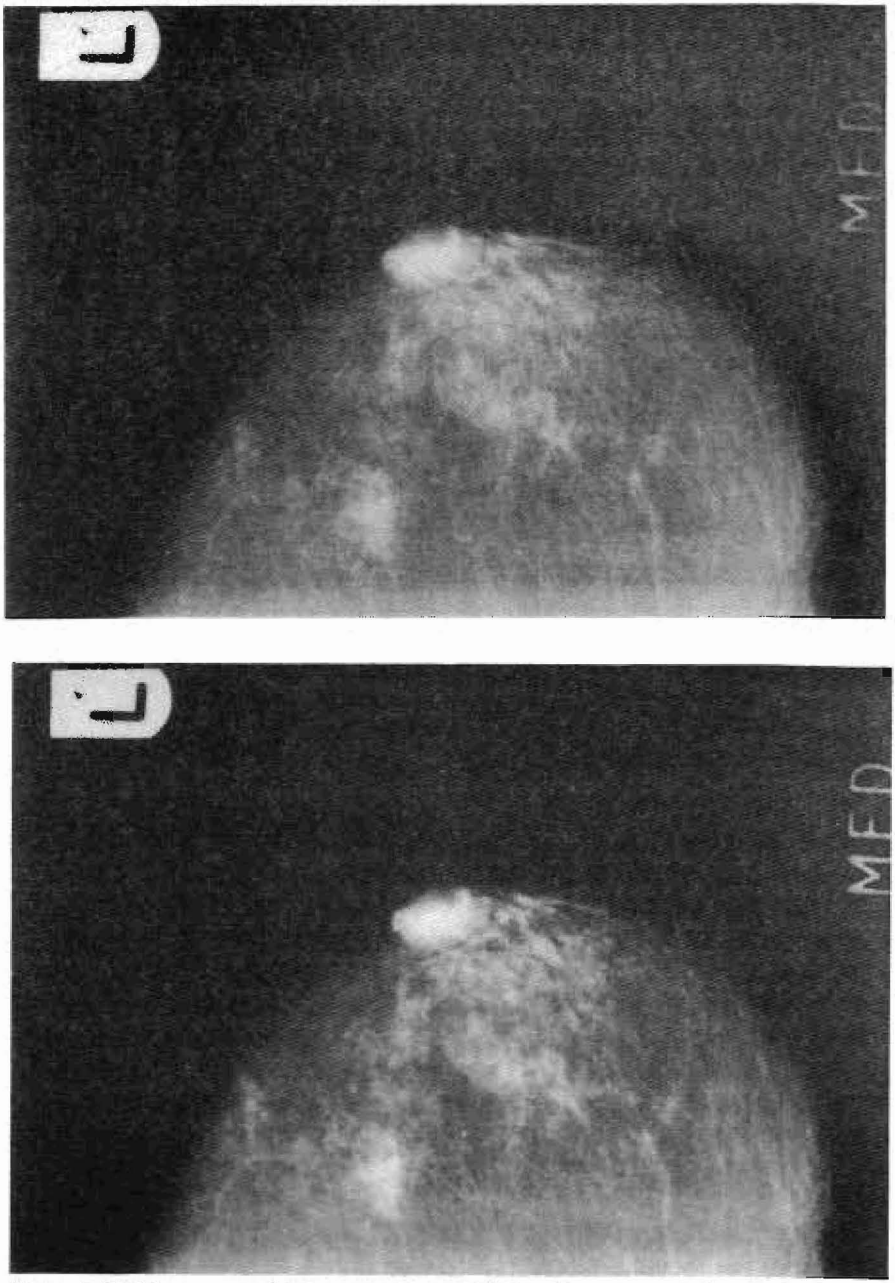

Figure 5.32: Mammographic images of breast FDL1. The top one is the original, and the bottom one is the result from the monoenergetic simulation with a photon energy of 16keV.

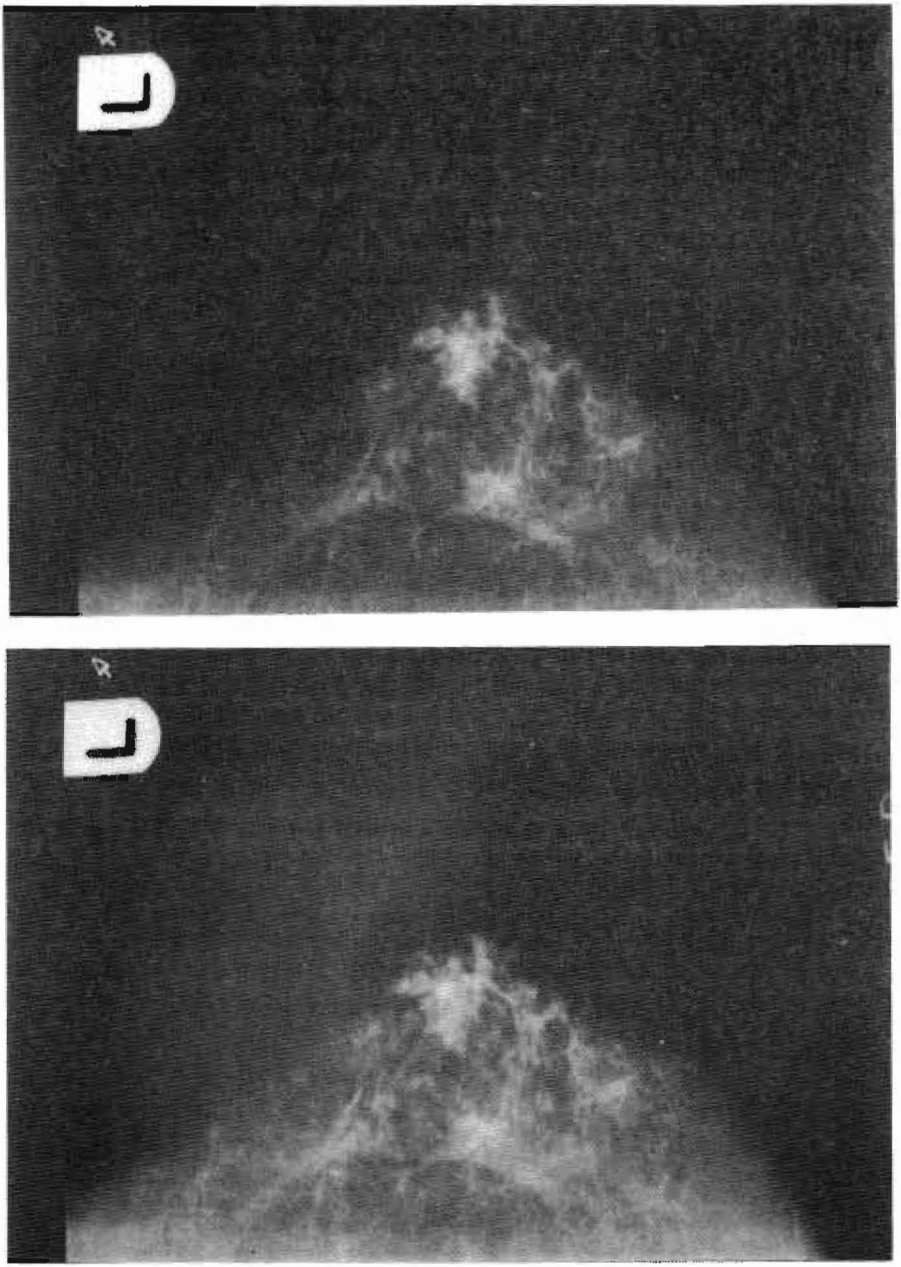

Figure 5.33: Mammographic images of breast GML1. The top one is the original, and the bottom one is the result from the monoenergetic simulation with a photon energy of 19keV.

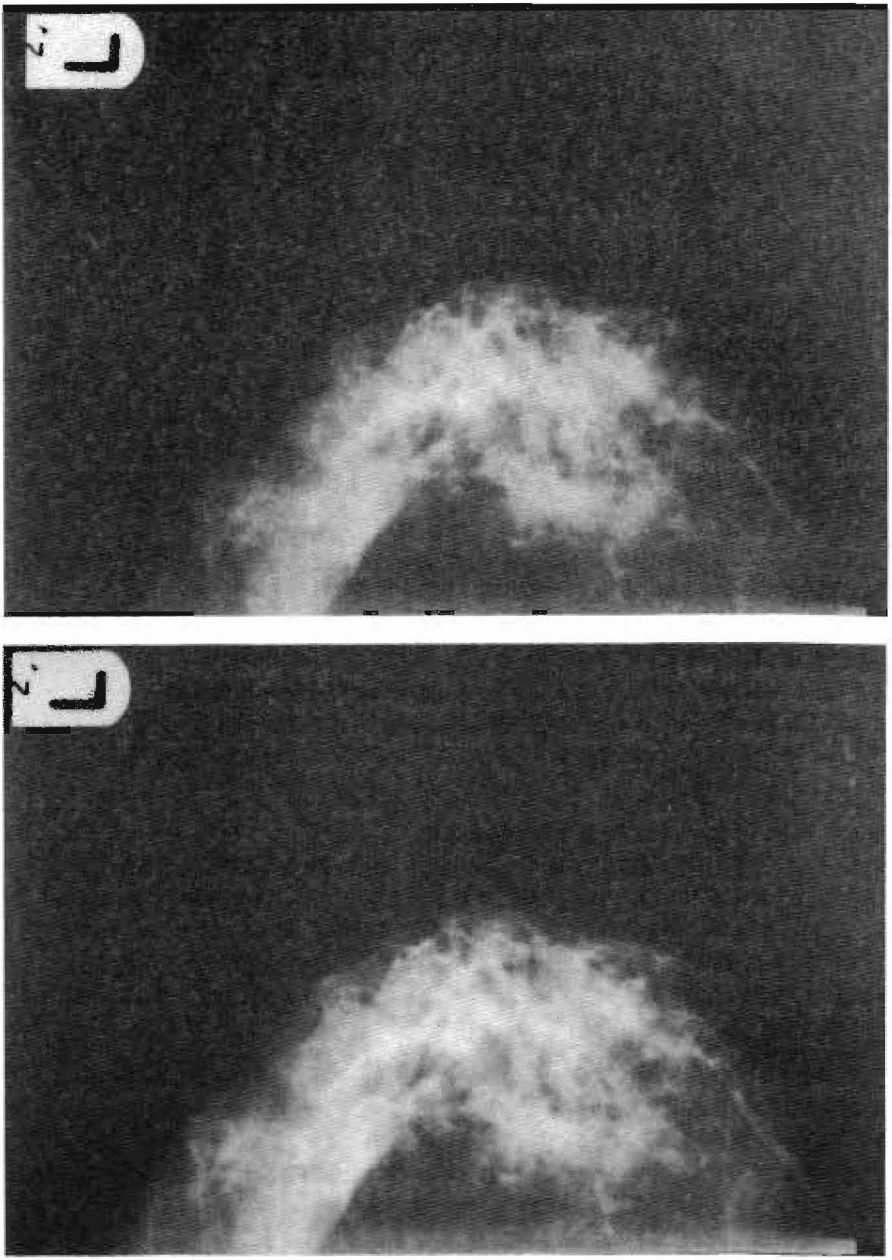

Figure 5.34: Mammographic images of breast MML1. The top one is the original, and the bottom one is the result from the monoenergetic simulation with a photon energy of 19.2keV.

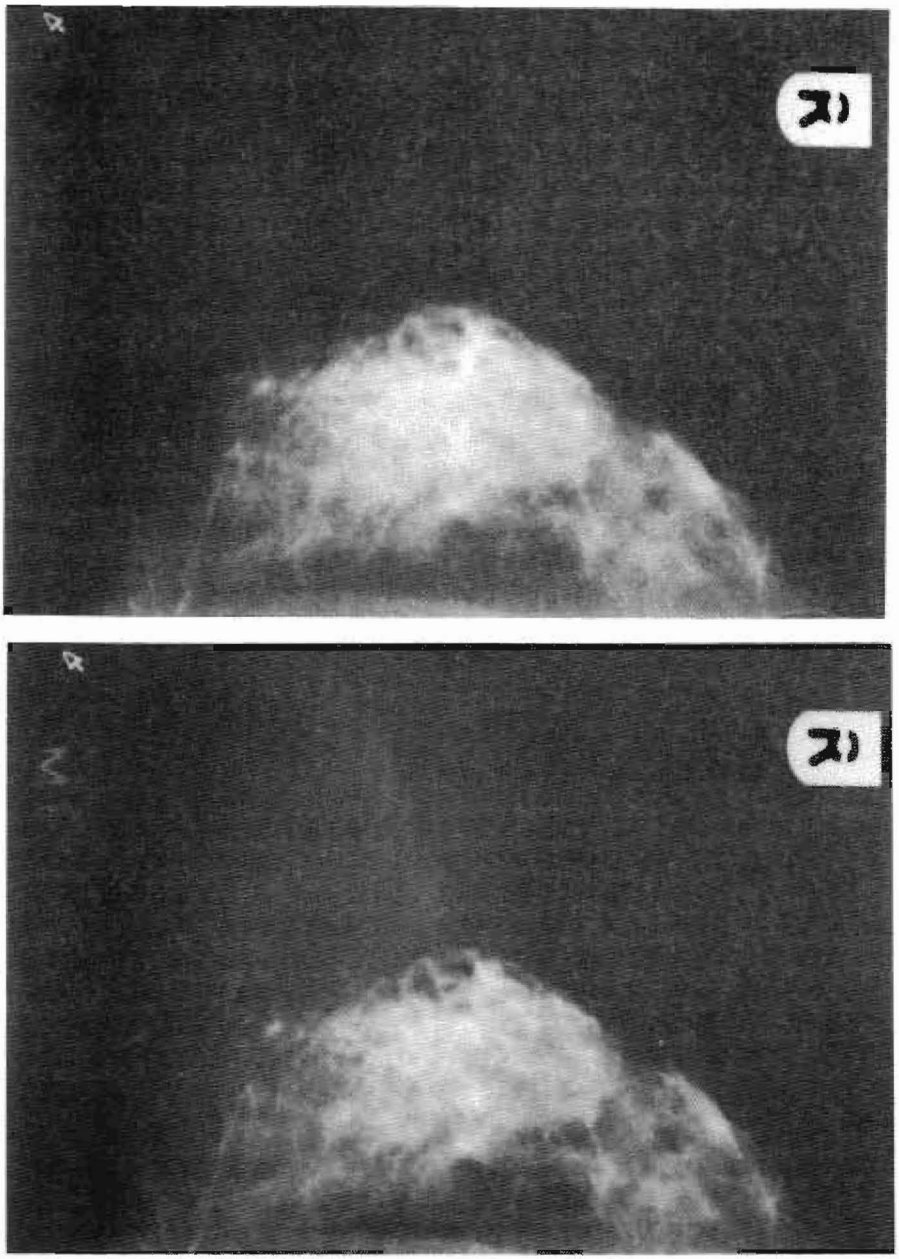

Figure 5.35: Mammographic images of breast MMR1. The top one is the original, and the bottom one is the result from the monoenergetic simulation with a photon energy of 19.5keV.

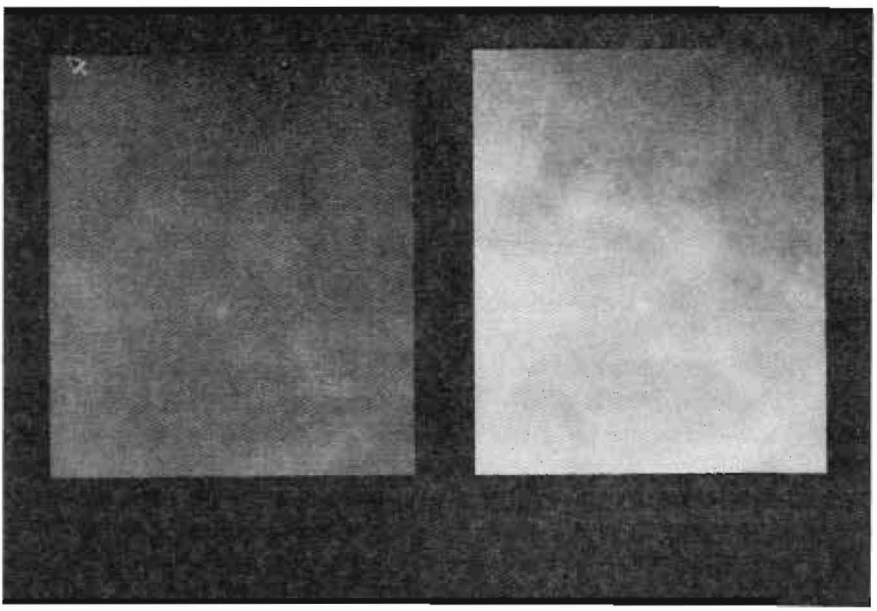

Figure 5.36: This is a segment taken from a mammogram, it shows several microcalcifications. The image on the left is the original, and the image on the right is the result of a monoenergetic simulation at 19keV.

5.6 Comments on modeling

In this chapter we presented two models of scattered radiation which were used to enhance the mammographic images. The constant scatter model is naive but enhances the images in a way which is easily understood, although the enhancement is more to do with basic image processing than the model of the scatter. The weighted scatter model is more accurate and produced quantitative values of the breast tissue which are exceptionally good when verified with practical results and measurements. The weighted scatter removal is of a high-pass nature and despite the use of the anti-scatter grid shows clear enhancement of the images, including calcifications. On the basis of the successful verification tests, the modeling was expanded to simulate a mammographic examination with a monoenergetic beam. The results of this modeling were exciting, and a way of automatically choosing a photon energy was described. Enhancement of specific mammographic signs by these methods is shown in chapter 7.

The algorithms developed in this chapter vary in their robustness to noise, and their applicability to images from different views. The constant scatter algorithm relies heavily on adequate segmentation of the breast area from the rest of the film and therefore shows no enhancement (although no degradation either) when the segmentation is poor, as is likely when the pectoral muscle is present. On the other hand, the weighted scatter algorithm is robust to noise and to view, with the automatic exposure control handling the robustness and the pectoral muscle being considered as highly attenuating for the scatter model. The monoenergetic simulation is also robust to noise, but the photon energy has to be carefully chosen to ensure the image is not too dark, and yet not saturated. The method we gave for choosing an optimal photon energy is not robust to noise due to its reliance on the maximum thickness of interesting tissue. The success of the monoenergetic simulations also relies on fine discrimination of the $h_{i,nl}$ values. If the $h_{i,nl}$ values are not found accurately enough, significant quantization error could occur. There is also a trade-off between the fineness of the discrimination and time.

5.7 Summary of chapter

In terms of the overall aim of our modeling this chapter has provided the missing link: a reasonable estimate of the scatter component. The crux of the chapter has been the development of the weighted scatter algorithm, which works on the energy imparted images, corrected for the spatially varying incident radiation intensity, supplied by the work in described in chapters 3 and 4. The first step is to determine a weighting mask w which represents for each pixel in a neighbourhood $\mathcal{N}$ of the central pixel what

percentage of the total scattered radiation comes from the vertical column of tissue at that pixel when the breast is homogeneous:

- From Barnes and Brezovich's data [4], the proportion of scatter $\frac{dE_s(r)}{E_s(R)}$ coming from a cylinder a distance r away from the centre, and dr wide can be found:

$$\frac{dE_s(r)}{E_s(R)} = \frac{\frac{s}{p}(r+dr) - \frac{s}{p}(r)}{\frac{s}{p}(R)},$$

  where $\frac{s}{p}(r)$ is the scatter-to-primary ratio for a radiation field of radius r, and R is the radius at which the ratio stops increasing. This calculation is specific to the thickness of the compressed breast on which the mammogram being considered was performed.

- The percentage of scatter $p(r,h)$ coming from a tube within the cylinder with radius r, and height h is:

$$p(r,h) = \frac{dE_s(r)}{E_s(R)n}$$

  where n is the number of such tubes in each cylinder: $n = \frac{H}{dh}$ with dh the thickness of each tube, and H the breast thickness.

- Apply the grid formula of Dance and Day [20] to get the percentage of scatter coming from each tube when an anti-scatter grid is used:

$$p_g(r,h) = p(r,h)t(\theta),$$

  where $\theta = \tan^{-1}(\frac{r}{h})$ is the scatter arrival angle, and t is the relative grid transmission.

- The last step is to integrate $p_g(r,h)$ over h, for all relevant r. The result of this integration is the proportion of scatter which comes from the cylinder with radius r when a grid is used. This is quantized to create a rotationally symmetric weighting mask w.

The next step is to find the scatter function which takes the value produced from the weighting mask convolved with energy imparted to give a scatter estimate, this is achieved using three calibration values:

- From the work in chapter 3, the primary component for each calibration case can be calculated:

$$E_p(x,y) = \frac{X_c}{X_{ref}} \frac{\int_0^{28} N_0^{rel}(E)\, E\, S(E)\, G(E)\, e^{-\mu_{air}(E)h_{plate}}\, e^{-h_\mu(x,y;E)} dE}{\int_0^{28} N_0^{rel}(E)\, E\, S(E)\, G(E)\, e^{-\mu_{air}(E)h_{plate}} dE},$$

  where $h_\mu(x,y;E)$ is the combined linear attenuation at energy E of the different tissue combinations: 100% interesting tissue, 100% fat, 50/50 interesting/fat.

- Using the scatter-to-primary ratios from Carlsson et al. [11] the energy imparted to the screen for the calibration cases can be predicted:

$$E_t(x,y) = E_p(x,y)(1+\tfrac{E_s}{E_p})$$

- As can be the scatter component:

$$E_s(x,y) = E_p(x,y)\tfrac{E_s}{E_p}$$

- U is the sum of predicted energy imparted convolved with the weighting mask w around a pixel (x_c, y_c):

$$U(x_c,y_c) = \sum_{(x_c-x,y_c-y)\in\mathcal{N}} E_t(x_c-x, y_c-y)w(x,y)$$

- At this stage, we have three corresponding values of U and E_s, and these define the scatter function s:

$$E_s(x_c,y_c) = s(U(x_c,y_c))$$

  In effect, U is a quantitative measure of the local tissue composition and placement, and on the basis of this we estimate the scatter component.

To take account of extra-focal radiation and breast edge effects, a value E_{out} is determined which is used then the weighting mask falls outside the breast area but within the image:

- To begin, the minimum scatter is estimated by convolving the weighting mask with the energy imparted image at a pixel near the chest wall and applying the scatter function to the result. A value of 0 is used if the mask falls outside the image. The ratio of maximum to minimum scatter from the data of Lam et al. [63] is then used to give the maximum scatter E_{smax}.

- The convolution sum required to obtain the maximum scatter is U_{max}:

$$U_{max} = s^{-1}(E_{smax})$$

- It is U_{max} which is required when the weighting mask is applied at the breast edge with the film (x_e, y_e), and hence E_{out} can be determined:

$$E_{out} = \frac{U_{max} - \sum_{(x_e-x,y_e-y)\in(\mathcal{N}\cap\mathcal{B})} E_t(x_e-x, y_e-y)w(x,y)}{\sum_{(x_e-x,y_e-y)\in(\mathcal{N}\cap\mathcal{B}\cap\mathcal{I})} w(x,y)},$$

  where $\mathcal{B}$ is the breast area of the image $\mathcal{I}$.

The primary component at each pixel (x_c, y_c) within the image can now be found:

- Convolve the weighting mask with the energy imparted image:

$$U(x_c, y_c) = \sum_{(x_c - x, y_c - y) \in (\mathcal{N} \cap \mathcal{B})} E(x_c - x, y_c - y) w(x, y) + \sum_{(x_c - x, y_c - y) \in (\mathcal{N} \cap \mathcal{B}^c \cap \mathcal{I})} E_{out} w(x, y)$$

- Apply the scatter function:

$$E_s(x_c, y_c) = s(U(x_c, y_c))$$

- Subtract the scatter estimate from the total energy imparted at the pixel to get the primary:

$$E_p(x_c, y_c) = E(x_c, y_c) - E_s(x_c, y_c)$$

The primary component can be input to the equations developed in chapter 3 to get a quantitative measure of the breast tissue, namely the thickness of interesting tissue h_{int}. To produce an image the primary component can be amplified using the automatic exposure control model of chapter 4, and then used to re-expose the film theoretically via the film-screen characteristic curve. Alternatively, a monoenergetic simulation can be carried out using the quantitative breast measures:

- The relative primary component in a monoenergetic simulation with photon energy E is:

$$E_p(x_c, y_c) = N_0 E e^{-H \mu_{fat}(E)} e^{-(\mu_{int}(E) - \mu_{fat}(E)) h_{int}(x_c, y_c)}$$

This value is amplified using the automatic exposure control model and then used to re-expose the film theoretically. The choice of photon energy and exposure can be automated by selecting two values of (h_{int1}, h_{int2}) to map to specific film densities (D_1, D_2):

- The light transmitted through the film can be written with two unknowns:

$$T_l(x_c, y_c) = k e^{(\mu_{int}(E) - \mu_{fat}(E)) h_{int}(x, y) \gamma},$$

- The photon energy E is found by minimizing the error in this equation:

$$\mu_{int}(E) - \mu_{fat}(E) = \frac{(D_2 - D_1) \log_e 10}{(h_{int1} - h_{int2}) \gamma},$$

- Knowing E, the constant k can be determined:

$$k = 10^{-D_1} e^{-(\mu_{int}(E) - \mu_{fat}(E)) h_{int1} \gamma}$$

6

Breast Compression

6.1 Introduction

In this chapter we propose a novel way of obtaining information about the internal physical properties and structures of the breast: comparing mammograms performed with the breast compressed to varying thicknesses. For example, a mammogram might be taken with the breast compressed to a thickness of 5 centimetres, followed by a second mammogram with the breast compressed to a thickness of 6 centimetres. The movement and deformation which is seen by comparing these two mammograms is linked to the physical properties of the breast: mammographic signs which do not change position between the two mammograms might be fixed in some manner (eg. by spicules to the chest wall); mammographic signs which appear not to change might represent a solid tissue structure (eg. a malignant tumour).

The results and conclusions explained in this chapter are important not only for diagnosis, but also for image analysis since algorithms must be robust to the degree of compression. This robustness is necessary as the algorithms will be used on mammograms performed by different radiographers, and the degree of compression often varies.

The technique of comparing mammograms performed at different compressions, which we have termed "differential compression mammography", aims to provide reliable information about the physical properties of the deep breast tissues and internal breast structures. This complements the information provided by external physical

examination of the breast which gives information about the physical properties of the breast tissue close to the breast surface. The information gained from differential compression mammography contrasts with that gained from the regular non-invasive techniques of mammography, magnification mammography, ultrasound and breast palpation, and the technique of fine needle aspiration biopsy.

Similar techniques to differential compression mammography are used in other fields to gain information about the internal structure of an object. For example, in order to determine the composition of an object, a materials scientist might apply forces to it and observe how it deforms. Similarly, information about the physical properties of breast tissue might be obtained by observing how the tissue distorts under compression. A comparison of two radiographs is sometimes used in the diagnosis of kidney stones: one is taken of the patient inspiring and a second of the patient expiring. By comparing the position of the calcification relative to the kidney on the two radiographs it is possible to determine whether the calcification is inside the kidney or not. As we shall show, two mammograms of a breast at different compressions can similarly reveal information about the inter-relationship of the internal structures.

This chapter reviews the results of a clinical trial which we have initiated. This trial aims to find whether detection and diagnosis of breast cancer can be aided through comparison of mammograms performed at two different compressions. The chapter starts with a survey of the literature relating to breast compression, and then discusses breast anatomy with a view to predicting what to expect when a breast is compressed. We consider inclusion of the details of breast anatomy vital because too often mammographic images are considered just as images, and domain-independent algorithms applied to them, rather than as projected images of a real, living part of the body. After the predictions, the results from the clinical trial and a detailed discussion of the relevance of the results is presented, before the chapter concludes with comments on both differential compression mammography and the robustness of image analysis algorithms.

6.2 Literature survey

The benefits of breast compression in mammography are well known:

- reduction of motion artifacts by immobilizing the breast
- reduction of geometric blur
- reduction of film density range through having a more uniform breast thickness
- reduction of scattered radiation

- improved separation of tissue structures through increased projected area
- reduction of radiation dose to the breast

A number of authors have commented on radiographic effects of breast compression which they have observed: Roebuck [84] notes how with magnification mammography the tissues can be displaced differently and composite shadows can disappear. Peters et al. [79] note that the apparent size of tension cysts depends on the forcefulness of the compression, and that this information may be useful to differentiate a cyst from a solid mass. They also show an apparent stellate density which disappears in the magnification view. Lamarque [64] notes obliteration of vascular shadows with compression, and argues strongly that radiologists should be aware of the effects of compression and should consider whether mammographic signs have been created or removed by compression.

Little has been published about the effect of compression on the breast itself: Jackson et al. [52] undertook a survey of discomfort felt, correlating the results with the menstrual cycle; Clark et al. [18] measured the pressure applied to the breast during compression; Sullivan et al. [100] measured the force applied and correlated this with perceived discomfort; Fife [30] surveyed the average dimensions of the compressed breast; Eklund [27] discussed the vague terms used to describe breast compression (eg. "appropriate", "adequate"), arguing that compression is an art rather than a science; Yancey et al. [110] explain the difficulty of viewing deep lesions with conventional compression mammography and show how with an adhesive dressing the breast can be stretched out before compression to aid visualisation; Watmough [104] stresses the need for safety limits on the compressive force. Most recently, concern has been expressed that breast compression can cause cancer cells, if present, to spread so that metastasis becomes more likely [105].

A model is helpful in predicting what happens when the breast is compressed. The only model of the breast which has been used in published work deals with thermal modeling of the breast [75], [76]. Models of soft connective tissues [26], [53], [95], skin mechanics [74] and flow induced deformation of soft tissues [6] have been published and these might form the basis of some prediction of how fibrous and adipose tissue might react/deform when the normal breast is compressed, but we are unaware of any work dealing with glandular tissue or neoplasms. However, this biomechanical approach does yield some interesting ideas. As Ryan ([85], private communication) notes, fibrous and adipose tissues in the breast are designed for specific functions, notably to resist gravity and to protect the organ; cancerous and other abnormal tissues within the breast are unlikely also to have such a role, thereby possibly reacting differently to deforming forces.

There is a surprising lack of literature on breast tissues in fields such as breast reconstruction and brassiere design. The only attempt at gaining any quantitative measure of the breast tissue has been in determining the firmness of the breast after reconstruction in order to gain a measure of fibrous capsule formation. These measures have been derived from using calipers [7], [41] and applanation tonometry [69], [40].

6.3 Breast anatomy

To be able to predict the effects of breast compression on the mammogram requires an understanding of basic breast anatomy, figure (6.1). The normal breast consists of glandular tissue with fibrous and adipose tissue in between the lobes and lobules, together with blood vessels, lymph vessels and nerves. The secreting glandular tissue is divided up into 15 to 20 lobes, each lobe containing many hundreds of lobules. These are all connected together by small ducts which further join together close to the nipple to produce the major lactiferous ducts which dilate out into the lactiferous sinuses, narrowing again as they pass through the nipple to form seven or so duct openings.

The breast tissue is enveloped in two layers of fibrous tissue, the deep layer overlying the muscle and the very thin superficial layer beneath the skin. Joining these two layers are fine fibrous ligaments (Cooper's ligaments), which support the breast against the chest. After multiple pregnancies and lactation, or as a result of increasing obesity and age, the Cooper's ligaments become stretched and the breast evolves from firm to pendulous. A small extension of the breast tissue proper commonly wraps round the outer border of the pectoralis major muscle at the upper outer margin of the breast to form the so-called 'axillary' tail, which is a not uncommon site for cancers (hence the use of the 45° medio-lateral view for screening).

After the menopause most of the glandular structures within the breast atrophy and are replaced by fatty tissue. However, many women retain considerable amounts of duct and glandular tissue within the breasts into old age. It has to be recognized, therefore, that the mammary tissue is constantly changing as a result of the normal aging process and as a result of natural physiological alterations during the menstrual cycle, pregnancy and lactation.

6.4 Predicting the effects of breast compression

Using knowledge of the mammographic process, breast anatomy, clinical signs of breast cancer and basic tumour growth some informed predictions can be made about the effect of breast compression on a mammogram. There are six feature characteris-

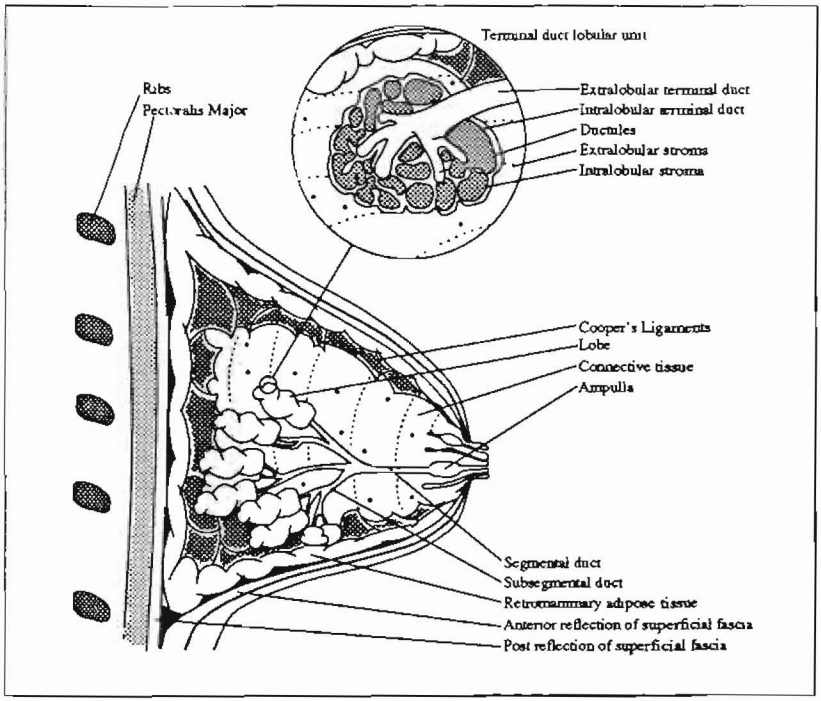

Figure 6.1: Cross-sectional structure of the breast.

tics which the degree of breast compression can affect: shape, size, relative position, absolute position, brightness and edge profile.

Shape is the most robust of the feature characteristics to compression because an object that is partially compressed should project to a similar shape as when it is fully compressed. The only anomaly would be if an object rotated and was projected differently, but this is unlikely to happen with the small differences in compression considered.

The size of the features depends on both the degree of compression and the geometry of the system. The importance of the degree of compression depends upon the type of object represented. For example, a classic clinical sign of breast disease is a lump in the breast. If the lump is soft it is probably benign, and its projected size is likely to increase with compression. The geometry of the system produces a magnifying effect with the magnification increasing if the object is nearer to the source; this will counteract the increase in projected size that derives from greater compression.

The relative position of a feature depends on its relationship and connections with the local tissue. Invasive tumours which have grown into the surrounding tissue are likely to move with the local tissue. Movement of features is confounded by the changing geometry which could amplify or reduce it, whilst further anomalies could arise from the projective nature of mammography.

The absolute position of features relies more on the global breast structure than on the local tissue connections. For example, fibrous strands might hold breast tissue to the chest wall giving little movement, or hold glandular tissue in place (consequently subjecting it to larger deforming forces). Malignant tumours fix themselves to part of the body as they grow, this may be the skin or the muscles of the chest wall, and consequently advanced tumours are unlikely to move far.

Brightness of a feature is the most unreliable characteristic since it can change due to different exposures, tissue properties and shadowing. For example, an object within a fatty breast might be compressed to half its thickness and yet appear equally bright in the mammogram because the exposure has reduced. Another case might have two fibroglandular volumes of tissue projected onto each other and these therefore might be much brighter than when considered individually.

The edge profile is often quoted as a means of distinguishing between benign and malignant lesions. When the breast is compressed, the tissues spread out and the sharpness of edges within the mammogram will change. An obvious case would be a blob of glandular tissue compressed to be very thin and having a much smoother edge profile. The edge profile of a hard lesion only changes because of the imaging conditions and the relative positions of the tissues around it. Edges are further blurred at large breast thicknesses due to the scatter-to-primary ratio increasing.

6.5 Procedure of the clinical trial

Women attending two assessment clinics were asked whether they would volunteer to take part in a trial, in full accordance with ethics committee directives. At no time did any of the women complain of pain; it is unlikely that a woman experiencing pain at screening would consent to extra views at the assessment clinic if offered the choice.

The procedure of the clinic was as normal except that two cranio-caudal view mammograms were taken for each breast. The first mammogram was taken at full (normal) compression, then the compression plate was raised slightly and another mammogram taken. Taking the extra mammogram required an additional 30 seconds and since the positions of the features within the mammograms were to be considered, it was important that the breast did not move significantly in this time. The back edge

of the mammogram (by the chest wall) provides a perfect reference line with which to measure absolute movement.

The decision to take the mammogram at maximum compression first was based purely on practical considerations: the radiographers felt that they could not easily judge when they were close to the maximum compression without actually reaching it, and the woman involved might reasonably be dismayed to learn after the first mammogram, that a second was to be taken with more compression.

The average thickness of the breast was measured by the radiographer marking a piece of card where the compression plate arm with the machine was joined, the exposure in mAs was also noted for each woman. The compression had to be released by an amount large enough to produce differences, while at the same time being small enough to produce a usable quality mammogram. It was found that releasing the compression between 0.5cm and 1cm was satisfactory. It was reported that upon releasing the compression the breast rises to fill the space near the chest wall, but not near the nipple.

When doing any differential study, care must be taken to isolate the effects of the factor being studied from other effects. In this case, the effects of extra compression are confounded with the effects outlined in the previous section. This removes the possibility of directly using the brightness of the areas to see tissue spreading out; if the exposure had been the same one might have expected to see small bright areas representing normal soft tissue disperse into larger but less bright areas.

The pairs of mammograms produced in the trial were studied both as films and on a video, with the mammograms in each pair being alternated quickly; this provides a vivid impression of the movement and deformation which is taking place.

6.6 Results of clinical trial

Figures (6.2) and (6.3) show the mammograms of a breast compressed first to a thickness of around 8cm and then 9cm. They provide an excellent example of the benefits of firm compression. The large dense area has dispersed with extra compression to show a smaller, more rounded shape indicative of a benign lesion. The mammograms show substantial movement of distinguishable features, figure (6.4). Some of the features are readily apparent in each mammogram separately (eg. the coarse calcifications) but others can only be spotted using the motion cues provided by alternating the images in rapid succession. The movement is dramatic considering the small difference in compression recorded. More importantly, the movement of different features shows qualitative differences according to the type of feature. Clearly, the position of a feature

in a mammogram is a function of compression.

Figures (6.5) and (6.6) show the mammograms of a breast compressed first to a thickness of 6cm and then of 6.5cm. The spiculated mass is held to the chest wall and hardly moves whereas the apparent fibrous tissue around it moves appreciably. Figure (6.7) shows the movement of the features. In view of the large movements observed it was conjectured that as the compression was relaxed, the breast tissues were springing back. However, in this example the breast was actually released from the compression between mammograms and then recompressed. Any major shift of the breast position between compressions would be noticeable by comparison of the projected breast edge and total projected breast areas. The large movements explain the difficulty which sometimes occurs when trying to find a specific area of the breast to magnify.

Figures (6.8) and (6.9) show a further example of a breast with a spiculated mass being compressed. However, this time the spicules do not appear to be reaching the chest wall and yet the mass remains almost stationary with more compression. This indicates that the spicules might in fact have been reaching the chest wall. This information could be vital as the clinicians might then decide to remove the whole breast rather than just the localised area.

In every cranio-caudal mammogram studied there was a shift in the projected breast area from the periphery towards the centre as the compression increased. This seems to be due to the skin on the central side of the breast being tighter than on the outside where the breast extends into the armpit. Thus when compression is applied, the breast is skewed inwards by the tight skin. This tightening of the skin is important in creating large deformation forces within the breast. If the breast were simply like a balloon, the tissues within it would move freely rather than deform. In short, the boundary conditions provided by the skin dominate here, as in every elastic deformation problem, and must be taken carefully into account in any biomechanical model.

The differing motion of features over the mammogram, even when they are projected close to each other, might come from them being representative of tissues at different heights within the breast. For example, a superior mass might move far more than an inferior mass, since most of the force is pushing the upper part of the breast down and to the sides (although the mass at the bottom might actually experience more of a deforming force). Indeed, it might be that the view at which to perform two compressions is dictated by the whereabouts of the volume of interest within the breast, since it is desired to bring as large a deforming force as possible upon it.

Figures (6.10) and (6.11) show the mammograms of a breast compressed to a thickness of 5.5cm and then 6.5cm. These appear to show that as the breast is compressed the blood is squeezed out of the visible vessels, possibly due to the vessels contracting with force. This effect was noted in several other cases which were studied and

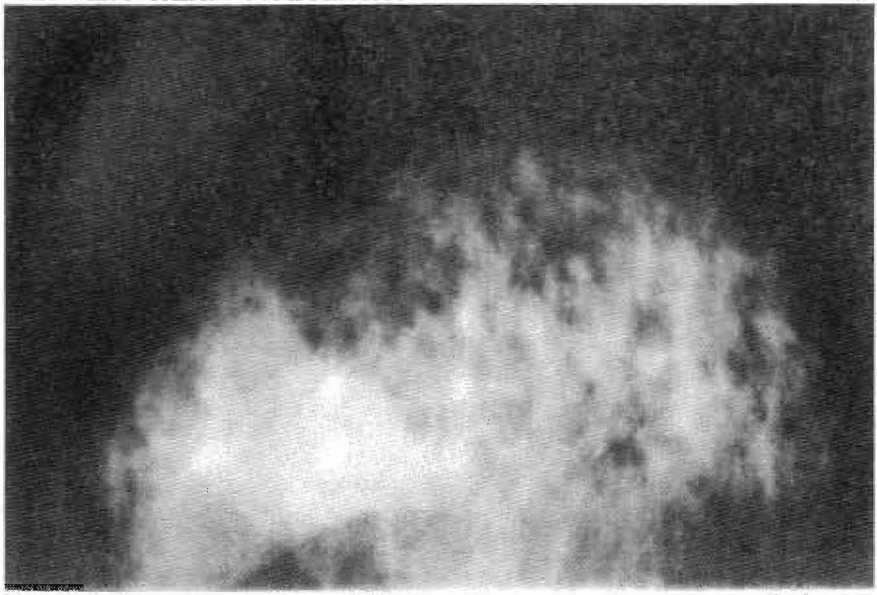

Figure 6.2: Mammogram of breast A. The breast is compressed to an average thickness of 8cm.

Figure 6.3: Mammogram of breast A. The breast is compressed to an average thickness of 9cm. Notice that the large dense area has dispersed with extra compression (above) to show a smaller, more rounded shape indicative of a benign lesion.

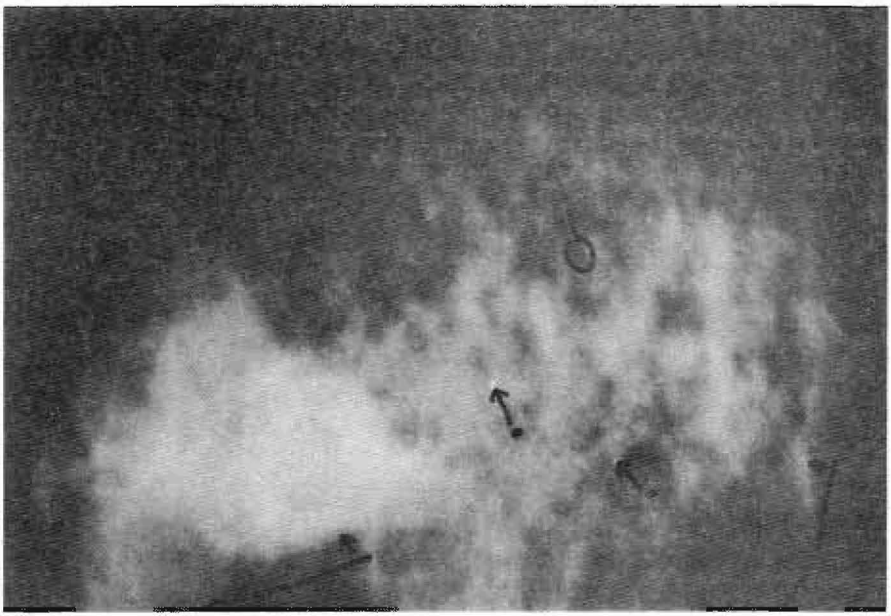

Figure 6.4: This figure shows the movement of some of the distinguishable features in the mammograms of breast A. A distinguishable feature is a recognisable area of the mammogram, for example a coarse calcification. Notice the large distances moved for a relatively small change in compression thickness.

in Lamarque's book [64]. Overall, these mammograms present a strange picture of compression, in which both the mass and the nipple move toward the chest wall with increased compression. However, the breast does get wider as a result of the extra compression (with a more equal thickness of tissue), and some of the vessels on the right side of the mammograms match perfectly at the chest wall.

It is clear from this study that the effects of compression must be considered when correlating mammographic signs with diagnoses. For example, attempts have been made to correlate vessels entering into a mass with malignancy, yet we have demonstrated here an example where vessels are seen going into the mass depending upon the compression used.

Figures (6.12) and (6.13) show medio-lateral oblique mammograms of a breast compressed to thicknesses of 6.5cm and then 7cm. These mammograms show a number of

Figure 6.5: Mammogram of breast B. The breast is compressed to an average thickness of 6cm. In the upper left of the mammogram there is a spiculated mass.

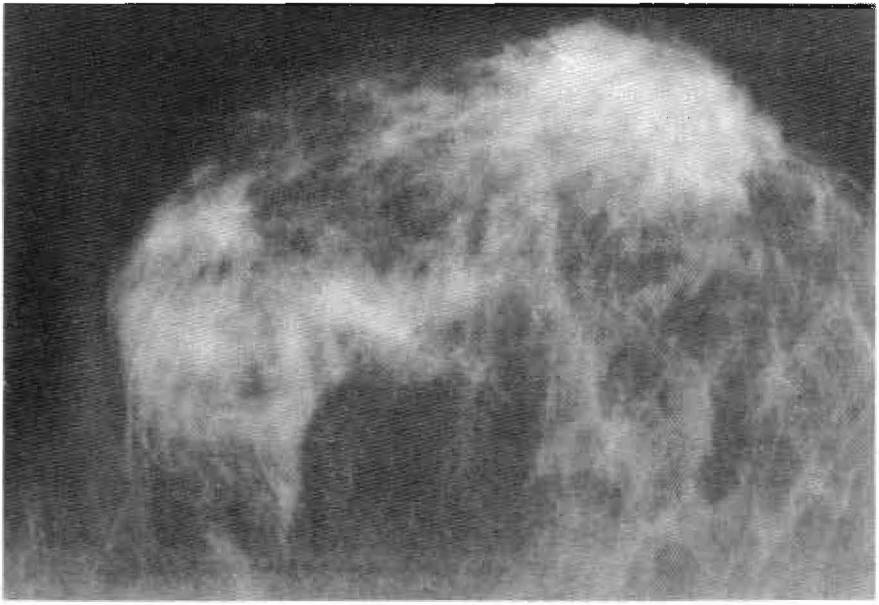

Figure 6.6: Mammogram of breast B. The breast is compressed to an average thickness of 6.5cm. The spiculated mass is held to the chest wall and hardly moves with extra compression, whilst apparent fibrous tissue next to it moves appreciably.

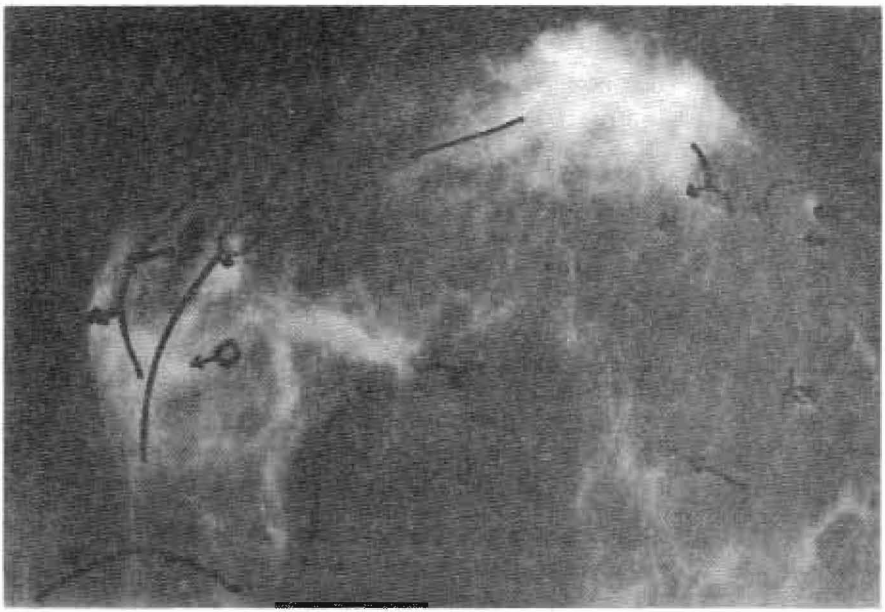

Figure 6.7: This figure shows the movement of the distinguishable features in the mammograms of breast B. Note the movement of the spiculated mass compared to the apparent fibrous tissue adjacent to it.

interesting changes, some of which are immediately evident but some of which require use of the video presentation of motion. On the right side of the mammograms a duct is shown head-on at less compression and then unfurled as if it is being pulled outwards at normal compression. The fat area just above it is also very evidently squashed and presents a larger projected area. On the left hand side some fibroglandular tissue is being forced into another volume of tissue. There is a potential problem with taking two mammograms at different compressions from the medio-lateral oblique view in that the breast is held on a slope so that as the compression is let off the breast is liable to slip, losing the reference line. This did not happen in the case reported here as the friction between breast and compression plate was enough to hold the breast in place.

We again emphasise the use of the video as a compelling way to depict the movement and deformation between the two compressions. Crucially for the radiologist, when the mammograms are viewed they can appear totally different (with few recognisable corresponding features), or identical, and yet when viewed on the video practically

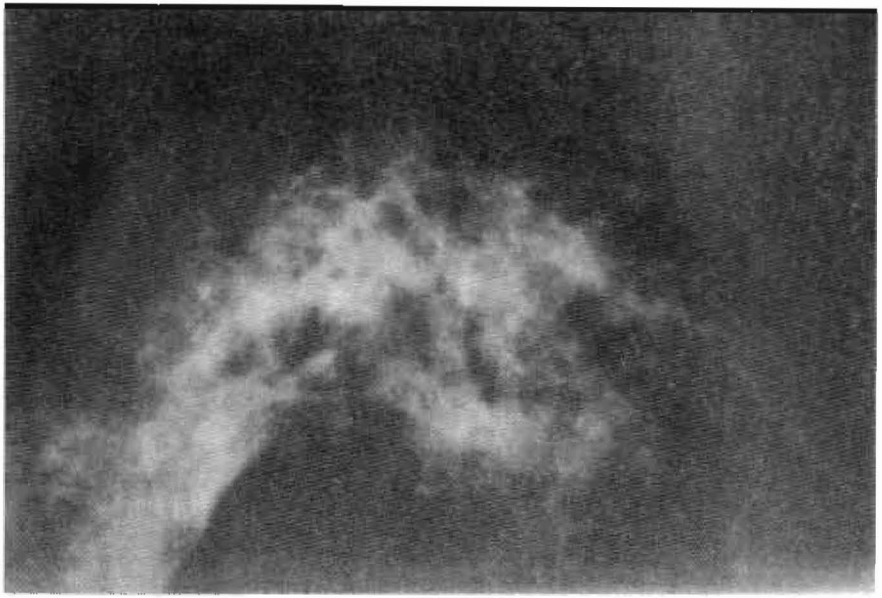

Figure 6.8: Mammogram with breast MML compressed to a thickness of 5.09cm. The reported exposure was 90.0mAs. In the middle left of the mammogram there is a spiculated mass.

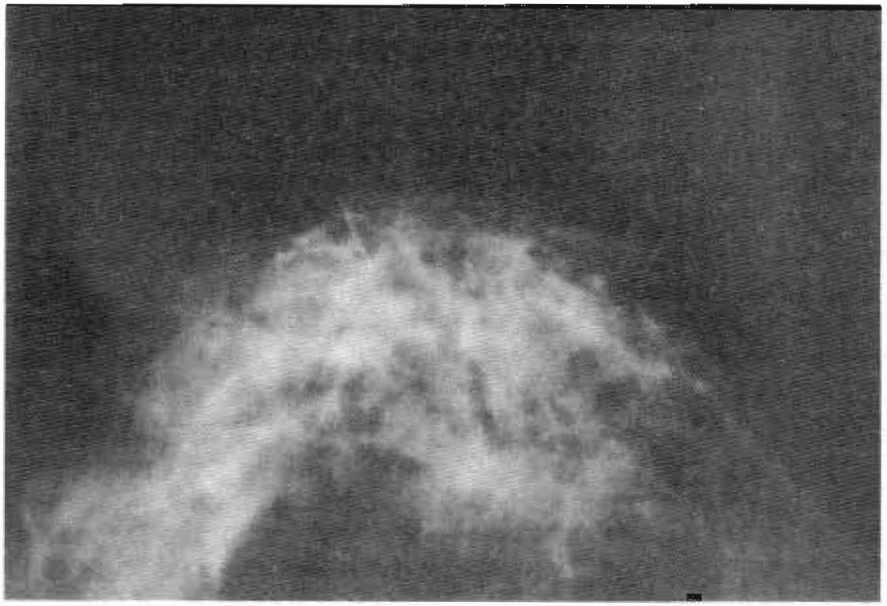

Figure 6.9: Mammogram with breast MML compressed to a thickness of 5.7cm. The reported exposure was 117.0mAs. The spiculated mass hardly moves despite apparently only having short spicules, this might mean that the spicules reach the chest wall.

Figure 6.10: Mammogram with breast FDL compressed to a thickness of 5.5cm, and exposure of 70.5 mAs. There is a suspicious mass present, later found to be benign.

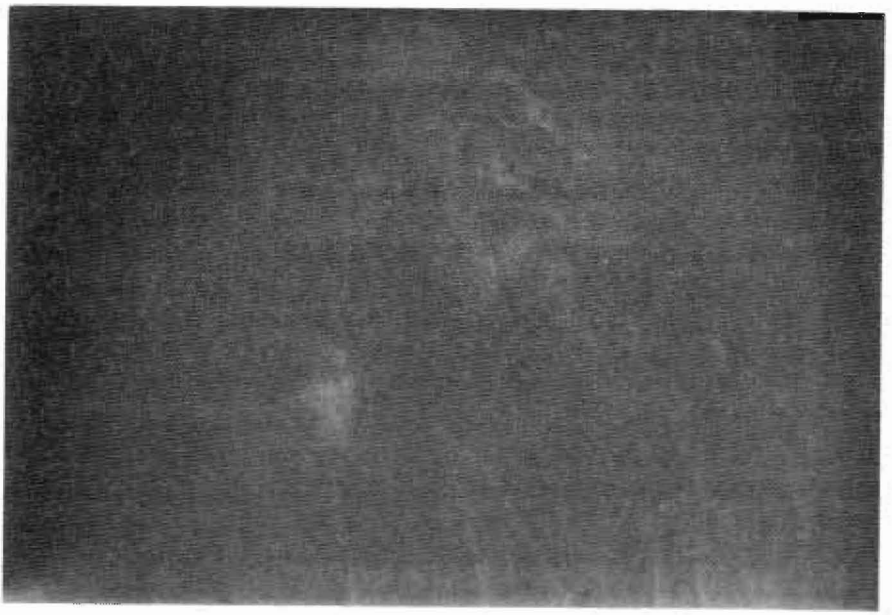

Figure 6.11: Mammogram with breast FDL compressed to a thickness of 6.5cm. The exposure was 92.7 mAs. The blood vessels practically disappear with compression, and the nipple and suspect mass are forced back towards the chest wall; yet the breast is evidently of more equal thickness and has spread sideways.

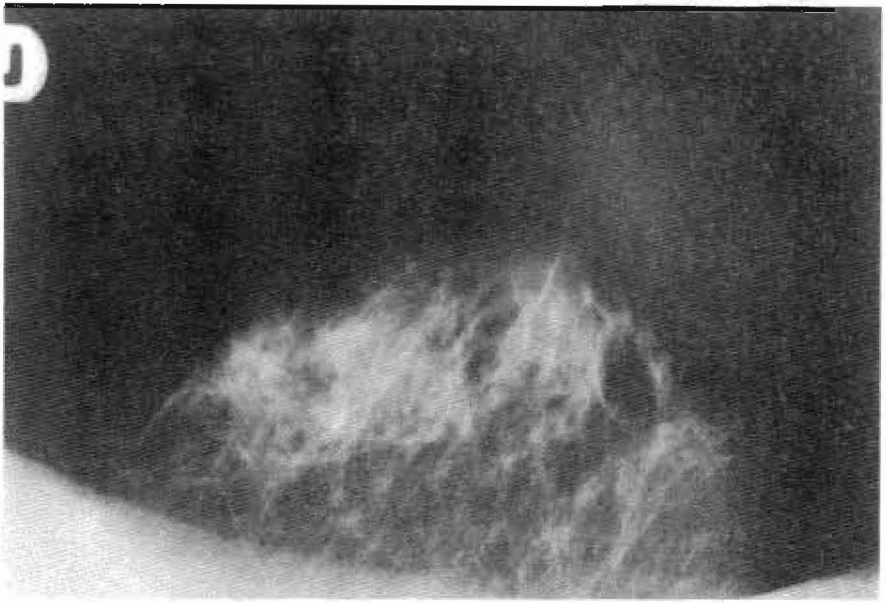

Figure 6.12: Mammogram with breast C compressed to a thickness of 6.5cm.

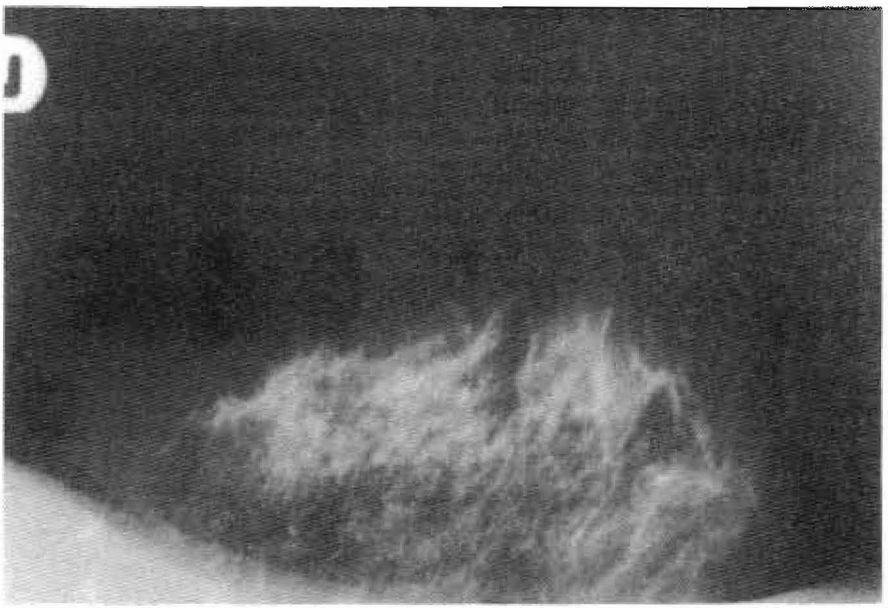

Figure 6.13: Mammogram with breast C compressed to a thickness of 7.0cm. There is a wide range of deformation and movement with the extra compression. Compare the bright spot on the right hand side of the less compressed mammogram, this has seemingly unfurled as if pulled outwards by the compression. On the left, two volumes of fibroglandular tissue seem to be forced into one another.

every point can be seen to shift or deform. This is true even in the mammograms of dense breasts that have been examined. However, although the movement and deformation is easily accessible using this technique, it might well be that experience in it has to be built up. From our experience, each viewing of the video provides further information. Work is underway towards adapting techniques from image processing that can aid the physician interpret this motion by Cerneaz et al. [13].

Our final example shows mammograms of a breast compressed first to a thickness of 5.4cm and then to 6.1cm, figures (6.14) and (6.15). In the middle right area of the mammogram there is a cluster of benign microcalcifications, shown in detail in figures (6.16) and (6.17). The cluster obviously changes formation with compression, and the change cannot be due solely to geometry. These mammograms are also interesting because the microcalcifications are more evident in the mammogram taken with *less* breast compression. This appears to be partly due to the microcalcifications spreading out with more compression.

It is evident from this example that attempts to correlate properties of microcalcification clusters to malignancy (eg. average distance between particles) should also take account of the effects of compression. This is particularly important if the mammograms being used in the study were performed by more than one radiographer, or were from different centres, since it is highly likely that different notions of firm compression will be applied.

Taking a medio-lateral oblique mammogram at less compression at the assessment clinic to compare with the one taken at screening will probably not provide the information given by our technique. This is because if the two mammograms are to be compared properly then they must have a reference line which is in the same position in both of them. Mammograms taken at two different times will probably have lost this reference.

6.7 Discussion of results of clinical trial

These results show that there are large deforming forces present when the breast is compressed. This has many implications, and poses a number of questions.

There is no set standard for the amount of breast compression applied: it is frequently described by the subjective term "firm". However, it seems there is a natural point at which further compression becomes impossible. This point might be when the skin enclosing the breast has been stretched to its maximum. This lack of standards, though understandable, is of concern since the examples presented in this paper have shown differences between mammograms at different compressions, and asymmetry

Figure 6.14: Mammogram with breast GML compressed to a thickness of 5.4cm. The exposure was 76.1 mAs. In the middle right of the mammogram there is a cluster of microcalcifications (enlarged in figure 6.16).

Figure 6.15: Mammogram with breast GML compressed to a thickness of 6.1cm. The exposure was 91.4 mAs. In the middle right of the mammogram there is a cluster of microcalcifications (enlarged in figure 6.17).

Figure 6.16: This is the cluster of microcalcifications from the mammogram of breast GML compressed to 5.4cm.

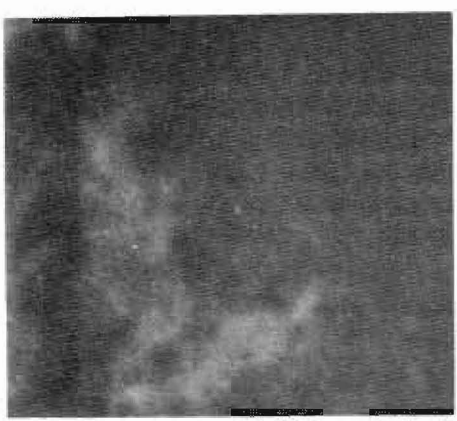

Figure 6.17: This is the cluster of microcalcifications from the mammogram of breast GML compressed to 6.1cm. The change in formation of the cluster is highly significant when statistics such as the average distance between particles are correlated with malignancy. It is also interesting to note the increased visibility of the microcalcifications in the less compressed mammogram, which appears to be due to the microcalcification spreading out with more compression.

between left and right mammograms is often cited as grounds for suspicion.

One aspect of this work which has not been considered is that of symmetry of movement and deformation between left and right breasts. It might well be that just as mammograms of left and right breasts are checked for symmetry, so the movement and deformation should also be in some way symmetrical. This comparison would be useful even if it only involved observing similar occurrences between left and right breasts.

The study of spiculations as a mammographic sign is particularly interesting because of their apparent "function" in holding a mass onto something, be it the local tissue or the chest wall. Similarly, two mammograms depicting a mass moving with a great deal of the local tissue attached to it, or moving relatively independently of the local tissue, might help the radiologist to decide whether a tumour is invasive or is in situ. This kind of observation could be used in deciding how much of the breast should be removed after diagnosis of cancer.

Mammography highlights areas of high absorption within the breast. It follows that if a mass is present small volumes of tissue around the edge of the mass might not show up. However, this does not mean that this tissue is not as firm as the mass itself and we suggest that consideration of the physical properties of the tissue in this way can provide a valid scientific explanation for some well-known observations. For example, Le Borgne's sign can be explained by benign masses having well-defined edges and thus appearing on mammograms in their entirety; whereas invasive malignant masses have grown into the tissue in a non-uniform manner so that although the mass feels large, its radiographic appearance belies this.

There are many signs which might benefit from being studied at different compressions: the "pulling in" or "pushing aside" of the parenchyma; "architectural distortion"; "tethering to the ducts"; "the halo of safety"; and clusters of microcalcifications. The latter can be ambiguous, and though some properties of such clusters are widely accepted as indicating benign or malignant disease, they are still a source of unnecessary biopsies. By studying the response of these clusters to deforming forces (i.e. their overall formation and individual particle sizes and shapes), it might be possible to judge not only whether they are in the lobules or ducts, but also whether the particles have some form of inter-connections (perhaps through central necrosis). It might be possible to distinguish lobules from ducts, since lobule calcifications might change shape with compression, whereas ductal ones do not (perhaps because the ducts are full).

Research into the physical properties of the breast and internal breast structure may well give rise to new designs of compression plates which spread the areas which are usually made up of dense tissue, rather than spreading the whole breast. For example, a rounded top plate might be considered, which pushes the central tissues

of the breast to the sides, giving a decreased thickness in the central area. This kind of plate would have the advantage of not pushing the nipple out, thereby avoiding the possibility that the ducts and glandular tissue which are connected to the nipple are also pulled out actually reducing the projected area of interest and giving a more cluttered mammogram.

Magnification mammography essentially goes some way towards taking mammograms at two different compressions in that radiologists use it to see whether a particular sign disappears with different compression. However, this technique doesn't provide a second image for reference, which can be directly compared to the original. So that, although gross comparisons can be made, detailed specific ones cannot. It might be that taking two mammograms with magnification at different compressions provides a much more detailed and explicit picture of the deformation and movement as well as bringing larger more specific deforming forces to bear. Whilst this form of differential magnification mammography is interesting, extreme care will have to be taken due to the magnification of size and movement from the changing geometry.

The decision to take mammograms at only two different compressions was based solely on ethical grounds. Essentially, compression is a continuously variable parameter that is sampled in this study at two points. We have shown how important the choice of the sample point is, and the additional information made available by a second. Dose irradiation prevents a greater sample set, but it should be taken into account in mathematical models of mammography.

6.8 Conclusions

We have shown that breast compression produces large movement and deformation of tissue within the breast. This implies that there are large forces at work and that some internal breast tissues are deformable. The movement seen is restricted by the internal structures and connections of the breast. We have further shown that taking mammograms at two different compressions is one way of determining the physical properties of the internal breast tissues, and of determining the breast structure. These results are not surprising since the breast is a flexible, deformable part of the body.

The disadvantage of the differential compression technique lies in the additional dosage which comes from needing the extra view, but it is our belief that additional dosage, if justified, is better than biopsy. Other methods exist which are non-ionizing and may provide a better picture of the internal physical properties of the breast and breast structure. Until such methods are developed, differential magnification mammography might provide more detailed information about the physical properties

of the breast and allow large deforming forces to be applied locally.

The work in this chapter has significant consequences for robust image analysis. The clinical trial has produced a number of mammograms which look significantly different from each other and yet are of the same breast. Consider the example which shows the acuteness of the edges of microcalcifications changing with breast compression: setting thresholds for detecting calcifications on the result of an edge detector or local contrast measure will clearly not be reliable on images performed at slightly reduced compression, if the threshold is set on images of firmly compressed breasts.

7

Comparison of Images

7.1 Introduction

In this chapter we study the results of the model-based enhancement algorithms on specific mammographic features, and show the effects of compression on these features. The range of features is restricted due to a lack of data, but some important signs are studied : calcification, a spiculated mass and a benign lesion. For each of these signs we present the specific area of the original image, the image with scatter removed, and the image created by the monoenergetic simulation. We duplicate this for the mammograms performed with less breast compression and also display relevant profiles. The aim of the chapter is to highlight the enhancement and effect of breast compression on specific features.

7.2 Calcifications

Breast GML contains some benign microcalcifications. These calcifications are small, clustered and, most importantly, round. Figure (7.1) shows the calcifications at full and slightly less compression, with the image enhanced by both the weighted scatter algorithm and monoenergetic simulation. The visibility of the calcifications is clearly enhanced by application of the model-based algorithms. It is important to note the change in the image with more compression: the calcifications seem to compress and spread out becoming less visible with edges that are far more blurred. This casts

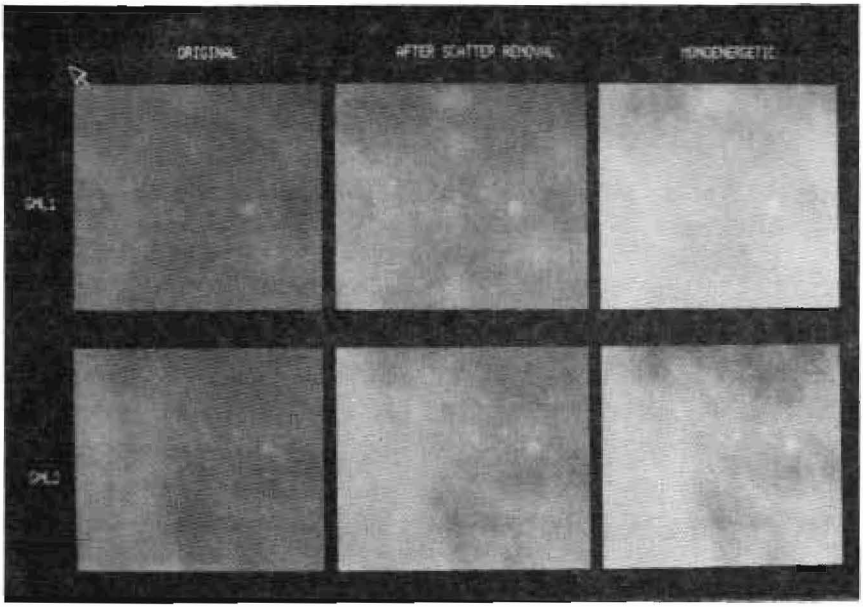

Figure 7.1: Calcifications from the two GML mammographic images. The top row shows the calcifications from the breast at most compression. The image on the left is the original, in the middle is the image with scatter removed, and on the right is the image created by the monoenergetic simulation. Clearly, the calcifications are significantly enhanced by the transforms. Notice also the differences in the calcifications at different compressions; the calcifications in the less compressed breast are more round, and have sharper edges.

doubt on whether image analysis algorithms using edge detection to predict, or edge sharpness to classify, calcifications will work reliably. Shape may be a more reliable measure, but the calcifications in the less compressed breast appear more distinctly round than those at most compression.

The differences in the images can be seen by taking a profile across them. Figure (7.2) shows such a profile taken across the top set of images. The enhanced images are clearly sharper and thus should be easier to detect the calcifications in. Certainly, a morphological operator would pick out the calcifications better in the enhanced images.

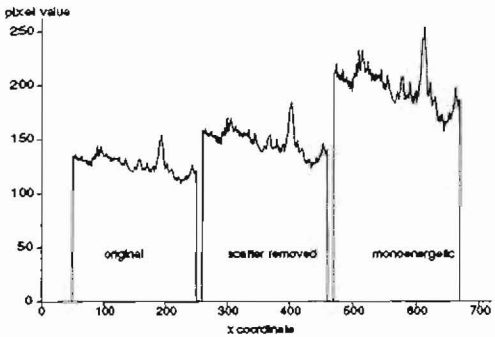

Figure 7.2: This is a profile across the top set of images shown in figure (7.1), the high peak towards the right of each individual profile is a calcification.

7.3 Spiculated mass

Figure (7.3) shows an image of a spiculated mass with less compression and enhancement. The mass is evidently better differentiable in the enhanced images and fine spiculation is better perceived, as well as the centre of the mass becoming more obvious. A profile across the image is shown in figure (7.4). The higher contrast in the enhanced images means that a check for spiculations (high contrast linear structures) should be more successful. Similarly, even classic template matching that attempts to detect the centre of the mass should be more successful and reliable on the enhanced image. In this example, maximum compression is clearly useful in aiding visibility of the lesion.

7.4 Benign lesion

Figure (7.5) shows an image of a suspect mass with less compression and enhancement. After ultrasound, the radiologist diagnosed this mass as benign. The original image is unclear in that the mass merges smoothly into the background, but this impression is not given in the enhanced images where the mass stands distinct from the background. Figure (7.6) shows a profile across the top set of images. Looking at the changes in this image and profile, it is hard to imagine reliable edge blur measurements without removal of the imaging parameters. Figure (7.7) shows a profile across the bottom set of images (i.e. images performed with less breast compression). The edges of the lesion

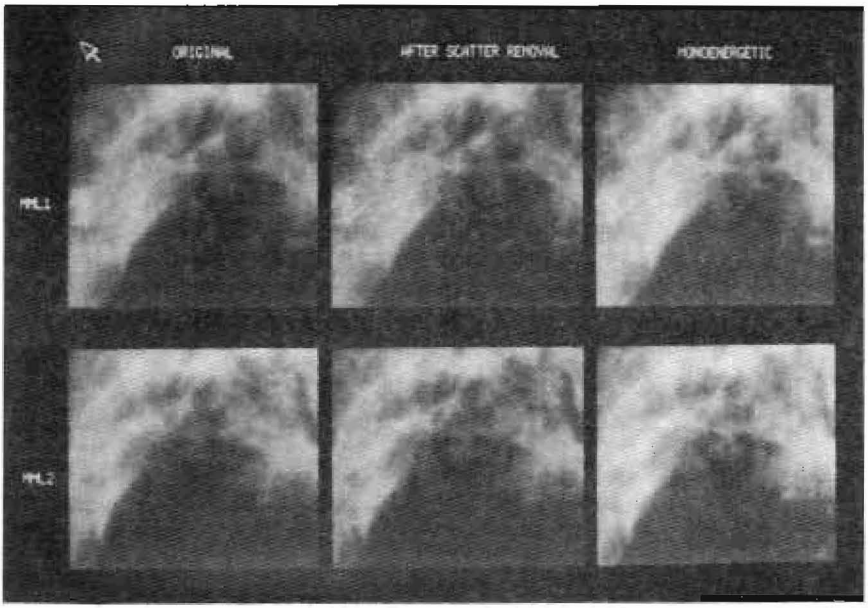

Figure 7.3: Breast MML has a spiculated mass situated in the middle left. This image has the mass in close-up showing the enhancement when the scatter removal and monoenergetic algorithms are run. The centre of the mass becomes far more visible with enhancement, and with extra compression. Detection of spicules should be a good deal easier in the sharper, enhanced images.

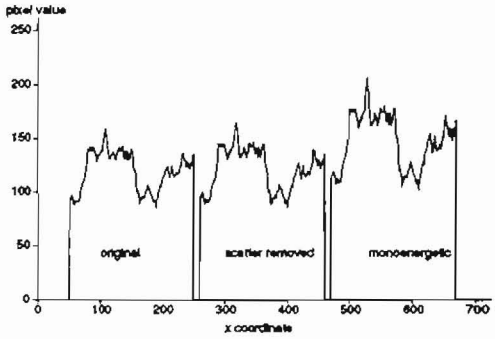

Figure 7.4: This is a profile across the top set of images shown in figure (7.3)

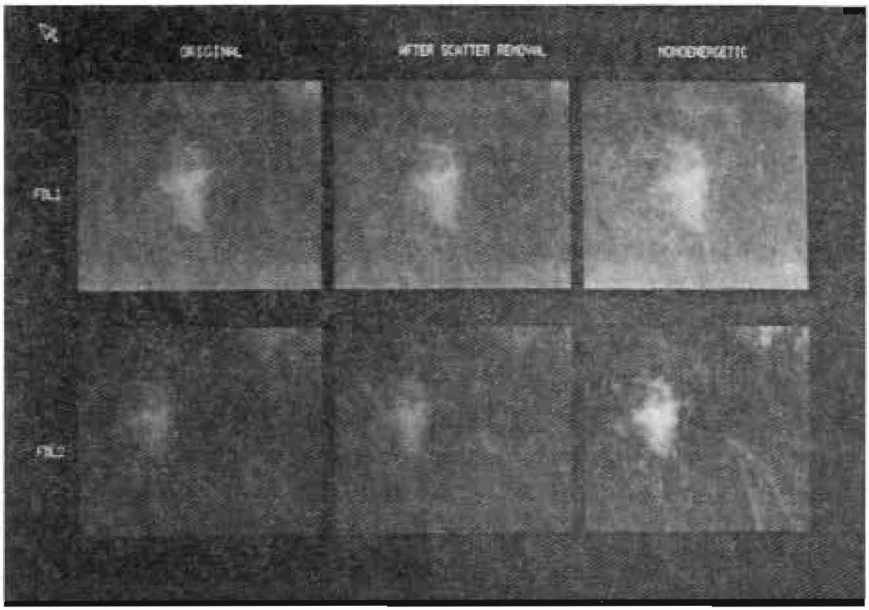

Figure 7.5: Breast FDL has a benign mass in, probably a cyst. The original image gives the impression that the mass merges smoothly into the background, with enhancement the mass stands out from the background giving a more benign appearance.

at less compression are much better defined, and therefore more benign, in the less compressed image. These profiles cast doubt on the robustness to breast compression of edge profiles. In view of there profiles, it would be interesting to examine the edge profile of a malignant mass with varying compression. Unfortunately, the only example we have at present is of a spiculated mass in which the edge profile is only important with a view to detection of the spicules.

7.5 Image analysis

The goal of the work in this thesis has been image enhancement. To achieve this we have taken a model-based approach which lends itself perfectly to preprocessing of the images before analysis in order to remove the imaging variations. Furthermore, the thesis contains some ideas on the effects likely to occur with different breast compres-

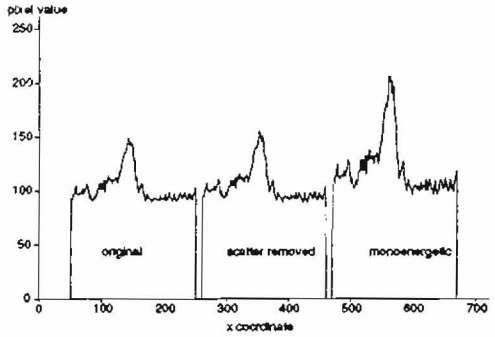

Figure 7.6: This is a profile across the top set of images shown in figure (7.5)

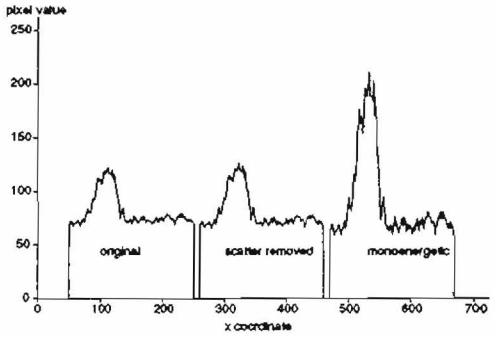

Figure 7.7: This is a profile across the bottom set of images shown in figure (7.5). Comparing this profile with that in figure (7.6) shows the effect of compression on the lesion edge blur. At less compression (i.e. in this profile) the lesion has much better defined edges.

sions. On the basis of our work, the stage is now set for using pattern, morphology and shape analysis to automate screening.

8

Conclusions and Further Work

8.1 Conclusions

In this thesis we have developed a model of the mammographic process with which it is possible to represent, and subsequently remove, the effects of the major factors which degrade mammographic images. Removal of these effects enhances the images and makes diagnosis more reliable and robust manner. To our knowledge this is the first model of the mammographic process (including the breast) which has been developed for enhancement of mammographic images. Consequently, this is the first research in which the spatial varying incident radiation intensity, breast thickness and exposure have been measured and used as an integral part of the processing. More importantly, we have developed the first model of scattered radiation in mammography and shown how to apply it to remove the effects of scatter by software.

The degrading effects studied in this thesis are scattered radiation, spatially varying incident radiation intensity, beam hardening and poor positioning of the automatic exposure control. Removal of the effects of scatter is a local high-pass filtering operation. This ensures that clinically significant information, such as calcification or spiculation, is preserved. Compensation for the spatially varying incident radiation intensity results in an image that is darker towards the nipple and accounts for the radiation intensity decay due to the diverging beam. Ultimately this allows calculation of a quantitative breast measure (the thickness of interesting tissue) for small volumes of breast tissue. Using the quantitative breast measures it is possible to simulate a scatter-free mammographic examination with a monoenergetic x-ray beam, thus overcoming

the loss of contrast in dense tissue due to beam hardening. Such an examination allows the introduction of more or less contrast depending upon the photon energy selected (the energies used normally in mammography are the result of a compromise between image quality and radiation dose to the breast - a compromise which we don't need to make). The signals which result from the simulation of the monoenergetic examination and scatter removal both require amplification before theoretical exposure to the film. To achieve this, the automatic exposure control is modeled and the signal is amplified to get an average film density over a control area. The automatic exposure control model also allows transformation of the original images to simulate different exposures, or different control unit positions.

As part of the development of the weighted scatter model, it was shown how the anti-scatter grid makes the scatter component of a higher frequency but lower amplitude. This occurs because of the way the grid functions to remove photons incident at unexpected angles (relative to the source). To do this without removing too much of the primary signal, the grid has to let through photons coming from a range of angles and therefore lets through scattered photons which have come from nearby locations. Thus the scatter component relies more on the nearby tissues. This observation has the important consequence that the scatter component can be more easily removed digitally when a grid is not used and the scatter is of a lower frequency. Removing the scatter digitally without a grid could reduce the radiation dose to the breast by a factor of two.

At each step in the development of the models presented in this thesis, the approximations and assumptions were stated. The error associated with some of these is extremely difficult to assess, so we verified the final results as comprehensively as possible. The verification tests took the form of comparing the thickness of "interesting tissue", with the values one might expect. The tests were both objective (e.g. comparing $h_{i,m}$ to measured breast thickness), and subjective (e.g. comparing the percentage of interesting tissue in the breast to how the mammogram appears to a trained radiologist). In all the example mammographic images to which the algorithm has been applied, the verification tests have been passed exceptionally well.

As well as model-based image enhancement, part of the work in this thesis (chapter 6) investigated the effects of the most neglected aspect of mammography: breast compression. The investigation took the form of comparing mammograms taken at different degrees of compression with a view to using the distortion and movement as a means of aiding diagnosis. We dubbed this novel technique "differential compression mammography". We discovered that small differences in compression produced large changes in the mammogram. The scale of the changes observed augurs well for the use of the technique as a diagnostic aid in difficult situations, although further investigation is necessary. There are two problems with applying the technique in practice:

the extra radiation dose to the breast and the probable necessity of using electronic equipment (such as video) to view the motion cues. Using electronic equipment will not be a problem once mammography becomes digital.

The results presented in chapter 6 are a cause for substantial concern about the robustness to compression of standard image analysis algorithms, and the reliability of so-called objective measures calculated by computer. For example, a pair of mammograms was shown where microcalcifications were actually harder to detect in the most compressed mammogram because the calcium seemed to squash, leading to a more blurred image. Other examples showed lesions that were far easier to see in the most compressed mammograms. Clearly, image processing is not going to be reliable if the degree of breast compression varies, as it reported to do between radiographers.

In conclusion, model-based image processing is a promising, indeed necessary, approach to take in safety-critical applications such as mammography. The cost of creating artifacts or removing important signs could be devastating to the woman involved. Mammography is well suited to model-based enhancement because it is a complex process with several degrading factors, although this very complexity makes any model approximate. It remains to be seen if image analysis algorithms can handle robustly differences in the degree of breast compression, but the results presented in this thesis indicate that this will not be easy.

8.2 Further Work

8.2.1 Extending model to other views and systems

The work in this thesis has dealt exclusively with mammograms performed from the cranio-caudal viewpoint on a GE Senographe mammographic system. Extending some parts of the work to other views and other mammographic systems is not trivial. There are two major problems: segmentation of the pectoral muscle and availability of component performance data.

Proper segmentation of the breast area from the pectoral muscle is crucial in work which requires finding minimum or maximum values within the breast area. Segmentation is therefore needed for the constant scatter algorithm and the automation of choice of photon energy for the monoenergetic simulation. The weighted scatter removal algorithm is not affected since an approximation can be made to the scatter entering the breast area from the muscle, i.e. zero.

The pectoral muscle is also the site of the lowest film densities and is where the linear approximation to the characteristic curve of the film-screen combination fails

significantly. Although this doesn't affect any of the algorithms presented in this thesis (the characteristic curve is just an imaging parameter), it does affect the analysis of the algorithms, and another analytical approximation will be necessary to aid understanding.

The differences between the pectoral muscle area and the rest of the mammogram mean that different image enhancement techniques should be applied to each area. For example, since the pectoral muscle is much more dense that the breast area it might be appropriate to have different exposures to the different areas. This could be achieved by segmentation and the placement of two theoretical automatic exposure controls: one under the breast, and the other under the muscle.

The availability of component performance data was a problem with the work in this thesis. For example, with the intensifying screen data from a Kodak screen was used rather than from a Fuji screen. The data for the anti-scatter grid, and x-ray tube on other systems should be similar to those used in this thesis since the equipment is standard (at least across the UK).

8.2.2 Improving the model and other degrading effects

The model of the mammographic process derived in this thesis contains many approximations and assumptions, and is therefore inherently improvable. Is it worth improving it further given that it passed the verification tests in chapter 5 so well? The answer is that some parts are probably worth more effort, while others aren't; particularly since the future of mammography is digital. For example, accounting for film reciprocity law failure and the calibration of the film-screen combination are probably not worth improving, however it might well be worth studying the shape of the breast edge.

8.2.3 Modeling other degrading effects

The model could be extended to cover effects such as glare and the blurring due to system geometry as they allow further safe sharpening of the images and will be present in digital mammography. Modeling such effects requires detailed consideration of the action of the intensifying screen, and the degree of blur created by photons of different energies.

One potential degrading factor not directly relevant to our work is the degradation which occurs to the mammographic film with age. By the time that mammography becomes digital there will be literally millions of films stored in the UK alone which

will require digitizing. As the films age they become lighter, and after a time significant degradation can occur. This degradation could well be modeled using empirical data. It seems likely that such images could be restored simply by re-exposing the film using our automatic exposure control model.

8.2.4 Modeling xeroradiography

Attainment of an objective measure of the breast tissue (i.e. thickness of interesting tissue) enables further modeling such as performing xeroradiography theoretically. Xeroradiography is a technique which provides high contrast for subtle tissue differences and is widely appreciated by radiologists (especially for dense breasts). However, it is of a lower resolution and, crucially in practice, gives a much higher radiation dose than conventional screen-film mammography. The problem in modeling xeroradiography is in obtaining the data for the various parts of the system as most physicists appear to have worked only on the low-dose screen-film technique.

8.2.5 Optimizing the monoenergetic simulation

Chapter 5 presented a monoenergetic simulation and explained how the choice of photon energy might be automated. The automation was based upon making the average thickness of interesting tissue map to a film density of 1.5, and making the maximum thickness of interesting tissue map to a film density of 0.6. These pairs of values were chosen by experience, and might not be optimal. It might be better to map the average thickness of interesting tissue above the automatic exposure control to a film density of 1.5, but this opens up the question of optimal placement of the control unit itself.

8.2.6 Optimal placement of the automatic exposure control

The automatic exposure control is usually placed towards the back of the chest wall, without any consideration of previous mammograms. In practice, this placement has been found to be effective, but it is not perfect and retakes are common. Instead of taking the average over an area, the automatic exposure control could duplicate our theoretical method of averaging over the entire breast. The problem with this is that at the edge of the breast the thickness of interesting tissue falls rapidly and this reduces the average over the whole breast significantly, making it unsuitable to use. Further consideration should be given to the optimal exposure, with perhaps a model of what the viewer perceives.

8.2.7 Digital scatter removal without an anti-scatter grid

The results in chapter 5 suggest that the effects of scattered radiation can be removed digitally without an anti-scatter grid. If this is true, then it might be possible to halve the present dose to the breast, and still present a satisfactory image.

The first attempt at investigating this might well involve performing a mammogram on an intricate phantom without an anti-scatter grid, and then modeling the scatter and removing it in a similar fashion to the weighted scatter algorithm. The result could then be compared to the mammogram actually attained when a grid is used.

8.2.8 Mammography workstation

The mammographic model developed in this thesis allows simulation of a monoenergetic x-ray beam for any photon energy, and adjustment of the automatic exposure control setting. Equally, the characteristic curve of the film-screen combination could be adjusted. These possibilities suggest that a workstation might be provided for the radiologist with the appropriate settings displayed and manipulable (e.g. exposure in mAs). Such a workstation would allow a radiographer to use her experience with the practical system to enhance the images prior to the radiologist viewing them. Alternatively, the radiologist might prefer to have automatic digital filtering applied before viewing: filtering based on model-based techniques where she/he understands the implications. Of course, similar enhancement would have to be performed on both left and right mammograms so as not to introduce asymmetry, and that could be a research topic all in itself.

8.2.9 Image enhancement to show interval cancers

Diagnosis of breast cancer is by no means faultless, and a number of cancers are missed by the people involved in the screening programme. These cancers are termed interval cancers because they appear between calls to screening. Application of image enhancement to the original screening mammograms to highlight the original signs (if any) could be a powerful way of convincing radiologists of the benefits of image processing.

8.2.10 Sorting mammograms into easy and difficult to diagnose

The percentage of the volume of interesting tissue to the volume of the breast appears to a reliable measure of the breasts appearance (chapter 5). High percentages mean

that the breast is dense and that the mammograms tend to be difficult to diagnose from. Low percentages mean that the breast is mainly fat and the mammograms tend to be easy to diagnose from. Further testing is needed to establish if the radiologist's difficulty in diagnosing is linked to the percentage of interesting tissue, or if other factors such as texture are important.

8.2.11 Image analysis

Image analysis algorithms must be robust not only to different imaging conditions, but also to different degrees of breast compression. Robustness is especially difficult to obtain with mammographic images because of the different equipment in use across the country and the non-standard amount of breast compression applied. For example, the robustness of an image analysis algorithm to the degree of breast compression can be determined by running the algorithms on the images produced by the clinical trial which we initiated (chapter 6). The outcome is likely to be surprising bearing in mind the results presented there.

The best way to test the robustness of analysis algorithms to different imaging conditions is to simulate the effects on the mammogram of the different conditions. In this way, the same breast image is used and the results will be comparable. The work presented in this thesis allows simulation of the effects of different imaging conditions. It might also be possible to simulate a mammogram performed without an anti-scatter grid so that the robustness to scatter can be judged. One of the most interesting tests would be to examine the variation in the performance of analysis algorithms on images compensated for the spatially varying incident radiation intensity.

As well as testing for robustness, the algorithms proposed in this thesis should also allow more robust algorithms to be developed by enabling the removal of the imaging parameters and the effects of scattered radiation before analysis. This opens up the question of what image should the computer be given to work on? If the image is to be the same as that received by a human, then the film density image acquired will have to be transformed prior to analysis into a "transmitted light" image. The idea could be taken further to give the computer an image to work on which is similar to that perceived by a human. However, doing this means presenting the computer with images that have imaging parameters still in, and whereas humans can automatically adjust, the computer cannot. Thus the computer should work more robustly with images which have the imaging parameters removed.

Certain feature characteristics depend not only on the imaging conditions but also on the thickness of the breast. For example, a 2cm cube of cancerous tissue might appear more distinct in a breast of height 6cm than in a breast of height 8cm. Similarly,

the degree of blur of an edge will be affected by the breast thickness due to, amongst other factors, scattered radiation. These facts argue for mapping the breast image to be as if it were of a standard thickness before image analysis. Using our notion of interesting tissue it is certainly feasible to map the breast to a new thickness by keeping the percentage of interesting tissue the same. However, before performing any mapping careful consideration has to be given to the relationship between the spatial extent of a feature and its brightness. This has to be considered because it is possible that a radiologist judges in some way the thickness of an object on the basis of its brightness. The idea of mapping to a standard breast thickness is certainly feasible since tumour size is probably independent of breast size.

8.2.12 Objective measures

There is much interest in making the computer an objective measurer of mammographic signs such as edge blur, degree of spicularity and parenchymal pattern. To make these measurements truly objective the imaging process must be taken into account and variations removed. It is pointless trying to measure something if part of the measuring process itself is varying. Use of a model to remove the imaging variations is, as noted above, probably similar to the way a radiologist automatically adjusts to take into account the imaging variations. Again though, breast compression will have to be carefully considered.

8.2.13 Breast compression

In chapter 6, the technique of differential compression mammography was explained. The main argument against this becoming a standard technique is the extra radiation dose to the breast involved. It could be argued that some of the same information is available when a magnification view is performed. When the magnification view is performed the breast is compressed differently from normal and only a reduced volume of the breast is imaged. The magnified view cannot be compared to the original to determine relative position changes or tissue spreading because of the magnification involved. However, it is possible to model the geometry involved in the magnification view and it should therefore be feasible to transform the image to make it comparable to the normal mammogram. In this way relative positions can be compared and tissue spreading assessed without the extra radiation dose to the breast (although the absolute positions will be lost).

The profiles across specific features under different compressions which were presented in chapter 7 suggest that the edge profiles of benign lesions change greatly with

compression. It might be that edge profile is one of the most significant and reliable characteristics to observe under compression.

Another interesting idea which arose whilst the different kinds of breast tissue were studied was based on an analogy with rubber: if you extend rubber it gets hotter, by manipulation of the breast could heat be generated internally and thermography used to pick up the different areas? The idea is that elastic tissues will store heat, but hard tissues will not.

A model would be helpful in predicting the changes in a mammogram when the breast is compressed. As pointed out in chapter 6, very little work has been done on modeling the breast and this is due in part to the great variance in proportions of different tissue types between the different breasts. The major reason however is the lack of knowledge of what to expect when any tissue is compressed. Using the work in this thesis the mammographic side of the problem can be solved. That is, knowing the constituents of the breast and positions, a mammographic image can be created which duplicates what would be seen in practice. If a model of the physical properties of the breast can be developed it would be possible to experiment theoretically with differential compression mammography.

A

Glossary

To a non-medic the medical world is full of undecipherable terms. However, most of the words have quite precise meanings and are formed in specific ways. For instance, benign tumours are described by adding the suffix -oma to the name of the tissue from which they originate. An example of a benign connective tissue tumour would be a fibroadenoma, arising from the fibrous tissues.

Cancers of connective tissues are indicated by the suffix 'sarcoma', thus, for example, a malignant tumour of fibrous tissue is known as fibrosarcoma. Cancers of epithelial or glandular tissue are indicated by the suffix 'carcinoma' and therefore the commonest cancer arising from the cells lining the ducts of breast tissue is known as adenocarcinoma.

The following is a list of words used in this thesis and other related ones, with their meanings. All the definitions are reproduced from the *Pocket Dictionary for Nurses*, published by Oxford University Press [103]:

Acinus n. a small sac or cavity surrounded by the secretory cells of a gland.
Aden- (adeno-) prefix denoting a gland or glands.
Adenocarcinoma n. a malignant epithelial tumour arising from glandular tissue. The term is also applied to tumours showing a glandular growth pattern.
Adenoma n. a benign tumour of epithelial origin that is derived from glandular tissue or exhibits clearly defined glandular structures. Adenomas may become malignant (see adenocarcinoma).

Adenosis n. 1. excessive growth or development of glands. 2. any disease of a gland, especially of a lymph gland (node).
Adipose tissue n. fibrous connective tissue packed with masses of fat cells. It forms a thick layer under the skin.
Aetiology n. (etiology) the study or science of the causes of disease.
Anastomosis n. an artificial connection between two tubular organs or parts.
Angiosarcoma n. a sarcoma arising in the blood vessels.
Anterior adj. describing the front part of any organ.
Apocrine adj. 1. describing sweat glands that occur only in hairy parts of the body, especially the armpit and groin. 2. describing a type of gland that loses part of its protoplasm when secreting.
Areola n. the brownish or pink ring of tissue surrounding the nipple of the breast.
Atrophy n. the wasting away of a normally developed organ or tissue due to degeneration of cells.
Asymptomatic adj. not showing any symptoms of disease, whether disease is present or not.
Axilla n. the armpit.

Benign adj. describing a tumour that is not cancerous.

Calcification n. the deposition of calcuim salts in tissue.
Carcinoma n. any cancer that arises in epithelium, the tissue that lines the skin and internal organs of the body.
Caudal adj. relating to the lower part or tail end of the body.
Collagen n. a protein that is the principal constituent of white fibrous connective tissue (as occurs in tendons).
Congenital adj. describing a condition that is recognized at birth or that is believed to have been present since birth.
Costal adj. of or relating to the ribs. c. cartilage, a cartilage that connects a rib to the breastbone (sternum).
Cranio prefix denoting the skull.
Cyst n. an abnormal sac or closed cavity lined with epithelium and filled with liquid or semisolid matter.
Cystic mastitis n. chronic mastitis in which the breast feels lumpy due to the presence of cysts.
Cytology n. the study of the structure and function of cells.
Cytoplasm n. the jelly-like substance that surrounds the nucleus of a cell.

Duct n. a tubelike structure or channel, especially one for carrying glandular secretions.
Dysplasia n. abnormal development of skin, bone, or other tissues.

Ectasia n. the dilation of a tube, duct or hollow organ.
Eczema n. a superficial inflammation of the skin. Eczema causes itching, with a red rash often accompanied by small blisters that weep and become crusted.
Endocrine gland n. a gland that manufactures one or more hormones and secretes them directly into the bloodstream (and not through a duct to the exterior).
Epithelium n. the tissue that covers the external structure of the body and lines hollow structures (except blood and lymphatic vessels). Epithelium may be either simple, consisting of a single layer of cells; stratified, consisting of several layers; or pseudostratified, in which the cells appear to be arranged in layers but in fact share a common basement membrane.
Erythema n. abnormal flushing of the skin caused by dilation of the blood capillaries.
Etiology n. (aetiology) the study or science of the causes of disease.
Eversion n. a turning outward.

Fibre n. a threadlike structure, such as a muscle cell or nerve.
Fibrocyst n. a benign tumour of fibrous connective tissue containing cystic spaces.
Fibrosis n. thickening and scarring of connective tissue, most often a consequence of inflammation or injury.

Gland n. an organ or group of cells that is specialized for synthesizing and secreting certain fluids, whether for use in the body or for excretion.

Haematoma n. an accumulation of blood within the tissues that clots to form a solid swelling.
Histiocyte n. a fixed macrophage, i.e. one that is stationary within connective tissue.
Histiocytoma n. a tumour that contains macrophages or histiocytes.
Hyalin n. a clear glassy material produced as the result of degeneration in certain tissues, particularly connective tissue and epithelial cells.
Hyperplasia n. the increased production and growth of normal cells in a tissue or organ.
Hypertrophy n. increase in the size of a tissue or organ brought about by the enlargement of its cells rather than by cell multiplication.

In situ adj. describing a cancer that has not undergone metastasis to invade surrounding tissue.
Invasion n. the destruction of healthy tissue by a malignant tumour.
Involution n. atrophy of an organ in old age.

Lactiferous adj. transporting or secreting milk.
Lesion n. a zone of tissue with impaired function as a result of damage or wounding.

Lipoma n. a common benign tumour composed of well-differentiated fat cells.
Liposarcoma n. a malignant tumour of fat cells.
Lobe n. a major division of an organ or part of an organ, especially one having a rounded form and often separated from other lobes by fissures or bands of connective tissue.
Lumen n. the space within a tubular or saclike part.
Lymph n. the fluid present within the vessels of the lymphatic system, which is derived from the fluid that bathes the tissues. Lymph is similar in composition to plasma, but contains less protein and some cells, mainly lymphocytes.
Lymph node n. one of a number of small swellings found at intervals along the lymphatic system. Groups of nodes occur in the groin and armpit, and other parts. They act as filters for the lymph and produce lymphocytes.
Lymphatic system n. a network of vessels that conveys electrolytes, water, proteins, etc. - from the tissue fluids to the bloodstream. Lymph passes through fine capillaries into the lymphatic vessels, which have valves to prevent backflow of lymph. The lymphatics lead to two large channels - the thoracic duct and the right lymphatic duct - which return the lymph to the bloodstream via the innominate veins.
Lymphocyte n. a variety of white blood cell. They are involved in immunity and can be subdivided into B-lymphocytes, which produce antibodies, and T-lymphocytes, which are involved in graft rejection etc.

Macrophages n. a large scavenger cell present in connective tissue, and many major organs and tissues.
Malignant adj. describing a tumour that invades and destroys the tissue in which it originates and can spread to other sites in the body.
Mammography n. the making of X-ray or infra-red ray photographs of the breast.
Mastectomy n. surgical removal of a breast. *Radical mastectomy* surgical removal of the breast itself, the lymph nodes in the nearest armpit, and the muscles linking the upper part of the chest with the shoulder, to combat cancer.
Mastalgia n. a pain in the breast.
Mastitis n. inflammation of the breast, usually caused by bacterial infection through damaged nipples.
Median adj. situated in or towards the place that divides the body into right and left halves.
Menarche n. the start of the menstrual periods (usually 10-17 years).
Menopause n. the time in a woman's life when ovulation and menstruation cease and the woman is no longer able to bear children. The menopause can occur at any age between the middle thirties and the late fifties; it is associated with a change in the balance of sex hormones in the body, which sometimes leads to hot flushes, palpitations, and emotional disturbances.
Menstrual cycle n. the periodic sequence of events in sexually mature nonpregnant

women by which an egg cell (ovum) is released from a follicle in the ovary at four-weekly intervals until the menopause.

Metaplasia n. an abnormal change in the nature of a tissue.

Metastasis n. the distant spread of disease, especially a malignant tumour, from its site of origin. This occurs by three main routes: 1. through the bloodstream; 2. through the lymphatic system; 3. across body cavities.

Mitosis n. a type of cell division in which a single cell produces two genetically identical daughter cells. It is the way in which new body cells are produced for both growth and repair.

Myo- My- muscle (prefix).

Necrosis n. the death of some or all of the cells in an organ or tissue, caused by disease, physical or chemical injury, or interference with the blood supply.

Neoplasm n. a new and abnormal growth: any benign or malignant tumour.

Nodule n. a small swelling or aggregation of cells.

Nullipara n. a woman who has never given birth to an infant capable of survival.

Oedema n. excessive accumulation of fluid in the body tissues: popularly known as dropsy.

Papilla n. any small nipple-shaped protuberance.

Papilloma n. a benign growth on the surface of skin or mucuous membrane.

Parenchyma n. the functional part of an organ, as opposed to the supporting tissue (stroma).

Parity n. the condition of a woman with regard to the number of pregnandes she has had that have each resulted in the birth of an infant capable of survival.

Pathology n. the study of disease processes with the aim of understanding their nature and causes.

Plasmacytoma n. a malignant tumour of plasma cells.

Pleomorphism n. the condition in which an individual assumes a number of different forms during its life cycle.

Plexus n. a network of nerves or blood vessels.

Proliferate vb. to grow rapidly by cell division : applied particularly to malignant tumours.

Prosthesis n. any artificial device that is attached to the body as a substitute for a missing or non-functional part.

Protoplasm n. the material of which living cells are made.

Protuberance n. a rounded projecting part.

Puerperal adj. relating to childbirth or the period that immediately follows it.

Purulent adj. forming, consisting of, or containing pus.

Sarcoma n. any cancer of connective tissue.
Scirrhous adj. describing carcinomas that are stony hard to the touch.
Sclero- prefix denoting 1. hardening or thickening, 2. the sclera (eye), 3. sclerosis.
Sclerosis n. hardening of tissue, usually due to scarring (fibrosis) after inflammation.
Stellate adj. star-shaped.
Sternum n. the breastbone: a flat bone extending from the base of the neck to just below the diaphragm and forming the front part of the skeleton of the thorax. The sternum articulates with the collar bones and the costal cartilages of the first seven pairs of ribs.
Supernumerary a. in excess of normal number; extra.
Syncytium n. a mass of protoplasm containing several nuclei.

Thorax n. the chest.
Trabecula n. any of the bands of tissue that pass from the outer part of an organ to its interior, dividing it into separate chambers.
Tumour n. any abnormal swelling in or on a part of body. The term is usually applied to an abnormal growth of tissue, which may be benign or malignant.

B

Attenuation of X-ray Photons

The photons of a beam of radiation are removed (attenuated) from the beam either by absorption or scattering. At the energies at which mammography is performed (10 - 28keV) there are two main attenuation processes: the photoelectric effect (absorption) and the Compton effect (scattering). In the photoelectric effect a photon is completely absorbed by the tissue, part of its energy being used to free an electron from an atom or molecule, the rest being given to the freed electron in the form of kinetic energy. The Compton effect results when a photon is scattered by an effectively free electron, continuing with less energy, the difference being given to the electron in the form of energy of recoil. The photoelectric effect is greatest for low-energy photons, whilst the Compton effect starts to dominate at much higher energies. The actual processes involved are highly complicated and are explained fully in [5] and [96].

Those x-ray photons which are not attenuated are said to form the primary beam. Beer's law for pencil beams relates the number of incident x-ray photons (N_0^{real}), number of primary beam photons (N_p^{real}), thickness of a material (h) and linear attenuation coefficient of the material (μ) at any one photon energy (E):

$$N_p^{real}(E) = N_0^{real}(E)\, e^{-h\mu(E)} \tag{B.1}$$

The linear attenuation coefficient is related to the density of the material, the atomic number of the material, and the photon energy E. It refers to the proportion of the photons at the specified energy which are removed per centimetre and it has units cm^{-1}. The coefficient μ is made up of terms for attenuation by both scattering (Compton effect)

and absorption (photoelectric):

$$\mu(E) = \mu_s(E) + \mu_a(E) \tag{B.2}$$

Application of Beer's law to a non-diverging monoenergetic beam of finite dimension (area A) with known incident and exiting intensities provides an average attenuation value:

$$\begin{aligned} \overline{h\mu} &= \log_e \left(\frac{\int_A \int N_0^{real}(x,y)dxdy}{\int_A \int N_p^{real}(x,y)dxdy} \right) \\ &= \log_e \left(\overline{\frac{N_0^{real}}{N_p^{real}}} \right) \end{aligned}$$

Note that this is not the average $h\mu$ over the area, and consequently will be an over- or under-estimate depending upon the distribution of $h\mu$ over the area. If the distribution is uniform then the equation gives the true average attenuation.

There is usually more than one material in the path of an x-ray and so equation (B.1) is often written as:

$$N_p^{real}(E) = N_0^{real}(E)e^{-(h_1\mu_1(E)+\cdots+h_i\mu_i(E)+\cdots+h_n\mu_n(E))},$$

where h_i is the total thickness of material i, and $\mu_i(E)$ is its linear attenuation coefficient at photon energy E. For polyenergetic x-ray beams it becomes necessary to integrate over all the photon energies.

C

Diagnosing Breast Cancer

C.1 Introduction to mammography

Mammography is the process by which a breast is exposed to an x-ray source to create a projective image showing differences in x-ray attenuation. Parts of the breast which consist of dense tissue rather than fatty tissue, attenuate a greater number of x-ray photons. The darkness of the film is related to the number of number of photons which pass through the breast. Thus, fatty tissue within the breast is represented by dark areas whereas denser structures are represented as light areas.

Mammography is the only method presently suitable for mass screening of women for breast cancer. It is both relatively cheap and effective in revealing the subtle and sometimes minute signs of early breast cancer [12], although some 8% of cancers are missed [67] and 70–80% of open surgical biopsies are benign [91].

The difficulty of the radiologist's task in diagnosing breast cancer from mammograms is due to several reasons. The most obvious difficulty is the projective nature of mammography, whereby dense tissues can be projected next to each other to form composites which look suspicious. Composites formed in this way are not unusual because the attenuation properties of different breast tissues, both normal and neoplastic, are similar. The next problem is that some breasts are very dense and their mammograms are very bright (figure C.1); this hides the bright patterns due to cancer. Another problem is that some signs of breast cancer are minute and can be simply missed if the mammogram is not studied sufficiently closely. The last, and perhaps the most

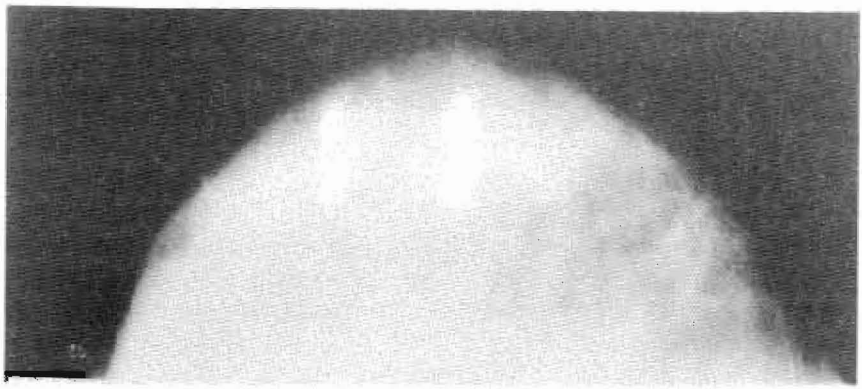

Figure C.1: An example of a mammogram of a dense breast. The radiologists task can be made exceptionally difficult, if not impossible, in breasts which are dense. Mammograms of women taken before menopause often appear like this, and it is the reason that hospitals in the UK generally do not perform mammography before the age of 35.

important problem, is that many mammographic signs only probably indicate breast cancer. These ambiguous signs have to studied with evidence accumulated from other modalities.

Clearly, the radiologist's task is difficult and the purpose of this appendix is to give the reader a sense of what diagnosing from mammograms entails. We firstly explain the screening procedure, and then briefly examine the two stages of the radiologist's task: detection of possible abnormalities and interpretation of abnormalities. The reader is referred to one of several books on the subject for more detailed explanation of how breast cancer is diagnosed [79], [84], [12].

(a) (b) (c)

Figure C.2: Woman positioned for (a) cranio-caudal (b) 45° mediolateral oblique (c) mediolateral mammogram.

C.2 Screening programme

The screening programme involves women between the ages of 50 and 64 years attending for mammography every 2 or 3 years [31]. The screening clinic is often mobile and involves only radiographers. The women who attend have one mammogram performed on each breast. This screening mammogram is performed from the 45° medio-lateral oblique view, figure (C.2). The 45° medio-lateral oblique view is used because it includes the pectoral muscle, which is a potential site of cancer.

The mammograms from the screening unit are taken to a stationary breast care unit where they are examined by a radiologist. If, on the basis of this examination, the radiologist finds any suspicious signs then the woman is recalled to an assessment clinic. Around 10% of women are recalled to the assessment clinic where further mammograms at different views are taken. The two extra views are the cranio-caudal and the medio-lateral (also shown in figure C.2). Often the extra views are enough to convince the radiologist that there is no cancer present. However, if the radiologist is still suspicious the woman might well be referred for ultrasound, palpation or fine needle aspiration biopsy. If the radiologist and breast care team have not been able to resolve their suspicions, the woman is either sent for open surgical biopsy, or asked to return in 6 months.

C.3 Detection of mammographic abnormalities

After checking that the mammogram is of a high enough quality and that it displays all the relevant information, Caseldine et al. [12] recommend a systematic search to detect

mammographic abnormalities:

1) Compare the mammograms of both breasts for "symmetry". Particularly important is asymmetry of the duct shadow, but also note the shape of the glandular tissue and any asymmetry of density. An example of what radiologists term asymmetry is shown in figure (C.4), whilst an example of symmetry is shown in figure (C.3).

2) Carefully inspect the skin and subcutaneous fat around the entire periphery of the breast image, looking for skin thickening, lack of definition of the deep surface of the skin and any excess of linear shadows traversing the fatty space between the breast tissue and the skin. It is important to compare the appearances at a site in one breast with those in the same position on the other side, before an appearance is judged to be abnormal. Figure (C.5) has an example of skin thickening.

3) Compare the nipples and subareolar regions: is the nipple everted or indrawn? Are the subareolar ducts more prominent than usual? Are they the same on both sides?.

4) Inspect every square centimetre of both breasts looking for distortion of the normal parenchymal pattern, including, very importantly, any interruption of a linear shadow which may be present.

5) Reinspect every square millimetre of both breasts using a magnifying lens in a search for calcifications.

6) Look specifically at the axillary region of both sides to detect the presence of glands.

C.4 Interpretation of mammographic abnormalities

C.4.1 Mass lesions

A mass lesion is commonly defined as an area of increased density (i.e. increased brightness). The margin of a lesion is the most reliable indicator of malignancy. Benign lesions (such as cysts or fibroadenomas) usually have a smooth, well-demarcated margin, often surrounded by the halo of fat it has displaced. Figure (C.6) shows a benign lesion in a thick breast.

If part of the margin of a lesion is ill-defined, it is probably malignant. It is often difficult to be certain if a part of the margin is genuinely ill-defined, or if it is obscured

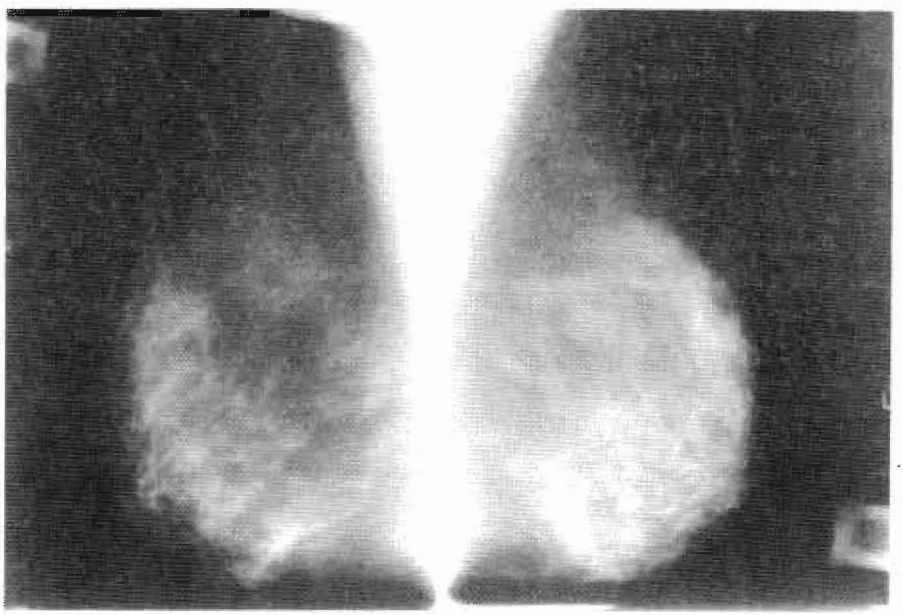

Figure C.3: An example of where a radiologist would use "symmetry" between left and right mammograms. At first glance a non-expert might note as suspicious the bright diffuse line towards the bottom of the each mammogram. However, the presence of the line in both mammograms, and the rarity of bilateral breast cancer, indicate that the line is harmless.

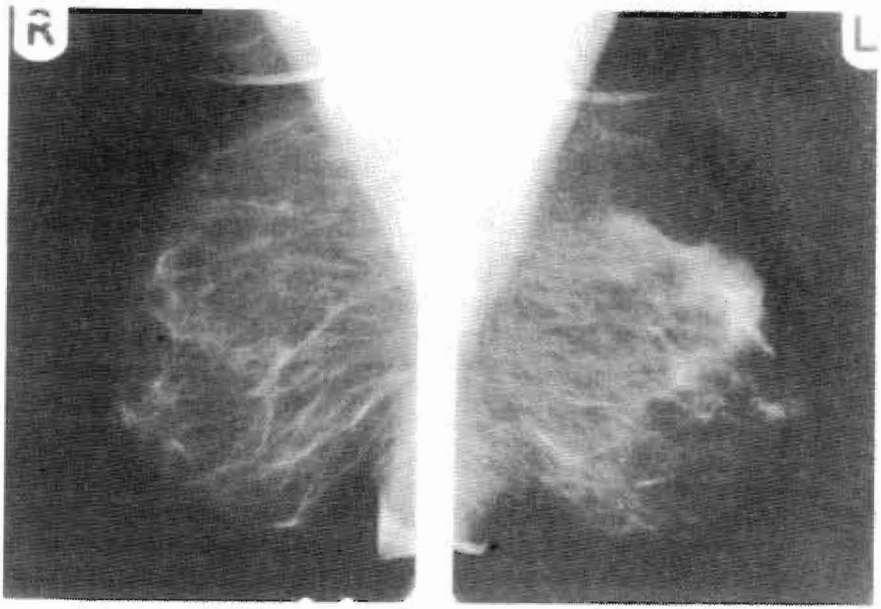

Figure C4: An example of what a radiologist would call "asymmetrical" mammograms. There is a large area of increased density in the left mammogram, and no similar occurrence is found in the right mammogram. In this case, the area of increased density turned out to be of no concern.

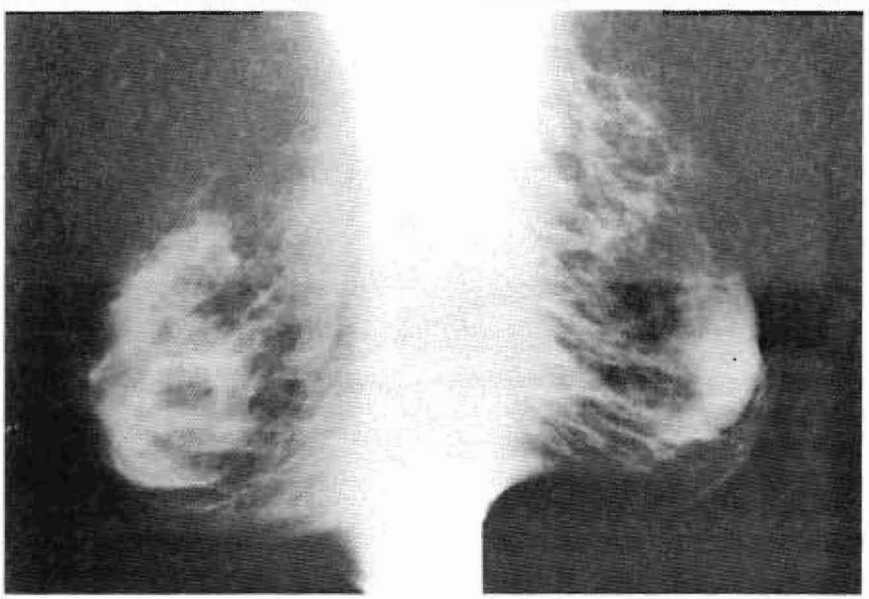

Figure C.5: An example of skin thickening. Normally the breast edge cannot be seen on a mammogram, but sometimes the skin thickens and the edge becomes apparent. Skin thickening can be a secondary sign of cancer, and might sometimes be the most obvious suspicious sign.

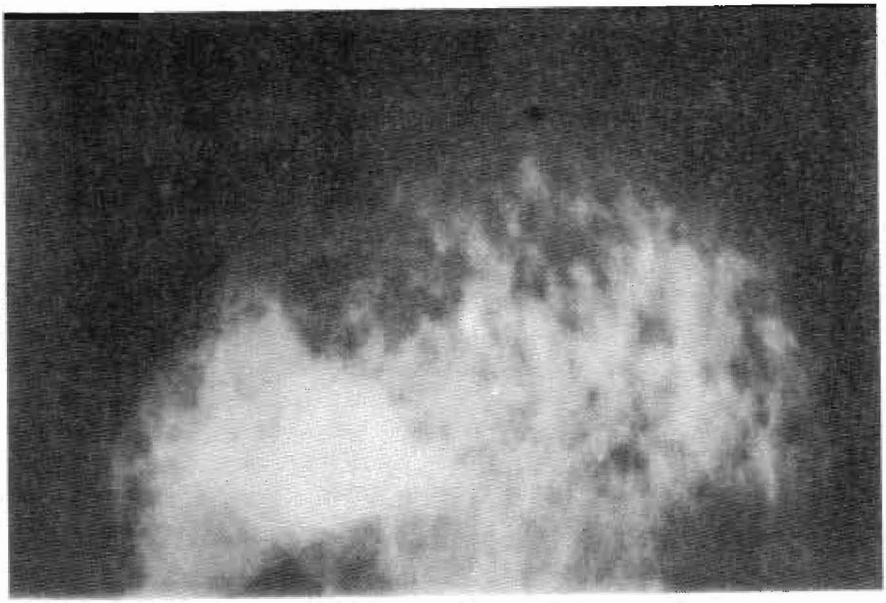

Figure C.6: The round shape in the bottom left of the mammogram is a benign lesion (a cyst). It is not that clear in this mammogram due to the surrounding dense tissue.

by overlying parenchymal shadowing. Figure (C.7) shows a lesion which looks well-defined on most sides but is in fact malignant. An irregular spiculated margin indicates a malignant lesion, particularly if the spicules are relatively short for the size of the lesion. Figure (C.8) shows a spiculated lesion.

The texture of a lesion can also be used for diagnosis. A homogeneous lesion is more likely to be benign than one which is non-homogeneous, whilst a lesion denser than the surrounding breast tissue is more likely to be malignant than one which is less dense.

C.4.2 Calcifications

Calcification can be one of the earliest signs of breast cancer, and is thus considered to be extremely important in screening. Large, coarse, scattered calcifications are invariably benign (figure C.9), as are small, rounded calcifications (figure C.10). However, clusters

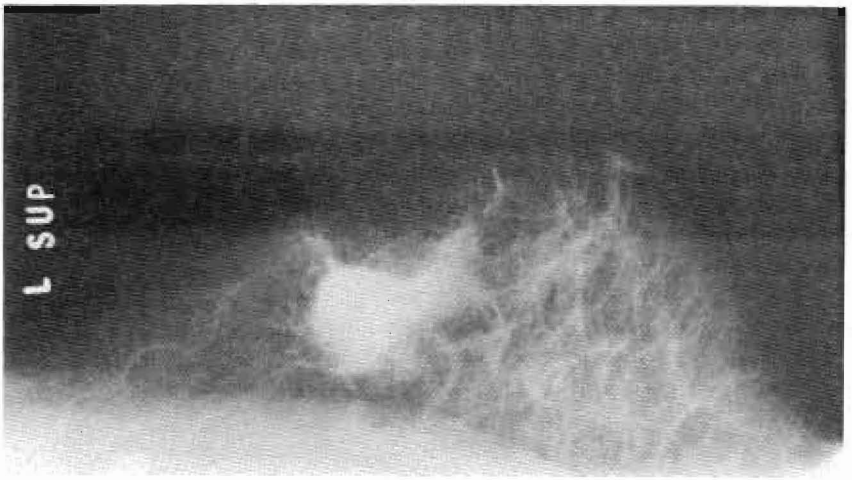

Figure C.7: Despite looking well-defined around most of its border, this lesion is in fact malignant.

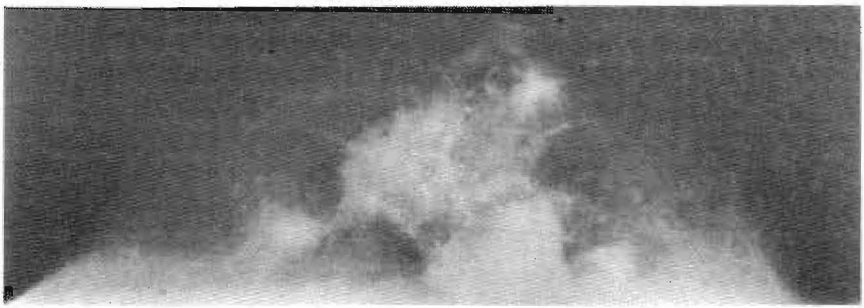

Figure C.8: A spiculated malignant mass: spicularity is a classic sign of malignancy. Sometimes the spicules attach themselves to the chest wall or the skin (in which case clinical signs can appear such as tethering).

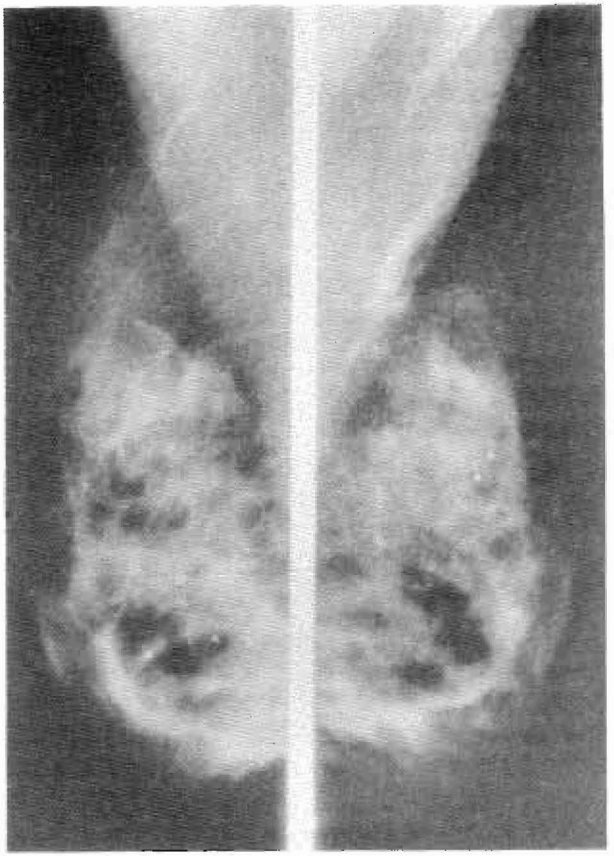

Figure C.9: An example of breasts with coarse calcifications. Coarse calcifications are not indicative of cancer.

of fine calcifications are likely to signify malignancy, especially if the particles are linear or branching (i.e. in the ducts). Groups of calcifications of mixed size with irregular shapes are also likely to signify malignant than benign disease. Figure (C.11) shows an example of a malignant cluster of calcifications.

C.4.3 Parenchymal deformities

Parenchymal deformities can be one of the first signs of breast cancer. The title covers a broad band of abnormalities which are detected from asymmetry or subtle distortion of the normal parenchymal pattern. If the parenchyma appears pushed aside by a lesion,

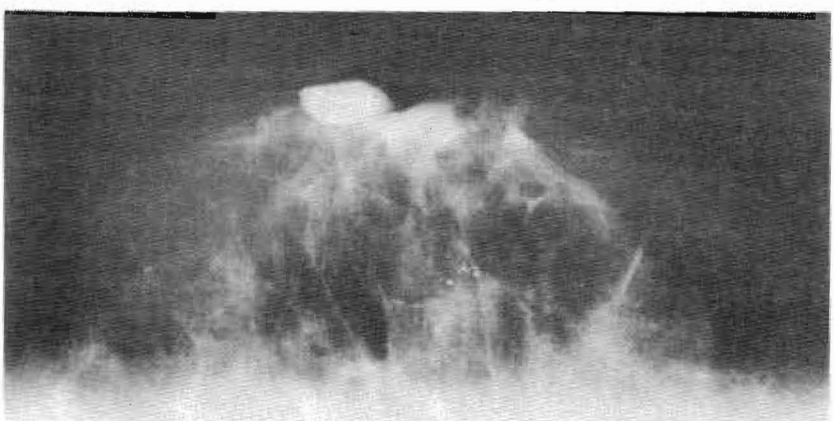

Figure C.10: Small rounded calcifications are usually benign.

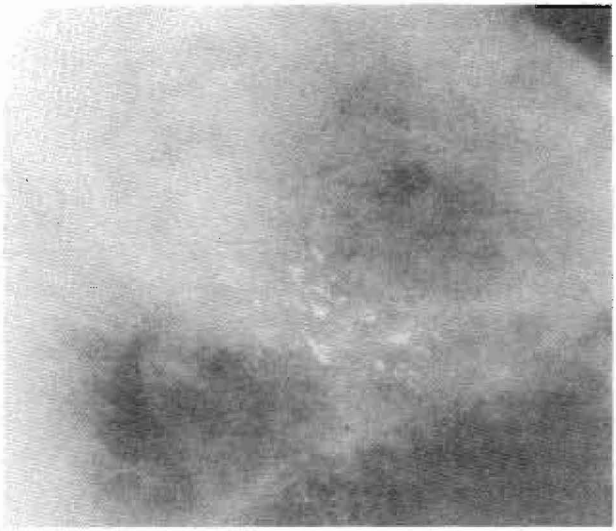

Figure C.11: An enlarged view of a cluster of malignant calcifications. Note the irregular shapes of the particles and the number of particles, both of which are considered to be signs of suspicion.

the lesion is likely to be benign. If the parenchymal strands are pulled in towards a lesion it is more likely to be malignant. If the parenchymal strands are actually interrupted by a lesion, it is highly likely to be malignant.

C.4.4 Reaction of a lesion

Lesions sometimes cause secondary signs to appear in mammograms, and these secondary signs might be the only visible sign of the cancer. Localized skin thickening is one of the more common secondary signs. It is almost always associated with a fairly obvious subcutaneous reaction (linear shadows reaching across subcutaneous fat layer to skin). The deep surface of the skin becomes slightly spiculated in the early stages and finally the thickened segment of the skin is drawn in towards the lesion. This strongly suggests malignancy. Distant skin thickening may be observed secondary to lymphatic obstruction or to oedema produced by a lesion. When detected, it is a highly significant finding.

A number of prominent ducts extending from a lesion towards the nipple strongly suggests malignancy, particularly if as a group they have a biconvex appearance, converging both on the lesion and on the nipple. A fan-shaped group of prominent ducts extending from the nipple is likely to be due to duct ectasia (benign).

D

Digitization Using a CCD Camera

The mammograms used for the work undertaken for this thesis were initially digitized using a CCD camera (Panasonic WV-CD50, Pulnix TM526 CCD+B50CS). These digitized images were abandoned because we could not discover how to remove the camera variables in order to transform pixel values into film densities. Figure (D.1) shows the main problem which we encountered. In this image, the intensity level of a uniform piece of black card is seen to vary considerably depending upon the overall brightness of each *horizontal* line. Figure (D.2) shows the pixel values recorded for an image consisting of a piece of black card with different length horizontal grey strips but without the white saturated, again the suppression effect is observed. The illuminating light in both cases was constant, as seen by taking an image of a uniform blank card.

To explain the suppression effect, the relationship between light transmitted through a film (T_l) and pixel value P was investigated. We did this using a light box and a strip of film which had a series of known film densities on. The relative intensity of the light received by the camera can be estimated from the light transmitted through the film which is found from the film density. The relationship of transmitted light to pixel value on any one *horizontal* line was almost perfectly linear within the bounds of the cameras sensitivity, figure (D.3).

It was our original intention to increase the dynamic range of our mammographic images by taking light and dark pictures of each mammogram and then combining them. We envisaged doing this by placing a calibration strip along the bottom of each film. However, because the camera is only linear along each horizontal line the linear

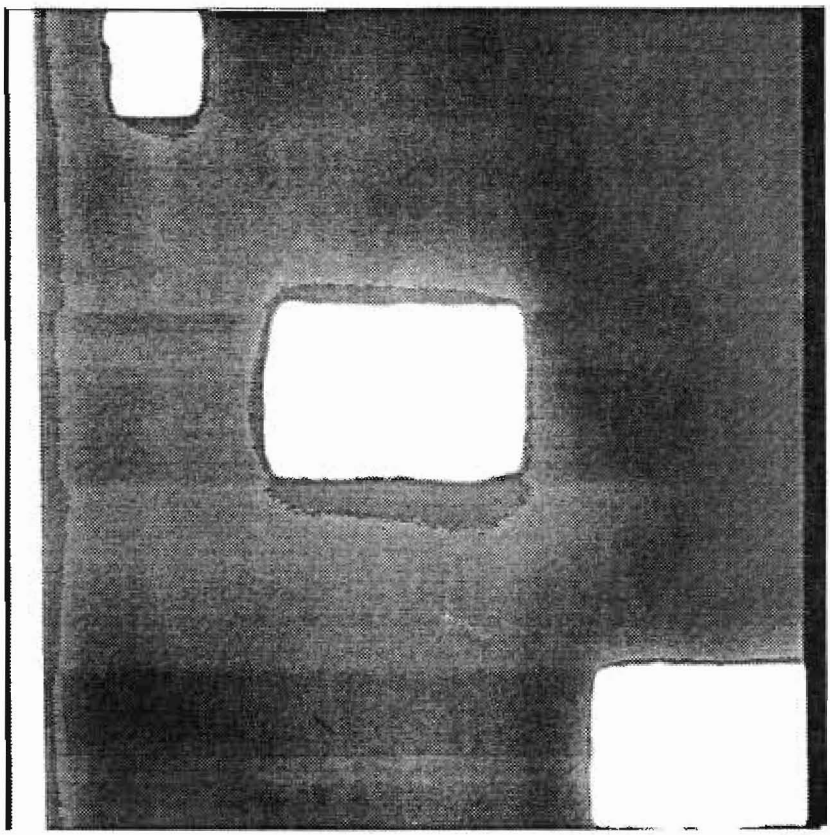

Figure D.1: An image taken with a CCD camera. All the external camera controls are switched off. The image shows that there is still an AGC circuit at work since horizontal lines with high brightness have their pixel values suppressed. This effect cannot be due to "blooming" or "smearing" from the saturated white levels since in these cases the pixel values would rise.

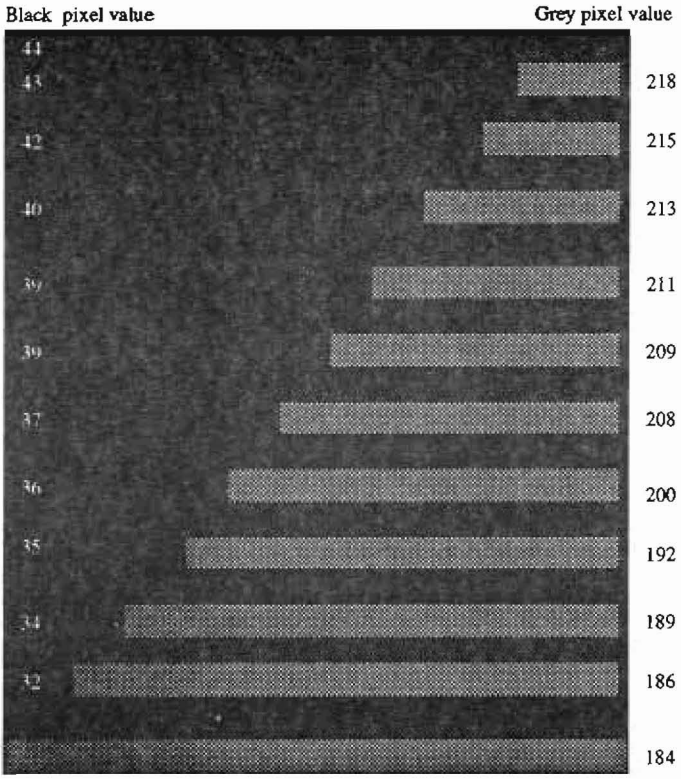

Figure D.2: A copy of an image in which a piece of black card with different length grey strips was imaged. The values down either side show the suppression of the pixel values as the overall brightness of the horizontal line increases.

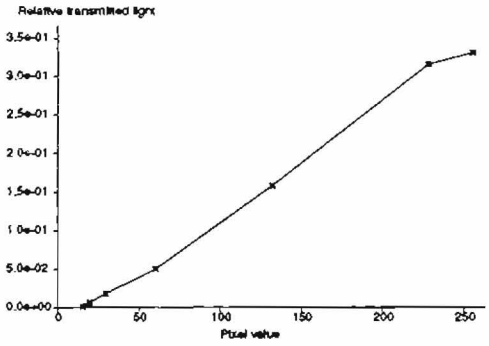

Figure D.3: The relationship between light reaching a CCD camera (i.e. the light transmitted through the film) and pixel value is practically linear for any one horizontal line within the bounds of the cameras sensitivity and when all external camera options are switched off.

variables need to found for each line and this seemed excessive and unreliable. Instead, we tried to predict the cameras output based on a conjectured link between the camera variables and the average input intensity of light:

$$P = \overline{P} + \alpha(T_l - \overline{T_l})$$

The relationship between $\overline{T_l}$, $\overline{P}$ and α is complex and despite some results indicating that there is a relationship we did not take the investigation any further. Our investigations were not helped by the apparent lack of knowledge of their products displayed by the camera manufacturers.

E

Calibration Using a Lucite Step Wedge

The model of the mammographic process described in chapter 3 requires that the relationship between film density (D) and relative energy imparted to the intensifying screen (E) be known. Idealy, the energy imparted to the intensifying screen in an area would be measured and plotted against the film density measured in that area using a densitometer. Unfortunately, it is extremely difficult to measure the energy imparted to the intensifying screen accurately. We approximate the relationship between relative energy imparted to the intensifying screen and film density by using a lucite step wedge as shown in figure (E.1). An exposure of this step wedge was performed before every mammogram used in this thesis and it was assumed that the film processing conditions do not change greatly over the short period of time between developing the step wedge and developing the mammogram.

Lucite was used for the step wedge because of the similarity between the attenuation properties of lucite and that of breast tissue consisting of half fat and half interesting tissue. This can be seen by comparing the linear attenuation coefficient of lucite with those of fat and interesting tissue, figure (E.2).

The mammography machine which was used for this work has only a limited range of manual exposure settings. Consequently, to obtain the complete range of film densities and thereby get the full characteristic curve requires that some object be placed over the automatic exposure control to give a suitable exposure. We calculated that a block of lucite big enough to cover the automatic exposure control and 3.59cm thick was suitable. This thickness gives an exposure in terms of mAs of around 30,

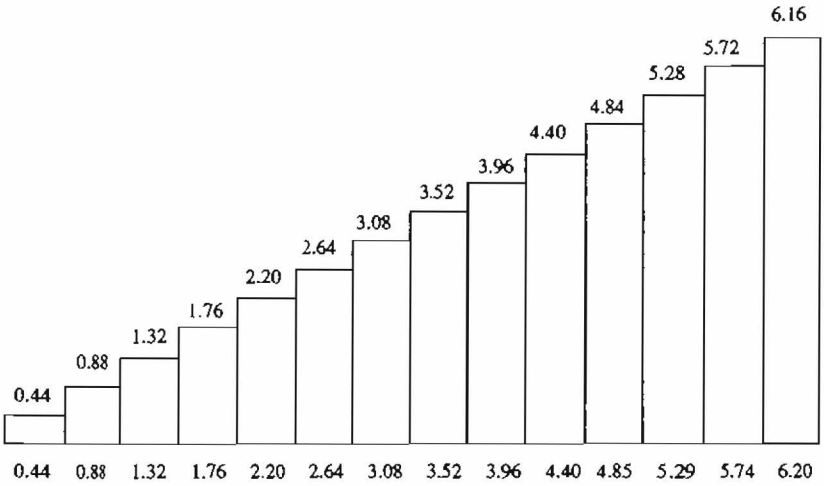

Figure E.1: The lucite step wedge which we use to find the relationship between relative energy imparted to the intensifying screen and film density. The height of each step of lucite is given above it, and beneath the wedge is given the thickness of lucite through which the photons actually have to pass to reach the screen, given the geometry of the system: the wedge is always placed with the focal spot directly above the middle of the wedge.

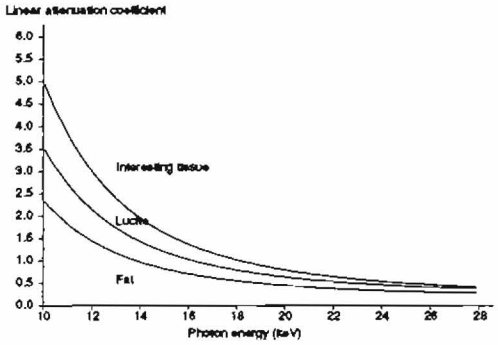

Figure E.2: Values of the linear attenuation coefficients for lucite, calculated from the mass attenuation coefficients as reported by by Hubbell [50] using a lucite density of 1.180 g $cm^{-}3$. Also shown are the linear attenuation coefficients for fat and interesting tissue.

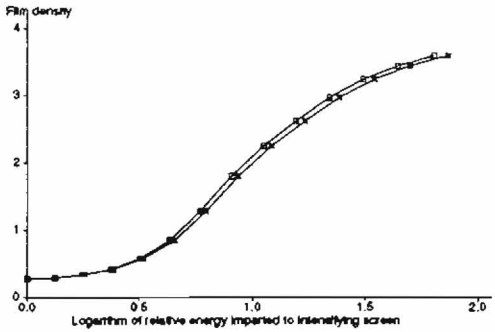

Figure E.3: Characteristic curve calculated using a lucite step wedge. Two curves are shown, one with a scatter estimate (squares) and the one using just the simulated primary (crosses) energy imparted.

and this is enough to produce a range of film densities from 0.2 to 3.7 (the full range available on the film).

With the lucite block over the automatic exposure control the step wedge was placed along the back of the film, where the chest wall is usually. Positioning is important because it is known that the incident radiation intensity varies greatly from the usual position of the chest wall out towards the nipple, but not much laterally. With the lucite step wedge always in this position it is simple to use the system geometry to calculate the actual thickness of lucite through which the photons must pass to reach the film. Using these thicknesses the relative energy imparted to the screen can be simulated using the model and incident energy spectrum presented in chapter 3. A scatter contribution is calculated on the basis of the ratios calculated by Barnes and Brezovich [4] corrected for use of anti-scatter grid. The height of lucite used for the scatter contribution is the height of the particular step, this seems reasonable because the steps are large and the scatter locations are quite local when a grid used (as shown in chapter 5).

Table (E.1) gives the relative energy imparted for each step from this simulation, also given, for interest, is the effective attenuation coefficient of the lucite; this shows the beam hardening effect. Figure (E.3) shows the characteristic curve given by using the scatter estimate and by ignoring scatter.

H	μ	R_p	R	L
6.16	0.764	1.000	1.000	0.0
5.72	0.772	1.337	1.323	0.122
5.28	0.780	1.797	1.761	0.246
4.84	0.789	2.430	2.358	0.373
4.40	0.798	3.307	3.177	0.502
3.96	0.807	4.528	4.304	0.634
3.52	0.817	6.238	5.869	0.769
3.08	0.827	8.651	8.054	0.906
2.64	0.839	12.083	11.130	1.046
2.20	0.851	17.001	15.492	1.190
1.76	0.865	24.120	21.742	1.337
1.32	0.881	34.550	30.802	1.489
0.88	0.900	50.065	44.141	1.644
0.44	0.924	73.637	64.197	1.808

Table E.1: The relative energies imparted to the intensifying screen by photons passing through a lucite step wedge as calculated in a simulation: H is the height of the step (the actual height seen from the focal spot is given in figure E.1; μ is the effective attenuation coefficient of the lucite; R_p is the relative energy imparted due to the primary beam; R is the relative energy imparted due to primary and scatter; L is the logarithm of the relative imparted energies of R.

Bibliography

[1] L. V. Ackerman and E. E. Gose. Breast lesion classification by computer and xeroradiograph. *Cancer*, 30:1025 – 1035, 1972.

[2] B. A. Arnold, H. Eisenberg, and B. E. Bjarngard. Measurement of reciprocity law failure in green-sensitive x-ray films. *Radiology*, 126:493 – 498, 1978.

[3] G. T. Barnes. Radiographic mottle : A comprehensive theory. *Medical Physics*, 9(5):656 – 667, 1986.

[4] G. T. Barnes and I. Brezovich. The intensity of scattered radiation in mammography. *Radiology*, 126:243 –247, 1978.

[5] H. Barrett and W. Swindell. *Radiological Imaging*. Academic Press, 1981.

[6] S. I. Barry and G. K. Aldis. Comparison of models for flow induced deformation of soft biological tissue. *Journal of Biomechanics*, 23:647 – 654, 1990.

[7] B. Burkhardt, P. Schnur, J. Tufield, and P. Dempsey. Objective clinical assessment of fibrous capsular contrature. *Plastic and Reconstructive Surgery*, 69:794, 1982.

[8] C. B. Caldwell, S. J. Stapleton, D. W. Holdsworth, R. A. Jong, W. J. Weiser, G. Cooke, and M. J. Yaffe. Characterization of mammographic parenchymal pattern by fractal dimension. *Physics in Medicine and Biology*, 35(2):235 – 247, 1990.

[9] C. B. Caldwell, S. J. Stapleton, D. W. Holdsworth, R. A. Jong, W. J. Weiser, G. Cooke, and M. J. Yaffe. Characterization of mammographic parenchymal pattern by fractal dimension. *SPIE Medical Imaging III: Image Processing*, 1092:10 – 16, 1989.

[10] C. B. Caldwell and M. J. Yaffe. Development of an anthropomorphic breast phantom. *Medical Physics*, 17(2):273 – 280, 1990.

[11] G. A. Carlsson, D. R. Dance, and J. Persliden. Grids in mammography: Optimization of the information content relative to radiation risk. Technical Report ULi-RAD-R-059, Linkoping University, Department of Radiation Physics, 1989.

[12] J. Caseldine, R. Blamey, E. J. Roebuck, and C. Elston. *Breast Disease for Radiographers*. Wright, 1988.

[13] N. J. Cerneaz. Automated analysis of mammograms. First year report, Engineering Science, Oxford University, 1992.

[14] H-P. Chan, K. Doi, S. Galhotra, C. J. Vyborny, H. MacMahon, and P. M. Jokich. Image feature analysis and computer-aided diagnosis in digital radiography.1. automated detection of microcalcifications in mammography. *Medical Physics*, 14:538 – 548, 1987.

[15] H-P. Chan, K. Doi, K-L. Lam, C. J. Vyborny, R. A. Schmidt, and C. E. Metz. Digital characterization of clinical mammographic microcalcifications:applications in computer-aided detection. *SPIE : Medical Imaging II*, 914:591 – 593, 1988.

[16] H-P. Chan, K. Doi, C. Vyborny, C. Metz, H. MacMahon, P. Jokich, and S. Galhotra. Digital mammography:development of a computer-aided system for detection of microcalcifications. *SPIE : Medical Imaging*, 767:367 – 370, 1987.

[17] H-P. Chan, K. N. Doi, K. L. Lam, C. J. Vyborny, and R. A. Schmidt. Computer-aided detection of microcalcifications in mammograms : Methodology and preliminary clinical study. *Investigative Radiology*, 23:664 – 671, 1988.

[18] D. J. Clark, I. R. Chambers, K. Faulkner, J. Rayson, P. M. Hacking, and J. Milton. Pressure measurements during automatic breast compression in mammography. *J. Biomedical Engineering*, 12:444 – 446, 1990.

[19] D. R. Dance. The monte carlo calculation of integral radiation dose in xeromammography. *Physics in Medicine and Biology*, 25:25 – 37, 1980.

[20] D. R. Dance and G. J. Day. Computation of scatter in mammography by monte carlo methods. *Physics in Medicine and Biology*, 29:237 – 247, 1984.

[21] D. R. Dance, J. Persliden, and G. A. Carlsson. Calculation of dose and contrast for two mammographic grids. *Physics in Medicine and Biology*, 37:235 – 248, 1992.

[22] D. H. Davies and D. R. Dance. Automatic computer detection of clustered calcifications in digital mammograms. *Physics in Medicine and Biology*, 35:1111 – 1118, 1990.

[23] D. H. Davies, D. R. Dance, and C. H. Jones. Automatic detection of microcalcifications in digital mammograms using local area thresholding techniques. *SPIE Medical Imaging III: Image Processing*, 1092:153 – 161, 1989.

[24] A. P. Dhawan, G. Buelloni, and R. Gordon. Enhancement of mammographic features by optimal adaptive neighbourhood image processing. *IEEE Medical Imaging*, 5:8 – 15, 1986.

[25] A. P. Dhawan and E. Le Royer. Mammographic feature enhancement by computerized image processing. *Computer Methods and Programs in Biomedicine*, 27:23 – 35, 1988.

[26] J. E. Egan. A constitutive model for the mechanical behaviour of soft connective tissues. *Journal of Biomechanics*, 20:681 – 692, 1987.

[27] G. W. Eklund. Mammographic compression: Science or art? *Radiology*, 181:339 – 341, 1991.

[28] B. W. Fam, S. L. Olson, P. F. Winter, and F. J. Scholz. The detection of calcification clusters in film-screen mammograms; a detailed algorithmic approach. *SPIE Medical Imaging II*, 914:620 – 634, 1988.

[29] B. W. Fam, P. F. Winter, F. J. Scholz, and S. L. Olson. Algorithm for the detection of fine clustered calcifications on film mammograms. *Radiology*, 169:333 – 337, 1988.

[30] I. Fife. The physical dimensions of compressed breasts. *British Journal of Radiology*, 64:73 – 74, 1991.

[31] P. Forrest. *Breast Cancer Screening. Report to the Health Ministers of England, Wales, Scotland and Northern Ireland*. HMSO, 1986.

[32] S. H. Fox, U. M. Pujare, W. G. Wee, M. Moskowitz, and R. V. Hutter. A computer analysis of mammographic microcalcifications : Global approach. In *Proceedings of the 5th IEEE Conference on Pattern Recognition*, pages 624 – 631, 1980.

[33] E. E. Frederick, M. R. Squillante, L. J. Cirignano, R. W. Hahn, and G. Entine. Accurate automatic exposure controller for mammography: Design and performance. *Radiology*, 178:393 – 396, 1991.

[34] K. E. Fredfeldt, E. Christensen, K. Conradsen, B. Ersboll, and S. Stedstrup. Automatic screening of plain film mammography. *Seminars in Ultrasound, CT, and MRI*, 13(2):135 – 139, 1992.

[35] I. M. Freundlich, T. B. Hunter, G. W. Seeley, C. J. D'Orsi, and N. L. Sadowsky. Computer-assisted analysis of mammographic clustered calcifications. *Clinical Radiology*, 40:296 – 298, 1989.

[36] A. G. Gale, E. J. Roebuck, P. Riley, and B. S. Worthington. Computer aids to mammographic diagnosis. *British Journal of Radiology*, 60:887 – 891, 1987.

[37] M. L. Giger, F-F. Yin, K. Doi, C. E. Metz, R. A. Schmidt, and C. J. Vyborny. Investigation of methods for the computerized detection and analysis of mammographic masses. *SPIE Medical Imaging IV : Image Processing*, 1223:183 – 184, 1990.

[38] R. Gordon and R. M. Rangayyan. Correction to feature enhancement of film mammograms using fixed and adaptive neighbourhoods. *Applied Optics*, 23:2055 – 2055, 1984.

[39] R. Gordon and R. M. Rangayyan. Feature enhancement of film mammograms using fixed and adaptive neighbourhoods. *Applied Optics*, 23:560 – 564, 1984.

[40] L. Gylbert. Applanation tonometry for the evaluation of breast compressibility. *Scandinavian Journal of Plastic and Reconstructive Surgery*, 23:223, 1989.

[41] L. Gylbert and A. Berggren. Constant compression caliper for objective measurement of breast capsullar contracture. *Scandinavian Journal of Plastic and Reconstructive Surgery*, 23:137 – 142, 1989.

[42] G. R. Hammerstein, D. W. Miller, D. R. White, M. E. Masterson, H. Q. Woodard, and J. S. Laughlin. Absorbed radiation dose in mammography. *Radiology*, 130:485 – 491, 1979.

[43] W. Hand, J. L. Semmlow, L. V. Ackerman, and F. S. Alcorn. Computer screening of xeromammograms : A technique for defining suspicious areas of the breast. *Computers and Biomedical Research*, 12:445 –460, 1979.

[44] R. P. Highnam, J. M. Brady, and B. J. Shepstone. Computing the scatter component of mammographic images (submitted). *IEEE Medical Imaging*, 1992.

[45] R. P. Highnam, J. M. Brady, and B. J. Shepstone. Model-based enhancement of mammographic images (submitted). *IEEE Medical Imaging*, 1992.

[46] R. P. Highnam, J. M. Brady, and B. J. Shepstone. Model-based enhancement of mammographic images. In *International Conference on Image Processing*, 1992.

[47] R. P. Highnam, B. J. Shepstone, and J. M. Brady. Mammograms at different compression plate widths for the detection of breast cancer. In *Radiology and Oncology 91, Work in Progress (abstracts)*, page 3. British Institute of Radiology, 1991.

[48] R. P. Highnam, B. J. Shepstone, and J. M. Brady. Differential compression mammography. *Investigative Radiology*, 1992.

[49] R. P. Highnam, B. J. Shepstone, and J. M. Brady. Mammograms at different compressions for the detection of breast cancer. In *Symposium Mammographicum (poster abstracts)*. Symposium Mammographicum, 1992.

[50] J. H. Hubbell. *Photon Cross Sections, Attenuation Coefficients, and Energy Absorption Coefficients from 10keV to 100Gev.* NSRDS-NBS 29 (U.S. GPO, Washington, DC), 1969.

[51] M. Ishida, H. Kato, K. Doi, and P. Frank. Development of a new digital radiographic image processing system. *SPIE*, 347:42 – 48, 1982.

[52] V. P. Jackson, A. M. Lex, and D. J. Smith. Patient discomfort during screen-film mammography. *Radiology*, 168:421 – 423, 1988.

[53] C. E. Jamison, R. D. Marangoni, and A. A. Glaser. Viscoelastic properties of soft tissue by discrete model characterization. *Journal of Biomechanics*, 1:33 – 46, 1968.

[54] R. Jennings, R. Eastgate, M. Siedband, and D. Ergan. Optimal x-ray spectra for screen-film mammography. *Medical Physics*, 8:629 – 639, 1981.

[55] P. C. Johns and M. J. Yaffe. Coherent scatter in diagnostic radiation. *Medical Physics*, 10:40 – 50, 1983.

[56] P. C. Johns and M. J. Yaffe. X-ray characterisation of normal and neoplastic breast tissue. *Physics in Medicine and Biology*, 32:675 – 695, 1987.

[57] N. Karssemeijer. A stochastic method for automated detection of microcalcifications in digital mammograms. In *XIIth Conference on Information Processing in Medical Imaging*, 1991.

[58] N. Karssemeijer and L. van Erning. Iso-precision scaling of digitized mammograms to facilitate image analysis. In *SPIE Medical Imaging V : Image Processing*, 1991.

[59] C. Kimme, B. O'Loughlin, and J. Sklansky. Automatic detection of suspicious abnormalities in breast radiographs. In T. L. Kunii A. Klinger, K. S. Fu, editor, *Data Structures,Computer Graphics and Pattern Recognition*, pages 427 – 447. Academic Press, New York, 1977.

[60] C. Kimme-Smith, L. W. Bassett, R. H. Gold, and S. Chow. Increased radiation dose in mammography due to prolonged exposure, delayed processing, and increased film darkening. *Radiology*, 178:387 – 391, 1991.

[61] D. J. Klein, H-P. Chan, E. P. Muntz, K. Doi, K. Lee, P. Chopelas, H. Bernstein, and J. Lee. Experimental and theoretical energy and angular dependencies of scattered radiation in the mammography energy range. *Medical Physics*, 10:664 – 668, 1983.

[62] S-M. Lai, X. Li, and W. F. Bischof. On techniques for detecting circumscribed masses in mammograms. *IEEE Medical Imaging*, 8:377 – 386, 1989.

[63] K. Lam and H-P. Chan. Effects of beam equalization on mammographic imaging. *Medical Physics*, 17:242 – 249, 1990.

[64] J-L. Lamarque. An atlas of the breast, 1988.

[65] T. Lau and W. F. Bischof. Automated detection of breast tumors using the asymmetry approach. *Computers and Biomedical Research*, 24:273 – 295, 1991.

[66] I. E. Magnin, F. Cluzeau, and C. L. Odet. Mammographic texture analysis: an evaluation of risk for developing breast cancer. *Optical Engineering*, 25:780 – 784, 1986.

[67] J. E. Martin, M. Moskowitz, and J. R. Milbrath. Breast cancer missed by mammography. *American Journal of Roentgenology*, 132:737 – 739, 1979.

[68] P. Miller. Classification of breast tissue by texture analysis. *First Year Report, Dept Medical Biophysics, U Manchester*, pages 29 – 33, 1991.

[69] J. R. Moore. Applanation tonometry of breasts. *Plastic and Reconstructive Surgery*, 63:9, 1979.

[70] E. P. Muntz, T. Fewell, R. Jennings, and H. Bernstein. On the significance of very small angle scattered radiation to radiographic imaging at low energies. *Medical Physics*, 10:819 – 823, 1983.

[71] S. Naimuddin, B. Hasegawa, and C. Mistretta. Scatter-glare correction using a convolution algorithm with variable weighting. *Medical Physics*, 14:330 – 334, 1987.

[72] R. Nishikawa and M. J. Yaffe. Signal-to-noise properties of mammographic film-screen systems. *Medical Physics*, 12:32, 1985.

[73] S. L. Olson, F. J. Scholz, P. F. Winter, B. W. Fam, S. E. Gordon, and A. K. Lee. Breast calcifications : Analysis of imaging properties. *Radiology*, 169:329 – 332, 1988.

[74] C. W. Oomens, D. H. van Campen, and H. J. Grootenboer. A mixture approach to the mechanics of skin. *Journal of Biomechanics*, 20:877 – 885, 1987.

[75] M. M. Osman and E. M. Afify. Thermal modeling of the normal woman's breast. *Journal of Biomechanical Engineering*, pages 123 – 130, 1984.

[76] M. M. Osman and E. M. Afify. Thermal modeling of the malignant woman's breast. *Journal of Biomechanical Engineering*, pages 269 – 276, 1988.

[77] G. J. Parkin. Direct digital mammography. In *Symposium Mammographicum (poster abstracts)*. Symposium Mammographicum, 1992.

[78] E. A. Patrick, M. Moskowitz, V. T. Mansukhani, and E. I. Gruenstein. Expert learning system network for diagnosis of breast calcifications. *Investigative Radiology*, 26(6):534 – 539, 1991.

[79] M. E. Peters, D. R. Voegeli, and K. A. Scanlan. *Breast Imaging*. Churchill Livingstone (London, New York, Melbourne), 1989.

[80] P.Wells, editor. *Scientific Basis of Medical Imaging*. Churchill Livingstone, 1982.

[81] J. H. Richter and E. Claridge. Extraction and measurement of lesion edge blur in mammograms by computer image analysis. In H.U.Lemke, M.L.Rhodes, C.C.Jaffe, and R.Felix, editors, *Computer Assisted Radiology*. Springer-Verlag, 1991.

[82] J. H. Richter and E. Claridge. Extraction of quantitative blur measures for circumscribed lesions in mammograms. *Medical Informatics*, 16:229 – 240, 1991.

[83] D. Roberts and N. Smith. *Radiographic Imaging*. Churchill Livingstone, 1988.

[84] E. J. Roebuck. *Clinical Radiology of the Breast*. Heinemann Medical Books (Oxford), 1990.

[85] T. J. Ryan and S. P. Curri. Cutaneous adipose tissue. *Clinics in Dermatology*, 7, 1989.

[86] J. Seibert and J. Boone. X-ray scatter removal by deconvolution. *Medical Physics*, 15:567 – 575, 1988.

[87] J. L. Semmlow, A. Shadagopan, L. V. Ackerman, W. Hand, and F. S. Alcorn. A fully automated system for screening xeromammograms. *Computers and Biomedical Research*, 13:350 – 362, 1980.

[88] Manchester Breast Screening Service. Manchester breast screening manual, 1990.

[89] A. Shadagopan, F. S. Alcorn, J. L. Semmlow, and L. V. Ackerman. Computerized quantification of breast duct patterns. *Radiology*, 143:675 – 678, 1982.

[90] P. Shrivastava. Model to analyse radiographic factors in mammography. *Medical Physics*, 7:222, 1980.

[91] J. H. Shroff, L. R. Lloyd, and D. M. Schroder. Open breast biopsy: A critical analysis. *The American Surgeon*, 57(8):481 – 485, 1991.

[92] E. A. Sickles. Breast calcifications: mammographic evaluation. *Radiology*, 160:289 – 293, 1986.

[93] E. A. Sickles. Mammographic features of 300 consecutive nonpalpable breast cancers. *AJR*, 146:661 – 663, 1986.

[94] K. T. Smith, S. L. Wagner, R. B. Guenther, and D. C. Solmon. The diagnosis of breast cancer in mammograms by the evaluation of density patterns. *Radiology*, 125:383 – 386, 1977.

[95] T. T. Soong and W. N. Haung. A stochastic model for biological tissue elasticity in simple elongation. *Journal of Biomechanics*, 6:451 – 458, 1973.

[96] R. D. Speller and J. A. Horrocks. Photon-scattering - a new source of information. *Physics in Medicine and Biology*, 36:1 – 6, 1991.

[97] W. Spiesberger. Mammogram inspection by computer. *IEEE Biomedical Engineering*, 26:213 – 219, 1979.

[98] L. Stanton, J. Day, T. Villafana, C. Miller, and D. Lightfoot. Screen-film mammographic technique for breast cancer screening. *Radiology*, 163:471 – 479, 1987.

[99] S. Steenstrup. Comments on enhancement of mammographic features by optimal adaptive neighbourhood image processing. *IEEE Medical Imaging*, 6(1):82 – 83, 1987.

[100] D. C. Sullivan, C. A. Beam, S. M. Goodman, and D. L. Watt. Measurement of force applied during mammography. *Radiology*, 181:355 – 357, 1991.

[101] L. Tabar and P. B. Dean. Basic principles of mammographic diagnosis. *Diagnostic Imaging In Clinical Medicine*, 54:146 – 157, 1985.

[102] P. G. Tahoces, J. Correa, M. Souto, C. Gonzalez, L. Gomez, and J. J. Vidal. Enhancement of chest and breast radiographs by automatic spatial filtering. *IEEE Medical Imaging*, 10:330 – 335, 1991.

[103] P. Wainwright. *Pocket Dictionary for Nurses*. Oxford University Press, 1984.

[104] D. J. Watmough and K. M. Quan. Breast compression to increase the sensitivity of light-scanning for the detection of carcinoma; potential hazard? *Journal of Biomedical Engineering*, pages 173 – 174, 1992.

[105] D. J. Watmough and K. M. Quan. X-ray mammography and breast compression. *Lancet*, 340:122, 1992.

[106] W. G. Wee, M. Moskowitz, N-C. Chang, Y-C. Ting, and S. Pemmeraju. Evaluation of mammographic calcifications using a computer program. *Radiology*, 116:717 – 720, 1975.

[107] F. Winsberg, M. Elkin, J. Macy, V. Bordaz, and W. Weymouth. Detection of radiographic abnormalities in mammograms by means of optical scanning and computer analysis. *Radiology*, 89:211 – 215, 1967.

[108] J. N. Wolfe. Breast patterns as an index of risk for developing breast cancer. *AJR*, 126:1130 – 1039, 1976.

[109] X. Wu, G. T. Barnes, and D. M. Tucker. Spectral dependence of glandular tissue dose in screen-film mammography. *Radiology*, 179:143 – 148, 1991.

[110] J. M. Yancey, G. F. McNeely, and R. E. Kinard. Breast traction mammography. *American Journal of Roentgenology*, 156:1321, 1991.

[111] X. Zhou and R. Gordon. Geometric unwarping for digital subtraction mammography. In *Proceedings of Vision Interface '88*, pages 25 – 30. Canadian Image Processing and Pattern Recognition Society, 1988.